

**POLITECNICO DI TORINO**

Master's Degree in Mechanical Engineering



Master's Degree Thesis

**ELECTROMAGNETIC-THERMAL  
FINITE ELEMENT SIMULATIONS OF  
SUPERCONDUCTORS APPLIED IN  
ELECTRICAL MACHINES**

Supervisors

Prof. SILVIO VASCHETTO

Prof. ALBERTO TENCONI

Phd INES PEIXOTO

Candidate

**FABIO PECCHIA**

July 2024



# Summary

The purpose of this thesis is to analyze, simulate, and experimentally verify the behavior of superconductors, materials of significant scientific interest and in ongoing research and development.

Concerning the study of superconductivity, both finite element simulation and analytical analysis requires experimental calibration of the material properties.

This thesis's work is focused in experimentally calibrating and optimizing these characterization methods. For this purpose simulations were conducted to analyze the electromagnetic behavior of two types of conductive tapes: copper and superconducting. These tapes were examined under two distinct thermal conditions—ambient temperature and immersion in liquid nitrogen.

The simulations were carried out under both direct current (DC) and alternating current (AC) regimes.

They were developed and verified, in order to draw important considerations for the work carried out.

For model verification and calibration, experimental tests were carried in superconducting tapes to measure their resistivity characteristic in DC conditions. These experiments were then used to characterize the material properties in the FEM models.

The macroscopic modelling approach is used in order to study and understand deeper the superconductivity, such as the A formulation or the T-A formulation.

The primary objective of this study is to perform a comparative analysis between experimental and numerical results, with an emphasis on achieving optimal model fitting in direct current (DC). This was accomplished using targeted optimization algorithms implemented in Matlab, considering the variable of interest, in particular, the DC parameters of the superconductive tape and the law for the superconducting material considered in this study, a REBCO tape.

The issue related to the losses in terms of electromagnetic heating has been discussed both for DC and AC currents, even compared to the traditional conductors.

Ultimately, this study discusses the potential applications of superconductors in electrical machines, evaluating both the advantages and challenges associated with their use. Additionally, future perspectives in this field are explored.

# Acknowledgements

First and foremost, I would like to express my deepest gratitude to my girlfriend, Francesca. Your unwavering support, love, and patience have been my pillars of strength throughout this journey. Your encouragement in moments of doubt and your belief in my abilities have pushed me to strive for excellence. I cannot thank you enough for being there for me every step of the way.

I owe a great debt of gratitude to my father, Fausto. Your wisdom, guidance, and unwavering faith in me have been a constant source of motivation. You have always been my role model, and your relentless pursuit of knowledge has inspired me to aim high and work hard. Thank you for all the sacrifices you have made to ensure my success.

To my mother, Anna Paola, I am deeply grateful for your endless love and support. Your nurturing spirit and constant encouragement have provided me with the confidence to overcome challenges. Your belief in me has been a driving force, and I am forever thankful for the countless ways you have supported me throughout this journey.

My brother, Andrea, deserves special mention for his steadfast support. Your presence and advice have been invaluable, and your ability to make me smile even in tough times has been a blessing. Thank you for always being there for me and for understanding the importance of my goals.

Lastly, I would like to extend my heartfelt thanks to all the people who have been by my side and supported me in various ways. Friends, colleagues, and mentors—each of you has played a crucial role in my journey. Your friendship, advice, and assistance have been instrumental in the completion of this work. I am truly grateful for your support and encouragement.



# Table of Contents

<b>List of Tables</b>	VIII
<b>List of Figures</b>	IX
<b>Acronyms</b>	XIII
<b>1 Introduction</b>	1
1.1 Overview of superconductors . . . . .	1
1.2 Applications . . . . .	6
1.2.1 Prospective Developments in Superconductor Applications .	11
<b>2 Literature review</b>	14
2.1 Fundamental theoretical concepts of superconductors . . . . .	14
2.1.1 Losses in superconductors . . . . .	14
2.2 Mathematical formulations . . . . .	16
2.3 Superconducting electrical machines . . . . .	17
2.3.1 Advantages and Challenges of Superconducting Technologies in Electrical Machines . . . . .	17
2.3.2 Machines with HTS wires/tapes . . . . .	20
2.3.3 Synchronous machines . . . . .	21
2.3.4 Induction machines . . . . .	22
2.3.5 Magnetic gears . . . . .	23
2.3.6 Machines with HTS bulks/stacked tapes . . . . .	24
<b>3 Theoretical foundations</b>	28
3.1 Electromagnetic theory in electrical machines . . . . .	28
3.1.1 Magnetic Circuits . . . . .	28
3.1.2 More details about Torque,Force,Power and dynamic behavior	30
3.1.3 Maxwell's Equations in Machine Geometry . . . . .	33
3.1.4 How the material influence the losses . . . . .	35
3.1.5 Dynamics in electrical machines . . . . .	36

<b>4</b>	<b>Electromagnetic simulations and experimental results</b>	<b>40</b>
4.1	Models and equations used . . . . .	40
4.1.1	Electromagnetic Theory . . . . .	40
4.1.2	Heat transfer phenomenon Theory . . . . .	44
4.1.3	Governing equations . . . . .	45
4.2	Electromagnetic simulations in conventional copper conductors . . .	48
4.2.1	Copper tape surrounded by liquid nitrogen . . . . .	48
4.2.2	Copper Tape under AC supply . . . . .	50
4.2.3	Electromagnetic heating . . . . .	54
4.2.4	Copper tape with DC supply (analytical) verification . . . .	57
4.2.5	Comparison between experimental data obtained from a copper tape powered by AC current and data obtained from the software . . . . .	61
4.3	Electromagnetic simulations in superconductors with different for- mulations . . . . .	65
4.3.1	A-formulation . . . . .	65
4.4	Experimental analysis and comparison between data . . . . .	67
4.4.1	Superconducting simulation in DC regime . . . . .	67
4.4.2	Collection of the data and laboratory experience . . . . .	69
4.4.3	Experimental method . . . . .	72
4.4.4	Experimental results . . . . .	74
4.4.5	Second set of data . . . . .	82
4.5	T-A formulation . . . . .	91
4.5.1	Model implemented on the software . . . . .	94
4.5.2	Results . . . . .	98
4.5.3	Discussion and comparison between the two different ap- proaches . . . . .	102
<b>5</b>	<b>Conclusions and future work</b>	<b>105</b>
5.0.1	Conclusions . . . . .	105
5.0.2	Future work . . . . .	106
<b>A</b>		<b>107</b>
	<b>Bibliography</b>	<b>118</b>

# List of Tables

1.1	Main characteristics, advantages and influences of several superconducting power apparatus . . . . .	12
4.1	Dimensions of Liquid Nitrogen and Copper Tape . . . . .	49
4.2	Thermal and Electrical Conductivity of Liquid Nitrogen at 77 K . . . . .	51
4.3	Limits of $J_{\text{rms}}$ for Copper Tape at Different Temperatures . . . . .	52
4.4	Comparison of Magnetic Field $B(T)$ from Software and Computed Values . . . . .	53
4.5	Comparison of Magnetic Field $B(T)$ from Comsol and Computed Values . . . . .	54
4.6	Comparison of Magnetic Field $B(T)$ from Comsol and Computed Values . . . . .	60
4.7	Comparison of Magnetic Field $B(T)$ from Comsol and Computed Values . . . . .	61
4.8	Measured peak values of Current and Voltage at the Secondary with Load . . . . .	62
4.9	Superconductor parameters . . . . .	68
4.10	First set of experimental data . . . . .	73
4.11	Optimal values of the variables in order to minimize the MSE . . . . .	81
4.12	Second set of experimental data . . . . .	83
4.13	Optimal values of the variables in order to minimize the MSE . . . . .	90
4.14	Dimensions of the tape and surrounding air . . . . .	95
4.15	Physical properties of materials . . . . .	95
4.16	Relationship between Current $I_s$ and Electric Field. . . . .	98

# List of Figures

1.1	Meissner effect . . . . .	1
1.2	Critical surface . . . . .	3
1.3	Evolutions of superconducting materials in time[5] . . . . .	4
1.4	Cross section of REBCO tape . . . . .	6
1.5	A superconducting coil for the big european Bubble Chamber magnet	7
1.6	Design of (MHD) . . . . .	7
1.7	(MHD) working principle . . . . .	8
1.8	homopolar sketch DC machine . . . . .	9
1.9	AC synchronous superconductor machine . . . . .	10
1.10	Magnetic levitation 1 . . . . .	10
1.11	Magnetic levitation 2 . . . . .	11
2.1	Comparison between pure superconductor and non-superconductor	15
2.2	Quantized vortices in superconductor(1) . . . . .	16
2.3	Quantized vortices in superconductor(2) . . . . .	16
2.4	Block diagram-how dealing with them [7] . . . . .	19
2.5	structure of a radial flux fully-superconducting synchronous machine [1] . . . . .	22
2.6	Magnetic gear in which iron pieces are replaced by HTS bulks [1] .	24
2.7	Schematic of the bulk-type fully-superconducting synchronous motor[1]	25
2.8	Schematic of a hysteresis machine with HTS bulk.[1] . . . . .	27
3.1	Scheme of magnetic circuit[8] . . . . .	29
3.2	Scheme of how the force is generated on the rotor[9] . . . . .	31
3.3	quadrature magnetic axis and direct magnetic axis[10] . . . . .	32
3.4	Theoretical and practical view of an induction motor[13] . . . . .	34
3.5	Steady-state torque-speed curve for a synchronous motor supplied at constant frequency. [14] . . . . .	38
3.6	Torque-angle curve for a salient pole excited rotor motor. [14] . . .	38
3.7	Typical torque-speed characteristic. [14] . . . . .	39

4.1	Geometry of the model . . . . .	48
4.2	Starting mesh . . . . .	49
4.3	Refined mesh . . . . .	49
4.4	Initial conditions for magnetic and thermal problem . . . . .	50
4.5	Magnetic insulation on all nitrogen boundaries . . . . .	50
4.6	Thermal insulation on all nitrogen boundaries . . . . .	50
4.7	Waveform I (A) (input signal) . . . . .	51
4.8	$J_{RMS}$ . . . . .	52
4.9	B(T) at time step $t=0,003648(s)$ . . . . .	53
4.10	Magnetic field at $t=0,01(s)$ . . . . .	54
4.11	Temperature map at $t=0(s)$ . . . . .	55
4.12	Temperature map at $t=3600(s)$ . . . . .	56
4.13	Relationship Temperature-time . . . . .	56
4.14	Time step function . . . . .	57
4.15	Post-process voltage . . . . .	59
4.16	Magnetic field at 1 (A) . . . . .	59
4.17	current and voltage . . . . .	60
4.18	Magnetic field at 2(A) . . . . .	61
4.19	Voltage signal post-processing at 3.988(A) . . . . .	63
4.20	Voltage signal post-processing at 10(A) . . . . .	64
4.21	Voltage signal post-processing at 16(A) . . . . .	65
4.22	Power law for different values of the exponential constant 'n'[17] . . . . .	67
4.23	Geometry on the software . . . . .	68
4.24	Magnetic field at 160 (A) . . . . .	69
4.25	Superconducting tape setup surrounded by liquid nitrogen and insulator	70
4.26	Superconducting tape setup surrounded by liquid nitrogen and insulator	70
4.27	Superconducting tape while liquid nitrogen is boiling . . . . .	71
4.28	Data collection . . . . .	71
4.29	Voltage as a function of the current . . . . .	74
4.30	E-J experimental curve . . . . .	74
4.31	Fitted experimental and computed voltage . . . . .	75
4.32	Iterative flow chart for the first code . . . . .	77
4.33	Result of the convergence of the algorithm considering the first set of experimental data. . . . .	81
4.34	Plot of the second set of data (E-J curve) . . . . .	84
4.35	Iterative flow chart for the second code . . . . .	86
4.36	E-J curve with Pearson correlation coefficient as O.F . . . . .	87
4.37	Iterative flow chart for the third code . . . . .	89
4.38	E-J curve with Genetic algorithm . . . . .	90
4.39	Measured time of convergence of the algorithm (A-formulation) . . . . .	91

4.40	T computed on the superconductor layer and A computed in the whole domain[23]	93
4.41	Geometry implemented according with T-A formulation.	95
4.42	Initial PDE	96
4.43	Dirichlet on the left side	96
4.44	Dirichlet on the right side	96
4.45	Step function	97
4.46	Schematic matlab code to find best fitting between experimental and simulated power law	98
4.47	T-A power Law	101
4.48	Fitting between experimental data and numerical optimization	102
4.49	Time to converge T-A formulation	102



# Acronyms

**LTS**

Low temperature superconductors

**HTS**

High temperature superconductors

**DC**

Direct current

**AC**

Alternate current

**P**

Power

**R**

Resistance

**I**

electric current

**I.C**

Initial conditions

**O.F**

Objective Function

**MSE**

Mean square error

# Chapter 1

## Introduction

This chapter briefly reviews the fundamental concepts of superconductivity and gives an outline of its current main applications.

### 1.1 Overview of superconductors

In physics, superconductivity is a particular phenomenon, by which under certain characteristics, some kind of materials, become perfect conductors of electricity, this does not mean which the resistance is exceedingly small, it is absolutely equal to zero ( $\Omega$ ). But this is not the only observable phenomenon, these materials also show perfect diamagnetism which means that they expel completely the magnetic field from within, this is known as 'Meissner effect' [1]:

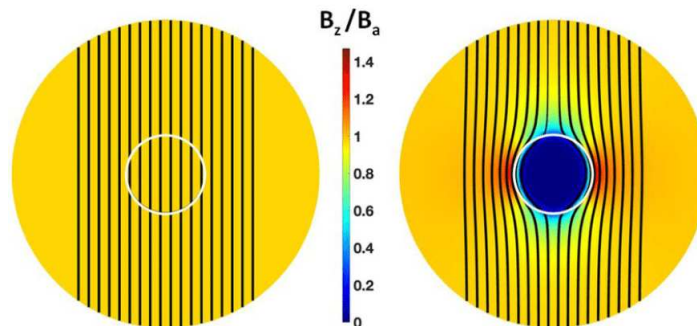


**Figure 1.1:** Meissner effect

The figure above shows the demonstration of the Meissner effect using a superconducting sphere (depicted as a white circle in cross section). When the temperature is above the transition temperature and a static external magnetic field  $B$  is applied in the vertical direction, it permeates uniformly throughout the

normal metal sphere (left, yellow corresponds to  $B_z = B_a$  ). However, below the transition temperature, the superconductor spontaneously expels the magnetic field (right, colors indicate  $B_z / B_a$ ). The illustrations show vertical cross-sectional views through the sphere's center. The colors represent the magnitude of the z-component of the magnetic field, while the black lines depict the streamlines of the magnetic field.[2]

The superconductivity can only be fully explained by delving deep into quantum mechanics, although from an engineering standpoint, a macroscopic approach proves more useful.

This approach leads to reliable studies which can still be conducted in the engineering field, specifically in the research and development of significant ideas and practical applications of global interest.

The phenomenon of superconductivity was discovered in mercury in 1911 by the Dutch physicist Heike Kamerlingh Onnes. He conducted his experiments at cryogenic temperatures using liquid helium, which had been produced a few years prior. Onnes was awarded the Nobel Prize in Physics in 1913 for his achievement in liquefying helium. He observed that at a temperature of 4.2 K, the resistance of mercury vanished. He quickly realized that this discovery could have important scientific applications therefore he started the construction of very large electromagnets which were capable to generate huge fields without power consumption. However, he discovered even that other parameters influenced the 'superconducting state', causing the revert from this state to a normal resistive one.[3]

As a matter of fact, the conditions under which this phenomenon occurs are when some materials are within a 'critical surface' defined by three parameters:

- 1. Critical temperature  $T_C$
- 2. Critical external magnetic field  $H_C$
- 3. Critical current density  $J_C$

This can be appreciated in the figure beneath:

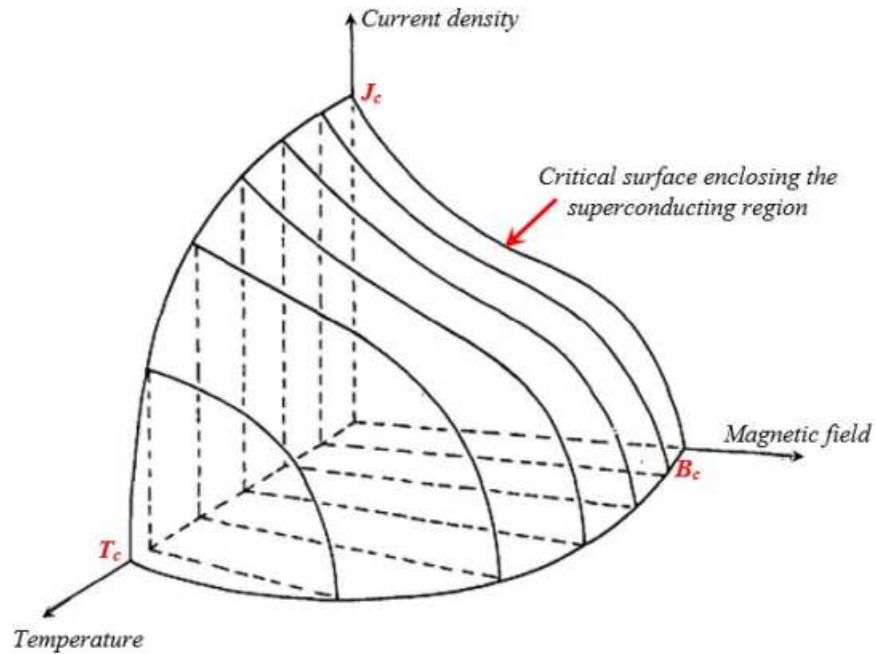


**Figure 1.2:** Critical surface

A distinction in terms of operating temperature between superconductors should be done, there are:

- 1. Low temperature superconductors (LTS): Their very low critical temperature makes them impractical because they require extremely high energy expenditure for refrigeration. As a result, it is often difficult taking advantage from their remarkable properties due to the high costs and technological challenges associated with their implementation.
- 2. High temperature superconductors (HTS)

Usually, the demarcation line between (HTS) and (LTS) is determined by the boiling point of liquid nitrogen, which occurs at 77 K. Liquid nitrogen is widely used due to its low cost.

The previous distinction is a subgroup of the main distinction which takes in account even the number of critical field to surpass in order to enter in the non-superconductive state. This differentiation is basically between:

- 1. Type I superconductors



strong magnetic fields. This characteristic makes them appealing for applications such as rotating machines that rely on high magnetic fields.

As the current through a type II superconductor increases towards the critical current density  $J_C$ , a small resistance begins to emerge. The typical criterion for defining  $J_C$  is an electric field strength of  $E = 1$  ( $\mu\text{V}/\text{cm}$ ).

When exposed to an AC magnetic field or carrying AC current, superconductors generate what is known as "AC losses" which could be very high. This loss arises from both the superconducting and non-superconducting portions of the tape or wire. The ac loss in superconductors is a result of the hysteresis caused by the motion of vortices in type II superconductors under the influence of AC magnetic fields or currents and even due to additional causes which will be analyzed later on.[1]

In order to delve into a more detailed understanding of materials that exhibit superconducting behavior, with regard to HTS (High-Temperature Superconductors), they can be divided into two main subcategories.

- 1. Bismuth strontium calcium copper oxide (or BSCCO for short)
- 2. Rare-earth barium copper oxides (or REBCO for short)

It is more interesting to explore the second class (REBCO), since they are the ones that were studied and experimented upon in the laboratory during the development of this thesis.

The typically used rare-earth (RE) element is usually Y (i.e., YBCO) or Gd (i.e., GdBCO). YBCO exhibits a critical temperature of approximately 90 K. To achieve a high current density, a biaxial texture is required, which is accomplished by depositing REBCO on a biaxial substrate. Thus, commercially available REBCO tapes come in the form of coated conductors, where REBCO occupies a thin layer of about  $1\ \mu\text{m}$  within a tape consisting of multiple layers. These layers include a substrate (e.g., Hastelloy or stainless steel) that can be up to  $100\ \mu\text{m}$  thick, a silver protective layer, and typically copper serving as the top and bottom stabilizer layers. These additional layers offer protective advantages in terms of mechanical strength and thermal stability. The critical current of REBCO exhibits high anisotropy and varies significantly based on the orientation of the applied magnetic field relative to the tape. The greatest critical current is observed when the magnetic field is parallel to the wide face of the tape. Compared to Bi-2223, REBCO coated conductors demonstrate higher critical stress and strain levels [1].

It is possible to appreciate in the following figure, which shows a typical section of a REBCO, what has been described previously.

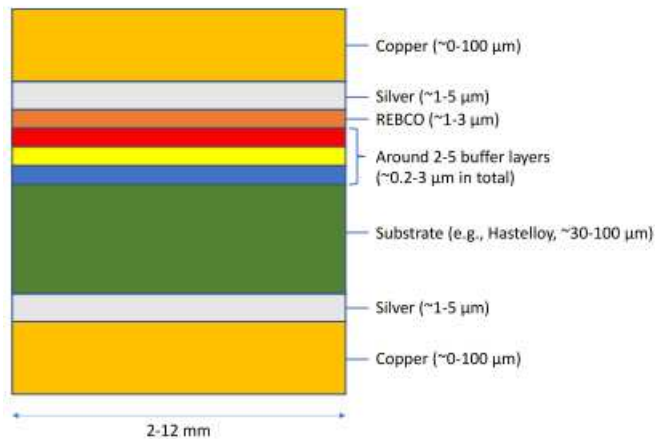


**Figure 1.4:** Cross section of REBCO tape

## 1.2 Applications

Over the years, superconducting magnets have become widely accepted in the research field and a lot of prototypes has been built, although not all of these have found useful and concrete applications. Therefore, starting from the research to concrete engineering applications, it is interesting to report some applications of superconductors to get a general idea of the evolution of the study of these new materials and, consequently, their potential applications in the present and near future, of course, with the necessary technological challenges and barriers to overcome.

- 1. **HIGH ENERGY PHYSICS:** Magnetic fields are very used in physics research to accelerate and analyse the beams of charged particles. If common magnet are used, a laboratory spends around 100 (MW) of electric power. Nowadays the magnets are almost superconductors since taking account the energy to cool down them, they are cheaper with respect to te conventional ones and produce much higher magnetic fields.[6]



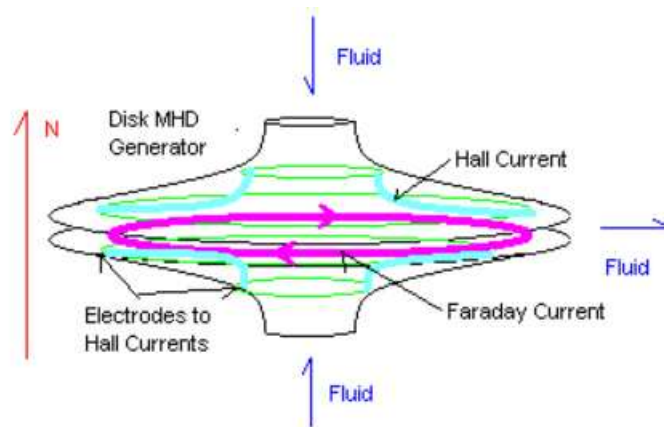


**Figure 1.7:** (MHD) working principle

- 3. DC MOTORS: Superconducting electric motors could be very efficient, smaller in size and lighter. In all prototypes only the the field windings has been made superconducting with the armature remained with conventional material. This is a very efficient idea since the rotating cryostat is avoided but even the energy dissipation due to relative motion between superconductor and field.[6]

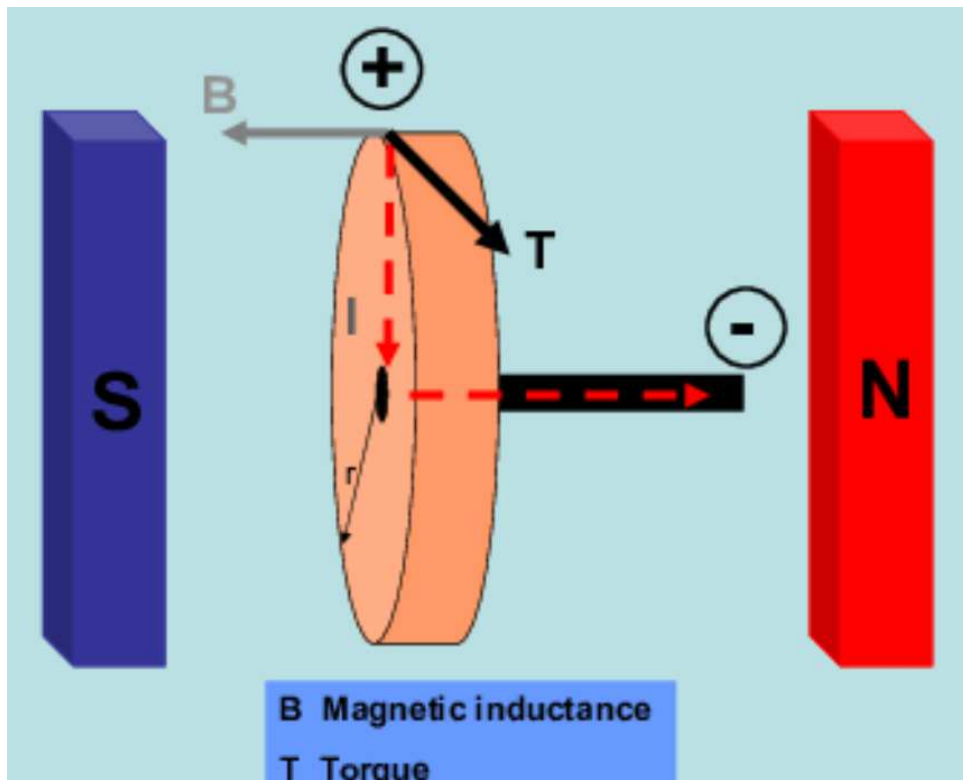
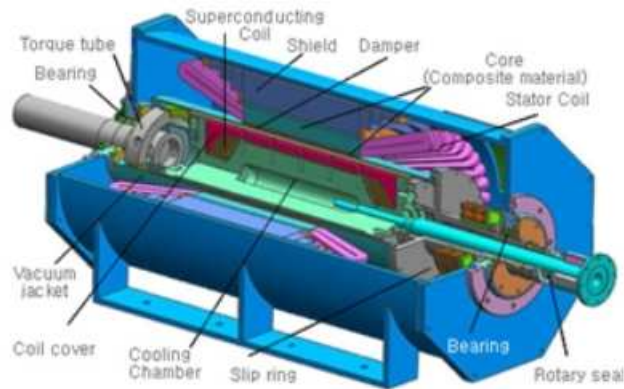


Figure 1.8: homopolar sketch DC machine

- 4. AC MACHINES: Unfortunately, working with an AC current, a lot of losses are involved. Despite the hard challenge, 300 (MW) machines have been built, considering some optimizations and designs and this will be analyzed deeper later on. Under normal operating conditions, the self inductance of the AC coils is quite small but if the AC current is large enough, it will take the iron out of the saturation region which means that the self inductance of the coils will rise a lot, blocking the incipient high current caused by a short circuit.[6]



**Figure 1.9:** AC synchronous superconductor machine

- 5. **MAGNETIC LEVITATION:** Due to the ability of superconductors to produce high fields with low energy consumption, this last application is now attracting attention in several countries, Japan for instance. At high speed, a levitation train moves on a cushion of magnetic field avoiding noise or wear. But a stable levitation can occur only if there is a diamagnetic element in the system. In the trains, this diamagnetism is provided by the eddy currents which tend to repel the train.[6]

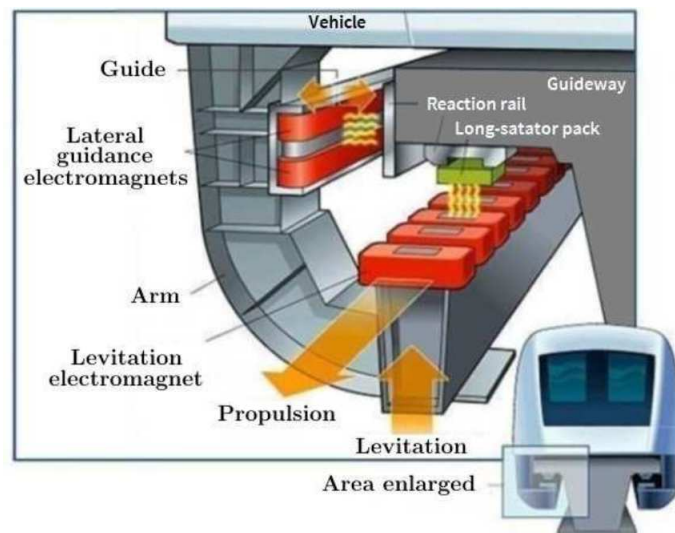


**Figure 1.10:** Magnetic levitation 1

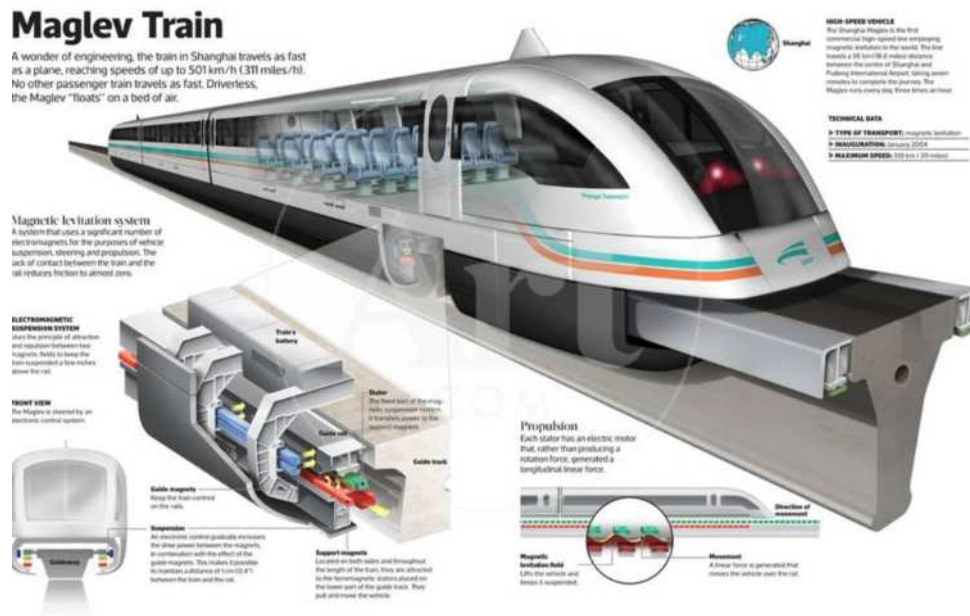


Figure 1.11: Magnetic levitation 2

In the table below it is possible to appreciate the use of some superconductors apparatus:

### 1.2.1 Prospective Developments in Superconductor Applications

#### 1. Advancements in Room-Temperature Superconductivity:

The quest for room-temperature superconductors remains a paramount objective in condensed matter physics. Recent breakthroughs involving hydrides have demonstrated superconductivity at markedly elevated temperatures, bolstering research momentum in this domain. The realization of superconductivity at ambient conditions is anticipated to herald a transformative era in the integration of superconductive materials into consumer electronics, transportation networks, and electrical power infrastructure.

#### 2. Paradigm Shift in Energy Transmission Efficiency:

Superconductive technologies are anticipated to be instrumental in the evolution of energy systems, particularly through the establishment of smart grids characterized by enhanced stability and efficiency. Such grids promise the facilitation of long-distance, low-loss transmission of renewable energy. The integration of superconductors into the energy grid is expected to be pivotal

**Table 1.1:** Main characteristics, advantages and influences of several superconducting power apparatus

<b>Apparatus</b>	<b>Characteristics</b>	<b>Advantages and Influences on Power System</b>
Cable	(1) High transmission power density (2) Low loss, compact size and light weight (3) Small reactance per unit length	(1) Low voltage, large current and high transmission power density (2) Small occupied urban space
Fault Current Limiter (FCL)	(1) Zero resistance in normal state and large impedance in fault state (2) Combination of detection, trigger and limiting current (3) Fast response (4) No harmful effect on power grid	(1) Enhanced stability of the grid (2) Improved reliability of power supply (3) Protected electrical apparatus (4) Reduced cost of construction and retrofit (5) Increased transmission capacity of the grid
Transformer	(1) High power density (2) Low loss, small volume and light weight (3) Liquid nitrogen cooling and insulation	(1) Reduced area of installation (2) Fulfilling requirements for environmental protection and energy saving (3) Noninflammable
Generator	(1) High capacity density (2) Low loss, small size and light weight (3) Low synchronous reactance (4) High overload ability	(1) Reduced energy loss and occupied area (2) Improved stability of the power system (3) Compensated reactive power, improved power quality and stability of grid
Motor	(1) High capacity density (2) Low loss, small size and light weight	(1) Reduced energy loss and occupied area (2) Improved efficiency
Magnetic Energy Storage (SMES)	(1) Fast response (2) High conversion efficiency (3) Able to provide high power to grid in short time	(1) Fast power compensation (2) Enhanced dynamic stability of the grid (3) Improved power quality (4) Improved reliability of power supply

for optimizing interconnectivity and supporting the proliferation of sustainable energy solutions.

**3. Superconductors in Quantum Information Science:**

The integration of superconductive materials in quantum information systems is proving to be of critical significance. Superconducting quantum interference devices constitute a cornerstone in the architecture of nascent quantum computing technologies, serving as the basis for quantum bits (qubits). The advancement of superconductivity in this field is likely to catalyze computational capabilities, enabling the resolution of algorithms that are currently intractable for classical computational frameworks.

**4. Innovations in Superconductive Transportation Modalities:**

The application of superconductivity is poised to extend beyond maglev transportation systems. Notably, the automotive sector could experience a renaissance through the adoption of superconductive motors, which offer advantages in terms of mass and efficiency. Similarly, the aerospace industry may benefit from enhanced propulsion mechanisms underpinned by superconductive technologies, potentially decreasing reliance on conventional fuels and mitigating the carbon footprint of air travel.

# Chapter 2

## Literature review

In this chapter, a general overview of superconductors is provided, their behavior, criticalities, and possible applications are discussed.

### 2.1 Fundamental theoretical concepts of superconductors

The study of superconductors in DC regime is considerably easier with respect to the AC regime. This is quite evident due to the intrinsic nature of the phenomenon.

#### 2.1.1 Losses in superconductors

In superconductors, as has been mentioned in the first chapter, the research on them is continuously growing and the study of their behavior is more complex as it will be shown more in detail.[7]

Concerning the study of losses, some key additional concepts have to be added:

- 1. **Zero Electrical Resistance:** Superconductors, by definition, have zero electrical resistance when they are below their critical temperature. This means that, in an ideal case, there would be no resistive (Joule) heating in a superconductor.

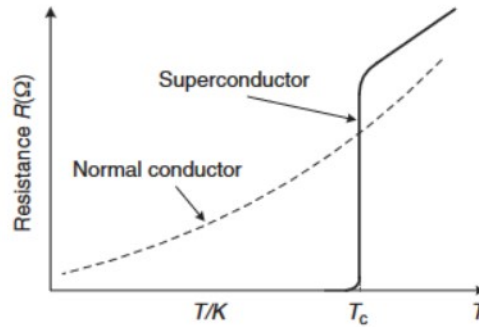


**Figure 2.1:** Comparison between pure superconductor and non-superconductor

- **2. Perfect Diamagnetism (Meissner Effect):** Superconductors expel all magnetic fields from their interior, during the process which leads the materials in a superconductive state.
- **3. AC Losses:** While ideal superconductors would have no losses, real-world superconducting materials can have AC losses, especially when they are carrying AC currents or exposed to AC magnetic fields. These losses can come from several sources, including resistive losses in regions of the material that are not fully superconducting, losses due to flux penetration into the superconductor, and losses due to the movement of vortices in type-II superconductors. Vortices refer to quantized magnetic flux lines that penetrate a type-II superconductor when the applied magnetic field is between the lower and upper critical fields ( $H_{c1}$  and  $H_{c2}$ ). In a type-II superconductor, when the magnetic field is less than  $H_{c1}$ , the superconductor exhibits perfect diamagnetism, meaning it expels all magnetic fields (the Meissner effect). However, when the magnetic field is between  $H_{c1}$  and  $H_{c2}$ , magnetic flux begins to penetrate the superconductor in the form of vortices. Each vortex carries a quantum of magnetic flux, and the region inside the vortex core behaves like a normal (non-superconducting) metal. These vortices can move in response to an applied current or changes in the magnetic field, and their movement can cause energy loss, leading to what is known as vortex dissipation or flux flow resistance. This is one of the reasons why real-world superconductors can exhibit losses, especially at high frequencies or in high magnetic fields.

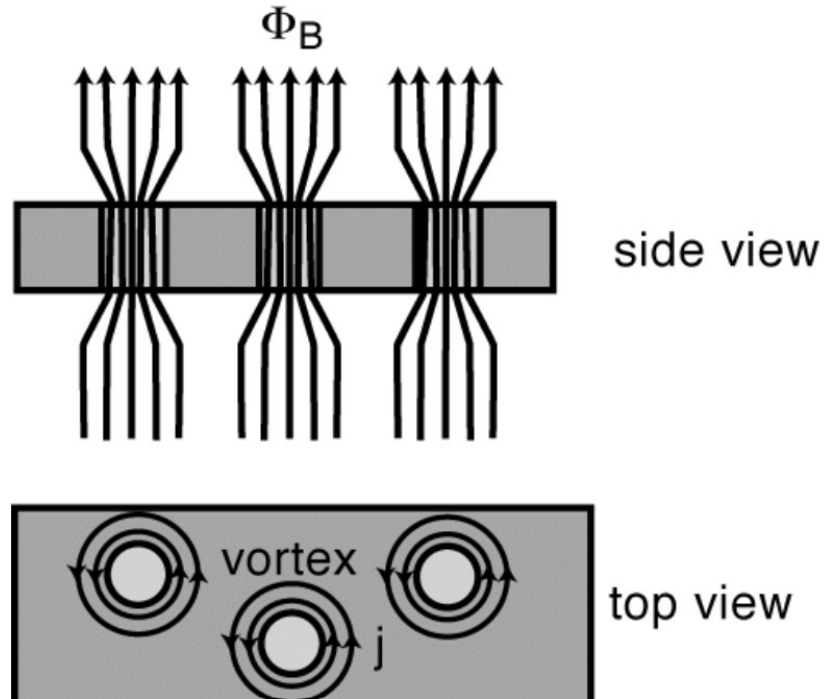


Figure 2.2: Quantized vortices in superconductor(1)

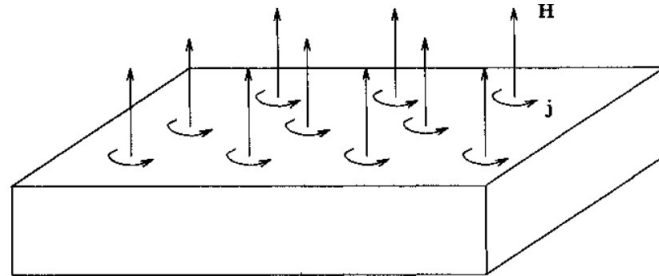


Figure 2.3: Quantized vortices in superconductor(2)

- 4. **Effect of Geometry:** The geometry of the superconducting material can also affect its losses. For example, a superconducting tape or wire can have different losses than a bulk superconductor.

## 2.2 Mathematical formulations

There are some basic mathematical formulations in order to develop a superconducting model and understand the behavior.

Depending on the field of study, these mathematical formulations will lead research to develop more accurate models, and as a result, superconductors can be increasingly employed in all fields where there are currently technological and scientific limitations. As was mentioned in the previous chapter, this phenomenon can be explained in a more accurate way passing through quantum physics, an important mathematical theory recognized as reliable is the 'BSC theory' which is able to explain well the Meissner effect.

Concerning the field of interest from the engineering point of view, it may be more useful dealing with 'macroscopic theories', like the Bean's model of superconductivity

## 2.3 Superconducting electrical machines

### 2.3.1 Advantages and Challenges of Superconducting Technologies in Electrical Machines

First of all, it is important to consider the advantages and disadvantages of the implementation of superconductors in the electrical machines, since nowadays, the research about them is still one of the main topics and issues studied and analyzed in the science field and surely in the near future, the challenges will become less restrictive and the real potential of this phenomenon and consequently the applications will become really huge, but for now it is relevant to put in evidence the level achieved in terms of technological applications.

The main advantages are quite evident:

- **Improved Efficiency through Zero DC Resistance:**  
Superconducting materials exhibit zero direct current (DC) resistance when in their superconducting state. This virtually eliminates ohmic losses when used as a magnet with a DC current, like the rotor field winding in an electrical machine.
- **High Current Density:**  
These materials can carry significantly higher current densities than traditional copper conductors. This allows for a reduction in the volume and mass of the conductor used in the machine.
- **Reduced Iron Content:**  
The ability of superconductors to generate extremely high magnetic fields means that the machine can be designed with less or even no iron content, cutting down on weight and eliminating or minimizing iron-related losses.

- **Superior Magnetic Fields in PM Equivalents:**  
Bulk superconductors and stacked tapes can produce magnetic fields that are orders of magnitude greater than those generated by conventional permanent magnets (PMs).
- **Special Characteristics in HTS Machines:**  
High-temperature superconducting (HTS) machines show high efficiency even at partial loads, exhibit low synchronous reactance, and possess a high overload capacity, features not commonly found in copper-based machines.

As it has been mentioned above, there still some challenges to overcome like the ones listed below:

- **AC Losses:**  
Superconductors are susceptible to AC losses when carrying alternating current (AC) or when exposed to fluctuating magnetic fields. This has restricted their use in machines armature.
- **Legacy Design Constraints:**  
Early low-temperature superconducting (LTS) machines faced significant thermal losses due to AC currents, which led to a design architecture that persists today, featuring a superconducting rotor and a normally-conducting stator.
- **Cooling Requirements:**  
The energy required for cryogenic cooling is substantially higher than the actual losses incurred, thus reducing the net efficiency of the machine. For instance, extracting 1 watt of heat at 77 Kelvin needs 12 to 20 watts of cooling energy.
- **Mechanical Limitations:**  
Superconducting wires and tapes have limited mechanical strength and allowable bending radii, which places additional constraints on machine design.
- **Quenching Risks:**  
The potential for a sudden loss of superconducting state, known as a quench, due to thermal disturbances, poses a reliability and safety concern.
- **Issues with PM Analogues:**  
Using bulk or stacked tapes as PM analogues requires the application and removal of large external magnetic fields for magnetization. Although this has been done successfully, the trapped magnetic fields have yet to reach the full potential of the material. Additionally, these materials are sensitive to demagnetization from fluctuating magnetic fields or thermal disturbances.

By addressing these challenges, it is surely possible to unlock the full potential of superconducting technologies in the design of more efficient and compact electrical machines.[1]

In the following block diagram it is possible to visualize how dealing with AC losses and how it is possible to reduce them:

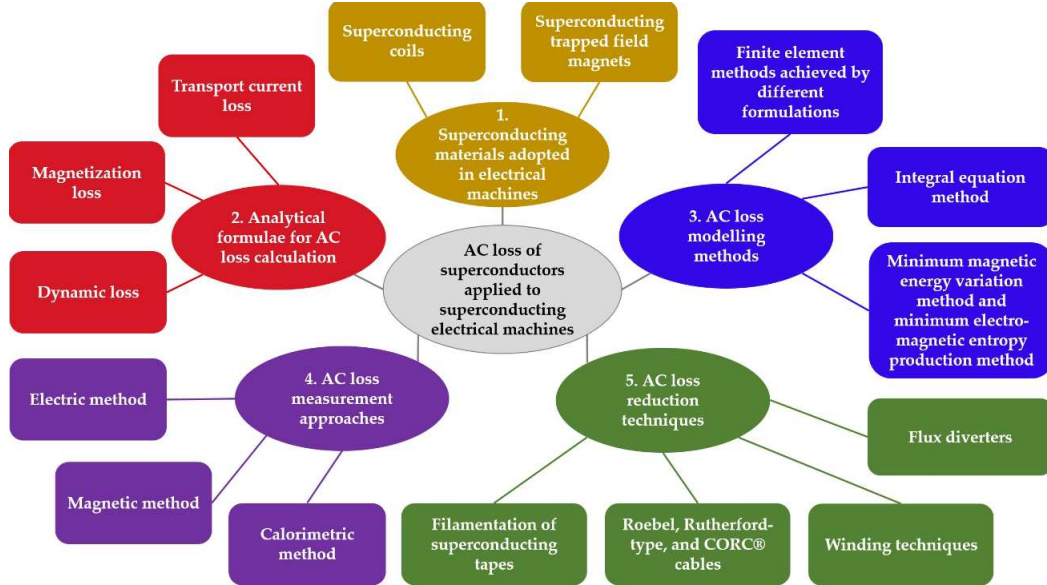


Figure 2.4: Block diagram-how dealing with them [7]

AC loss is indeed a complex phenomenon that significantly impacts the efficiency and performance of superconducting applications.

The diagram breaks down the issue into five interconnected areas, suggesting a comprehensive approach to tackling AC losses:

- **Superconducting materials in electrical machines:** This indicates the types of superconducting materials being used and how their unique properties influence AC loss.
- **Analytical formulae for AC loss calculation:** These are the theoretical tools and equations that help predict AC losses in different scenarios, providing essential insights for design and optimization.
- **AC loss modelling methods:** Through modeling, engineers can simulate and understand the losses in various operational conditions. Methods like finite element analysis and integral equation methods allow for detailed investigations.

- **AC loss measurement approaches:** To validate models and theory, experimental measurement of AC losses is crucial. This can be done through various methods, including electric, magnetic, and calorimetric techniques.
- **AC loss reduction techniques:** Once AC losses are understood and measured, strategies can be developed to reduce them. This includes material engineering like filamentation of tapes, innovative designs like Roebel cables, and the use of flux diverters.

Together, these areas represent a holistic approach to managing AC losses in superconducting systems, encompassing both theoretical and practical aspects. This is crucial for the development of more efficient and cost-effective superconducting technologies.

### 2.3.2 Machines with HTS wires/tapes

These machines are categorized based on the type of superconducting material used, which includes various forms such as wires, bulks, and stacked tapes. The reason behind this categorization is that the material form significantly influences multiple factors like the machine design itself, analytical methods, numerical simulations, mechanical support systems, and cooling requirements, as well as performance metrics like power density and AC loss.

Most HTS machines using wound wires or tapes are either synchronous machines or machines that can function both as synchronous and induction machines. However, there are also innovative machine designs that do not require rotating cryogenic couplings or slip rings. These include unique configurations like claw pole machines, homopolar machines, flux-switching direct current (DC) machines, and doubly-fed machines, among others.

Two notable types of machines, namely DC and flux modulation machines, also feature stationary windings. For instance, Sumitomo[1] has manufactured DC superconducting motors specifically for electric vehicles (EVs). These motors utilized stationary coils made of Bi-2223 superconductor and stationary iron claw poles to direct the magnetic flux and generate a four-pole magnetic field in the air gap.

Another groundbreaking innovation was the world's first liquid nitrogen-cooled motor, which was a flux modulation machine. It had Bi-2223 coils for both the field and armature. The unique aspect of this motor was its dual-rotor design, sandwiched between the field and armature layers. The iron placed on these rotors modulated the magnetic field. This resulted in the armature coils experiencing a fluctuating magnetic field, thereby inducing a back electromotive force (EMF).[1]. Below, an overview is presented, highlighting some of the most significant developments in superconducting electrical machines.

### 2.3.3 Synchronous machines

HTS synchronous machines boast higher power density when compared to their induction counterparts. This is attributed to the stronger rotor field achievable with HTS coils or bulks. Unlike other machine designs that necessitate iron components, synchronous machines can opt for an ironless construction, reducing the overall weight.

Typically, these machines have an outer stator housing for armature winding and an inner rotor for the DC magnetic field. While some are fully superconducting, partially superconducting models are more prevalent due to concerns about AC losses and cryogenic heat loads. In these models, the rotor field windings are superconducting, while the armature winding is usually conventional.

Although AC losses are generally low in the field winding of a partially superconducting synchronous machine, some losses can still occur due to harmonics in the armature winding.

These machines can be designed with either radial or axial flux topologies. Using iron components can reduce the magnetomotive force (MMF) required but limits the airgap flux density and increases the machine's mass.

Several projects have explored the potential of HTS machines, including Siemens' series of machines and the AMSC ship motors, which have demonstrated superior efficiency. EU-funded projects like Suprapower and EcoSwing have also made significant strides in wind turbine generators.

Design studies have been conducted for fully-superconducting synchronous machines. These studies include aircraft motors, wind turbines, and other applications. Among the design considerations are the use of iron teeth in the stator, winding configurations, and strategies to reduce AC loss.

To further minimize the machine's mass, active shielding techniques have been proposed. These involve adding superconducting wires around the machine to reduce stray magnetic fields. Such designs have been applied in aircraft motors and wind turbine generators.[1]

Concerning DC machines, it could be interesting to observe a typical configuration of a fully-superconducting:

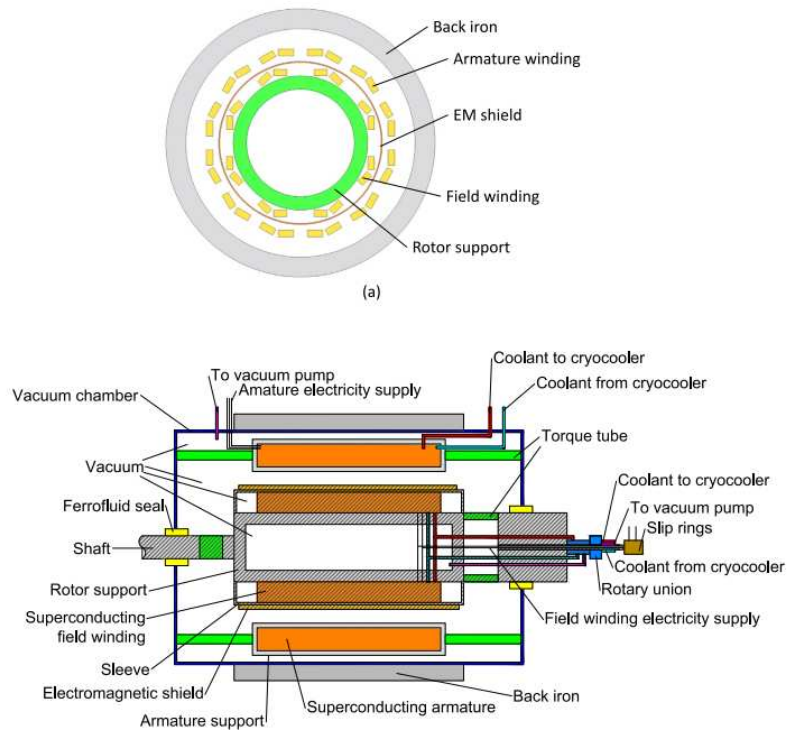


**Figure 2.5:** structure of a radial flux fully-superconducting synchronous machine [1]

### 2.3.4 Induction machines

A team of researchers from Soonchunhyang University discovered that induction motors fitted with High-Temperature Superconducting (HTS) Bi-2223 tapes in the rotor demonstrated superior characteristics. These motors exhibited greater starting torque and efficiency across a variety of loads. This improvement is attributed to the unique properties of HTS materials. Initially, the HTS material undergoes quenching due to the AC current induced by the stator, resulting in higher resistance and subsequently higher starting torque. As the rotor gains speed, the low resistance of the superconductor contributes to high efficiency and minimal slip.

Conversely, researchers at Seikei University modified traditional aluminium rotor bars by adding Bi-2223 tapes to slots in the bars. Although this model didn't operate in synchronous mode, it was observed that the HTS material could trap magnetic flux, a phenomenon later theoretically explored.

Kyoto University researchers have designed a series of motors where HTS-coated

bars replace traditional squirrel-cage rotors. These motors could operate both in slip and synchronous modes, thanks to the zero DC resistance property of superconductors. Most of these prototypes functioned around the temperature of liquid nitrogen, with one unique design intended for liquid hydrogen fuel pumps operating at even lower temperatures.

While most prototypes have been partially superconducting, some have used Bi-2223 for both the rotor and the armature, pushing towards a fully superconducting design. One specific model even featured a dual set of rotor bars and end rings—one made from Bi-2223 and another from copper—enabling its operation at both cryogenic and standard temperatures.[1]

### 2.3.5 Magnetic gears

Magnetic gears were introduced as an alternative to mechanical gears in 2001. Unlike mechanical gears, which are susceptible to wear and friction, magnetic gears can transfer torque between rotating bodies without physical contact. The design includes an inner and outer rotor with permanent magnets (PMs), a stationary layer of iron pieces, and two air gaps.

The iron pieces in the stationary layer modulate the magnetic field of the rotors. This modulation results in magnetic flux density harmonics with varying pole pairs and rotational speeds. The torque is produced when these harmonics with the same number of pole pairs rotate at the same speed. This mechanism allows the two rotors, even rotating at different speeds, to transmit torque to each other.

The possibility of using superconducting tapes instead of PMs has been investigated, showing potential for higher torque density. The use of superconductors alters the operation slightly, as they can saturate and magnetize the iron pieces. As unlike PMs, superconductors have the capability to push the iron pieces into their saturation zones.

Subsequently, a design using only high-temperature superconducting (HTS) coils in the stator was proposed, eliminating PMs altogether. Some other studies have proposed replacing iron pieces in the modulation layer with superconducting bulks to achieve better flux modulation. This design allows for a thinner modulation layer, leading to a lighter gear system.

Analytical studies have been carried out to understand the magnetic field distribution and torque variations in these new designs.[1]

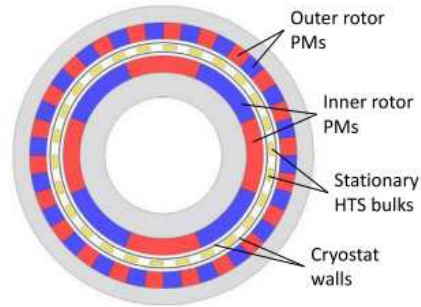


**Figure 2.6:** Magnetic gear in which iron pieces are replaced by HTS bulks [1]

### 2.3.6 Machines with HTS bulks/stacked tapes

Studies, models, and applications related to Machines with HTS bulks/stacked tapes are also significant.

In the list below are explained briefly the different machines and how they work. Bulk HTS materials offer a range of unique properties that can be selectively employed in the design of superconducting machines. Their application is contingent upon the particular property being exploited, be it flux trapping, flux shielding, or flux pinning.

One of the most promising aspects of HTS bulks is their ability to act as Trapped Field Magnets (TFMs). When magnetized, these bulks trap magnetic flux and act similarly to permanent magnets (PMs) in PM synchronous machines. However, TFMs, when it comes to magnetic flux densities—achieve values an order of magnitude higher than conventional PMs, reaching up to 17 Tesla. Therefore, the most significant performance gains in superconducting machines stem from their use as TFMs.

HTS bulks also offer flux shielding capabilities. This attribute has been beneficially employed in reluctance machines, where the magnetic resistance (or reluctance) is a critical parameter. Flux modulation or flux concentration machines also take advantage of this ability. The shielding property allows these machines to guide and concentrate magnetic flux more efficiently, thereby improving their performance.

The property of flux pinning in HTS bulks offers yet another path for machine design, particularly in hysteresis machines. The flux pinning helps in maintaining the magnetization state, which can be a crucial factor in the efficient operation of these types of machines.

It's worth noting that stacked tapes can functionally serve as bulk HTS material, thereby extending the range of design options and applications. This flexibility

allows engineers to consider stacked tapes when bulks are not practical for certain configurations.

In summary, whether it is enhancing the capabilities of existing machine types or enabling new types altogether, HTS bulks stand as a crucial factor element in the field.

- **Trapped field synchronous machines:** In 2005, a team at Tokyo University of Marine Science and Technology (TUMSAT) conducted a series of tests on an axial flux machine that utilized trapped magnetic fields. The machine's rotor was equipped with Gadolinium Barium Copper Oxide (GdBCO) bulks, positioned between dual stators with copper windings. These copper armatures also played a role in magnetizing the GdBCO bulks through a process called in-situ pulsed field magnetization. The machine initially had an output power of 3 kW, which was subsequently increased to 10 kW. Later advancements included a more complex dual-rotor, triple-stator design that boosted the output power to 16 kW and achieved a maximum trapped field of 0.7 Tesla at a rotational speed of 720 rpm.

A noteworthy project was ASUMED, primarily funded by the European Union, which focused on the development of a 1 MW fully-superconducting synchronous motor designed specifically for aerospace applications. The ambitious goal for this project was to achieve a power density of 20 kg/kW. The motor's design featured a stator wound with GdBCO and a rotor equipped with stacked High-Temperature Superconductor (HTS) tapes, functioning as Trapped Field Magnets (TFMs).

Adding some context, the use of superconducting materials like GdBCO and YBCO in these machines allows for greater power density and efficiency, characteristics that are highly desirable in applications ranging from renewable energy generation to electric propulsion systems.[1]

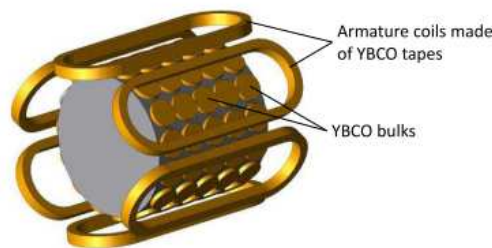


**Figure 2.7:** Schematic of the bulk-type fully-superconducting synchronous motor[1]

- **Hysteresis machines:** Among machines that utilize High-Temperature Superconductors (HTS), hysteresis machines have a notably straightforward design. The rotor in these machines is essentially a cylindrical shell made of HTS bulk material. The armature, typically made of copper, generates a rotating magnetic field. This results in a fluctuating magnetic field experienced by the rotor's HTS bulk. Unlike other machines that leverage the flux shielding property of HTS, hysteresis machines use the flux pinning capabilities of type II superconductors.

The working principle is:

The HTS bulk undergoes magnetic hysteresis, a phenomenon where the material's magnetization ( $M$ ) and the applied magnetic field ( $H$ ) follow a hysteresis loop. Research has shown that the torque generated in these machines is directly proportional to the area covered by this hysteresis loop. One of the intriguing aspects of hysteresis machines is that they maintain a constant torque-speed characteristic, as hysteresis loss is not affected by the frequency of the applied field.

The mechanics behind torque production are based in the external magnetic field induces a current within the HTS bulk, leading to a magnetization that resists changes imposed by the external field. This creates a misalignment between the instantaneous directions of magnetization of the armature and rotor fields, thereby producing torque. As the rotor reaches synchronous speeds, it is been experimentally verified that a sustained level of synchronous torque exists, contrary to initial expectations.

In terms of real-world applications, a team from the Federal University of Rio de Janeiro, built small-scale prototypes using stacks of HTS tapes coiled in a spiral around the rotor core. These prototypes had a power output of around 200 W. Interestingly, these machines were found to operate in both synchronous and asynchronous modes. The asynchronous mode triggers when the load torque surpasses the pinning torque, leading the HTS material to enter a hysteresis cycle.[1]

The hysteresis machine shares similarities with induction motors in that there's a lag between the magnetic fields generated by the stator and rotor. However, this lag is not dependent on the rotor speed, resulting in a constant torque-speed characteristic. This unique feature makes hysteresis machines an interesting subject for further research and potential applications in areas requiring constant torque.

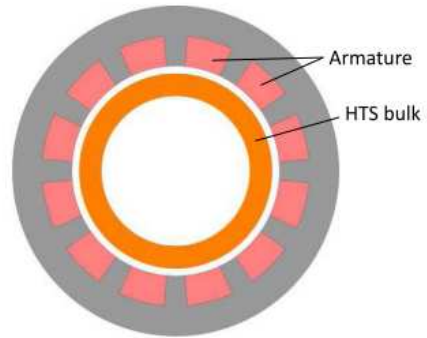


**Fig. 18.** Schematic of a hysteresis machine with HTS bulk.

**Figure 2.8:** Schematic of a hysteresis machine with HTS bulk.[1]

# Chapter 3

## Theoretical foundations

### 3.1 Electromagnetic theory in electrical machines

Electromagnetic theory serves as the foundational framework for the understanding and development of electrical machines.

The field of electrical machine design has undergone significant advancements, particularly due to the introduction of novel materials and computational methods. These innovations have notably enhanced efficiency and facilitated optimal designs. Among these advancements, the incorporation of superconducting materials has shown promise for further improvements in efficiency, thermal performance, and design compactness.

Computational tools based on electromagnetic theory allow for precise modeling and simulation, which are indispensable for incorporating advanced materials like superconductors into machine design.

To understand the potential future directions in this crucial field, a focused overview that covers the key aspects is essential.

#### 3.1.1 Magnetic Circuits

The fundamental equation governing magnetic circuits is analogous to Ohm's Law in electrical circuits:

$$\Phi = \text{mmf} \times \frac{1}{\text{Reluctance (S)}} \quad (3.1)$$

Here,  $\Phi$  is the magnetic flux, mmf is the magnetomotive force, and  $S$  is the reluctance of the magnetic circuit. The reluctance  $S$  is given by:

$$S = \frac{l}{\mu A} \quad (3.2)$$

where  $l$  is the length of the magnetic path,  $\mu$  is the permeability of the material, and  $A$  is the cross-section area.

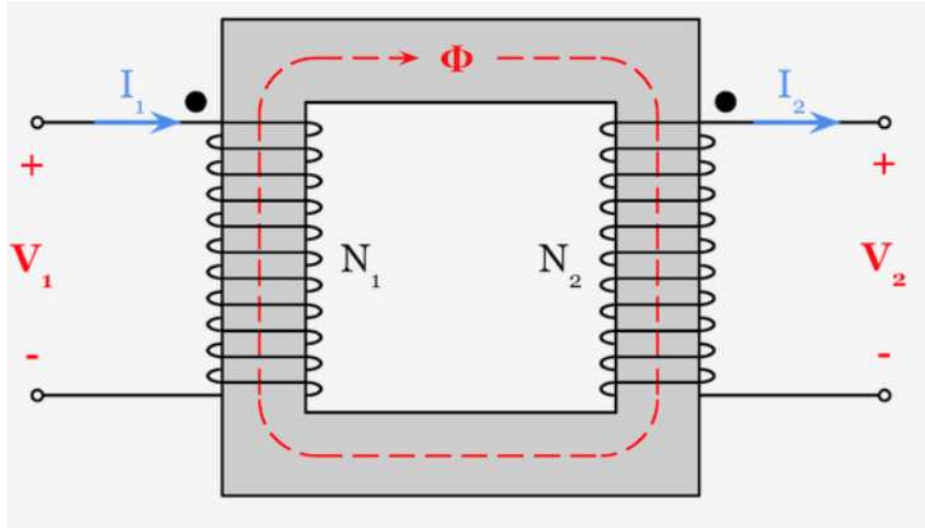


**Figure 3.1:** Scheme of magnetic circuit[8]

Considering a transformer with a closed iron core, if the core has a length  $l$  and cross-sectional area  $A$ , the total reluctance  $S$  of the core can be calculated using (3.2). The magnetic flux  $\Phi$  in the core can then be determined using the magnetomotive force mmf generated by the primary winding.

Electromagnetic induction is the principle by which electrical machines convert mechanical energy into electrical energy and vice versa. Faraday's Law and Lenz's Law are the fundamental principles governing electromagnetic induction. Faraday's Law can be stated as:

$$\text{emf} = -\frac{d\Phi}{dt} \quad (3.3)$$

This equation states that a change in magnetic flux  $\Phi$  through a closed loop induces an electromotive force (emf) in the loop. The negative sign is due to Lenz's Law, which states that the induced emf will always work to oppose the change in flux that produced it.

In the context of electrical machines like motors and generators, this principle is exploited to convert between mechanical and electrical energy. In a motor, a supplied voltage induces a current, which then produces a magnetic field. This magnetic field interacts with the magnetic field of the rotor, generating a torque that turns the rotor. Conversely, in a generator, the mechanical rotation of the

rotor induces a voltage in the stator windings.

Now, let  $N$  be the number of turns in the winding and  $i$  be the current flowing through it. The magnetomotive force (mmf) is given by:

$$\text{mmf} = N \times i \quad (3.4)$$

In a rotating machine, the induced emf in the rotor or stator winding can be represented as:

$$E = N \frac{d\Phi}{dt} \quad (3.5)$$

Additionally it is important to introduce the concept of conversion energy, torque and power as follows:

The energy conversion in electrical machines can be understood using the concept of co-energy  $W'$ , given by:

$$W' = \int_0^i N\Phi di \quad (3.6)$$

Here,  $W'$  is the co-energy stored in the magnetic field, which represents the mechanical energy available for conversion.

The torque  $T$  generated in a machine can be related to the co-energy as:

$$T = \frac{dW'}{d\theta} \quad (3.7)$$

where  $\theta$  is the mechanical angle of rotation. The mechanical power  $P$  is then  $T \times \omega$ , where  $\omega$  is the angular velocity.

### **3.1.2 More details about Torque, Force, Power and dynamic behavior**

The production of torque and force in electrical machines is fundamentally a result of the interaction between magnetic fields. Starting from the trivial Lorentz's Law considering a charge 'q', in electrical machines it is possible to assume that the charges are electrons flowing as a current  $I$  in windings. Therefore, the force on a length  $\ell$  of conductor carrying a current  $I$  in a magnetic field  $B$  is:

$$F = I(\ell \times B) \quad (3.8)$$

In an electric motor, torque is produced by the force generated on the rotor windings due to the stator magnetic field. The torque  $\tau$  is given by:

$$\tau = r \times F \quad (3.9)$$

where  $r$  is the radius of the rotor. For a motor with  $N$  turns and current  $I$ , the torque can be rewritten as:

$$\tau = N \times I \times (A \times B) \quad (3.10)$$

Here,  $A$  is the area vector of the loop, which is perpendicular to the plane of the loop.

In the following figure, a clearer graphical representation of the previously discussed equations is provided.

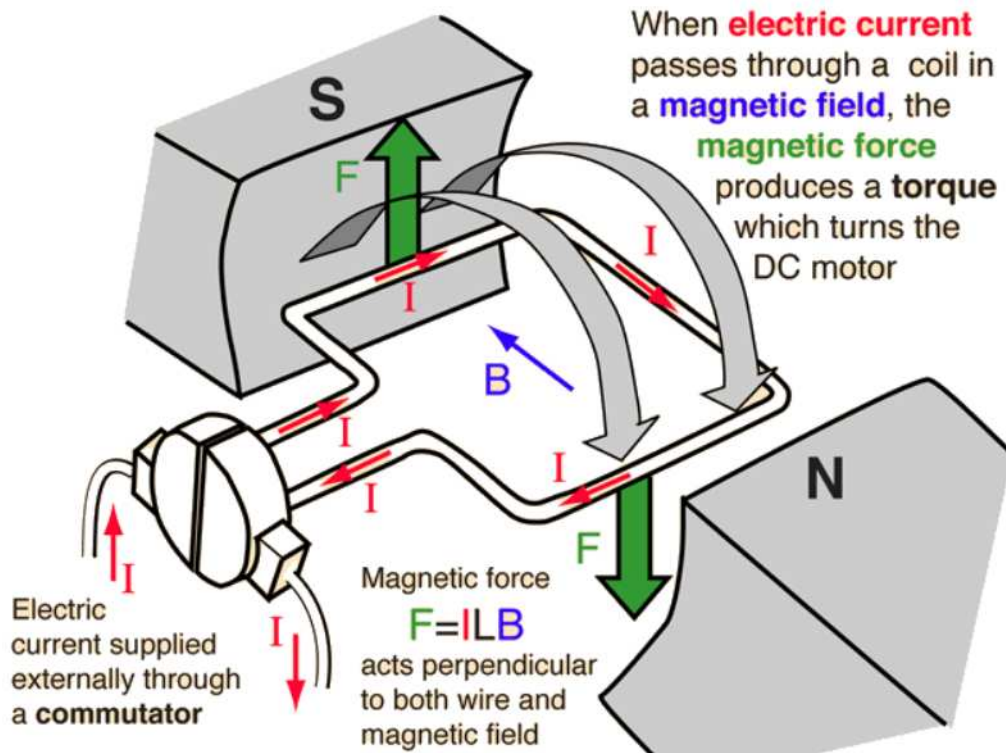


**Figure 3.2:** Scheme of how the force is generated on the rotor[9]

The torque can also be expressed in terms of the magnetomotive force (mmf) and magnetic flux  $\Phi$  as:

$$\tau = \text{mmf} \times \Phi \quad (3.11)$$

For a three-phase motor, the torque  $T$  produced can be modeled as:

$$T = \frac{3}{2} \times p \times (\Psi_d \times i_q - \Psi_q \times i_d) \quad (3.12)$$

where  $p$  is the number of pole pairs,  $\Psi_d$  and  $\Psi_q$  are the d-axis and q-axis flux linkages, and  $i_d$  and  $i_q$  are the d-axis and q-axis currents, respectively.

In the subsequent figure, the significance of the d and q axis flux linkages is illustrated.

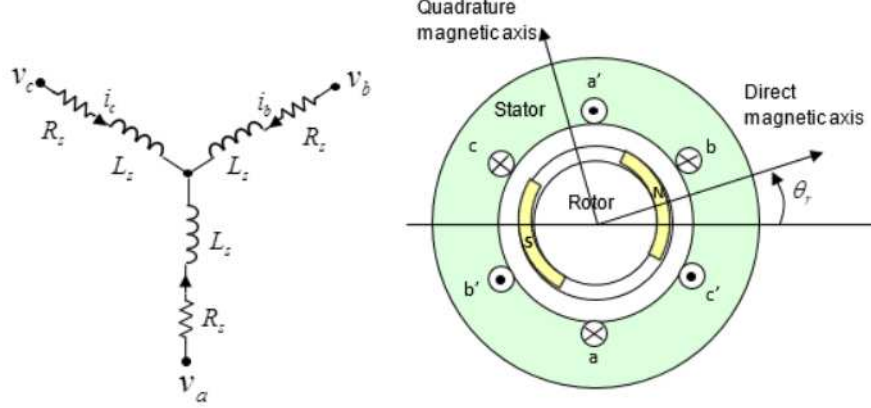


**Figure 3.3:** quadrature magnetic axis and direct magnetic axis[10]

The mechanical power  $P_m$  is related to the torque  $\tau$  and the angular velocity  $\omega$  as:

$$P_m = \tau \times \omega \quad (3.13)$$

The electrical power  $P_e$  is given by  $V \times I$ , where  $V$  is the voltage and  $I$  is the current. The efficiency  $\eta$  of the machine is then:

$$\eta = \frac{P_m}{P_e} \times 100\% \quad (3.14)$$

### Conservation of Energy

The energy conservation principle states that the input electrical power must equal the sum of the mechanical output power and the losses, mainly due to heat and friction:

$$P_e = P_m + P_{\text{loss}} \quad (3.15)$$

It is even important understanding the dynamic behavior of an electrical machine, therefore it is briefly explained.

It can be understood through the second-order differential equation[11]:

$$J \frac{d^2\theta}{dt^2} = \tau - \tau_{\text{load}} - B \frac{d\theta}{dt} \quad (3.16)$$

Here,  $J$  is the moment of inertia of the rotor,  $\tau$  is the electromagnetic torque generated within the machine,  $\tau_{\text{load}}$  is the load torque,  $B$  is the damping constant,

and  $\theta$  is the rotor angle. This equation represents Newton's second law applied to rotational motion, where the net torque is equal to the rate of change of angular momentum.

This equation is explained better subsequently.

The electromagnetic torque  $\tau$  is generated due to the interaction between the magnetic field of the rotor and the stator. This torque aims to align the rotor and stator fields and can be expressed as:

$$\tau = K \cdot i \cdot \Phi \quad (3.17)$$

where  $K$  is a constant of proportionality,  $i$  is the current, and  $\Phi$  is the magnetic flux.

The load torque  $\tau_{\text{load}}$  depends on the mechanical load connected to the machine. For example, in a fan, this torque could be proportional to the square of the angular velocity  $\omega$ :

$$\tau_{\text{load}} = K_{\text{load}} \cdot \omega^2 \quad (3.18)$$

The damping term  $B \frac{d\theta}{dt}$  accounts for losses due to friction and other non-ideal effects.

Combining these into the equation of motion, we get:

$$J \frac{d^2\theta}{dt^2} = K \cdot i \cdot \Phi - K_{\text{load}} \cdot \left( \frac{d\theta}{dt} \right)^2 - B \frac{d\theta}{dt} \quad (3.19)$$

The transient study on electrical machines is really critical since the moment of inertia  $J$  and the damping constant  $B$  become particularly important. When a machine starts, the angular velocity  $\omega$  is zero, and the term  $J \frac{d^2\theta}{dt^2}$  dominates, causing an initial acceleration. As the machine reaches its steady-state, the damping term  $B \frac{d\theta}{dt}$  and the load torque  $\tau_{\text{load}}$  balance out the generated torque  $\tau$ , leading to a constant angular velocity.

In specific cases, like a step change in load or a sudden start, the equation can be solved analytically to give insights into the transient behavior. However, in most practical applications, numerical methods like Runge-Kutta are used for solving this equation, especially when the system is nonlinear or when the load varies with time in a complex manner.

### 3.1.3 Maxwell's Equations in Machine Geometry

Maxwell's equations, typically, in electrical machines, are formulated in spherical coordinate due to the complex geometries, like cylindrical or toroidal shapes, which

necessitate a specialized approach to applying Maxwell's equations.

It is typical to apply the divergence and the curl operators to the potential magnetic field vector  $\vec{A}$  in a cylindrical coordinate system  $(r, \phi, z)$  as follows[12]:

$$\nabla \cdot \vec{A} = \frac{1}{r} \frac{\partial}{\partial r}(rA_r) + \frac{1}{r} \frac{\partial A_\phi}{\partial \phi} + \frac{\partial A_z}{\partial z}, \quad (3.20)$$

$$\nabla \times \vec{A} = \left( \frac{1}{r} \frac{\partial A_z}{\partial \phi} - \frac{\partial A_\phi}{\partial z} \right) \hat{e}_r + \left( \frac{\partial A_r}{\partial z} - \frac{\partial A_z}{\partial r} \right) \hat{e}_\phi + \left( \frac{1}{r} \frac{\partial}{\partial r}(rA_\phi) - \frac{1}{r} \frac{\partial A_r}{\partial \phi} \right) \hat{e}_z. \quad (3.21)$$

These specialized variants of the curl and divergence functions can be integrated into Maxwell's equations to handle the  $r$ ,  $\phi$ , and  $z$  aspects of electric and magnetic fields. This produces a set of partial differential equations, which are the Governing equations, explicitly designed for the cylindrical configurations frequently encountered in electrical machinery.

For instance, considering the Maxwell's equation  $\nabla \times \vec{H} = \vec{J} + \frac{\partial \vec{D}}{\partial t}$ , in cylindrical coordinates this expands to the following one, which is just an example:

$$\begin{aligned} \nabla \times \vec{H} &= \left( \frac{1}{r} \frac{\partial H_z}{\partial \phi} - \frac{\partial H_\phi}{\partial z} \right) \hat{e}_r + \left( \frac{\partial H_r}{\partial z} - \frac{\partial H_z}{\partial r} \right) \hat{e}_\phi + \left( \frac{1}{r} \frac{\partial (rH_\phi)}{\partial r} - \frac{1}{r} \frac{\partial H_r}{\partial \phi} \right) \hat{e}_z \\ &= \vec{J} + \frac{\partial \vec{D}}{\partial t} \end{aligned} \quad (3.22)$$

Indeed, in scenarios such as an induction motor with a squirrel-cage rotor—though not limited to this specific example—Maxwell's equations in cylindrical coordinates prove to be particularly useful. This is due to the cylindrical geometry of both the rotor and the stator.

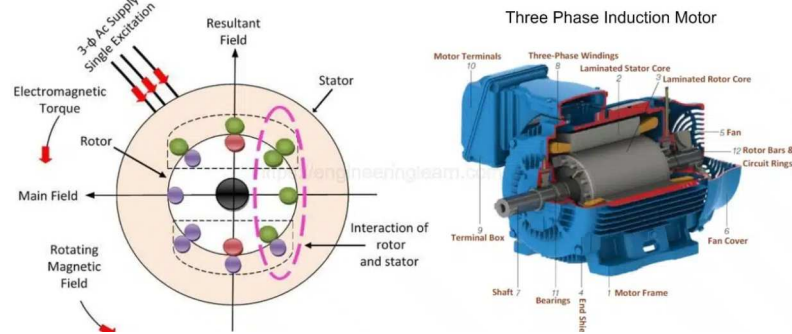


Figure 3.4: Theoretical and practical view of an induction motor[13]

In order to complete the pure mathematical background, aimed at understanding better the usefulness of the computational methods to deal with the complexity of the design of this machines, it could be relevant to highlight that in real-world applications, the complexity introduced by non-uniform materials, winding distributions, and non-linear magnetic characteristics often necessitates approximations. One common simplification involves using the magnetic vector potential  $A$ .

For the relationship between magnetic field  $B$  and magnetic vector potential  $A$ , we have:

$$B = \nabla \times A \quad (3.23)$$

This simplifies Maxwell's equations into a Helmholtz equation for  $A$ :

$$\nabla^2 A - \mu\sigma A = -\mu J \quad (3.24)$$

Here,  $\sigma$  is the conductivity. Equation (3.24) is easier to solve numerically and is often used in conjunction with FEA methods.

### 3.1.4 How the material influence the losses

The material properties significantly affect the performance and efficiency of electrical machines. Understanding the relationships between conductivity, permeability, and core losses is crucial for optimal machine design.

While high conductivity and permeability are generally desired, they often come at the cost of increased core losses and material costs. Therefore, a balanced approach that takes into consideration the performance requirements, cost constraints, and environmental impact is essential for the successful design and operation of electrical machines.

For conductive paths like windings, materials with high electrical conductivity like copper are often chosen, due to their lower resistive losses.

For the core, materials like Silicon Steel, Cobalt-Iron, and Nickel-Iron alloys are commonly used due to their high permeability and low core losses.

It is important, however, which the material choices also have ecological implications, as some high-performing materials can be non-renewable or require energy-intensive manufacturing processes.

It is true that a higher conductivity leads to lower Joule losses but as it was said before, it might increase the machine's cost.

Similarly, higher permeability materials can lead to better performance but can be expensive and have higher core losses. The choice often involves a trade-off.

Concerning the AC losses which happen in the core of the machine, there are some formulations which can help in order to have an idea concerning the optimization, it is clearly always necessary a deep study which implies, numerical simulations, testings, and so on.

The most critical losses in the core are the following ones:

- **Eddy Current Losses** When alternating magnetic fields pass through the core, they induce circulating currents known as eddy currents. These are given by:

$$P_{\text{eddy}} = \pi^2 f^2 B^2 t^2 V \sigma \quad (3.25)$$

Where  $f$  is the frequency,  $B$  is the magnetic flux density,  $t$  is the thickness of the core laminations,  $V$  is the volume, and  $\sigma$  is the conductivity.

- **Hysteresis Losses** These occur due to the constant re-magnetizing of the core material in AC conditions. The loss per cycle is proportional to the area of the hysteresis loop and can be calculated using:

$$P_{\text{hyst}} = \eta B^n f V \quad (3.26)$$

Where  $\eta$  and  $n$  are the known Steinmetz coefficients, and  $V$  is the volume of the core material.

[14]

### 3.1.5 Dynamics in electrical machines

First of all, it is relevant to understand the concept of 'slip' in the electrical machines.

Slip  $s$  is defined as the difference between the synchronous speed  $N_s$  and the rotor speed  $N_r$  as a fraction of the synchronous speed. The equation for slip is given by:

$$s = \frac{N_s - N_r}{N_s} \quad (3.27)$$

Here,  $N_s$  is in revolutions per minute (rpm) or in radians per second, and  $N_r$  is the actual speed of the rotor.[11]

**In synchronous machines**, the rotor speed is equal to the speed of the rotating magnetic field produced by the stator, which is known as the synchronous speed  $N_s$ . Mathematically,  $N_s$  is often given by:

$$N_s = \frac{120 \times f}{p} \quad (3.28)$$

Here,  $f$  is the frequency of the AC supply and  $p$  is the number of poles. Because the rotor speed matches the synchronous speed, the slip  $s$  in a synchronous machine is zero:

$$s = \frac{N_s - N_r}{N_s} = \frac{N_s - N_s}{N_s} = 0 \quad (3.29)$$

This leads to several key characteristics:

- **Constant Speed:** The motor operates at a fixed speed regardless of the load, which is beneficial for applications that require precise speed control.
- **Power Factor Control:** Synchronous machines can operate at leading, lagging, or unity power factor, providing more control over the electrical system.
- **High Efficiency:** With no slip losses, synchronous machines are generally more efficient at converting electrical power to mechanical power, although they are more complex and costly to build and operate.
- **Torque:** In synchronous machines, the electromagnetic torque is in phase with the rotor speed, leading to smooth torque curves.

Mathematically, the power  $P$  and torque  $\tau$  in a synchronous machine is expressed as:

$$P = \tau \times \omega_s \quad (3.30)$$

$$\tau = \frac{P}{\omega_s} \quad (3.31)$$

The load angle, represents the angle by which the rotor magnetic field leads or lags behind the stator magnetic field, and it is a measure of how far the machine is "pulled out" from its synchronous condition. The load angle is directly related to the torque and power output of the machine.

Indeed, the load angle is crucial for stability analysis. A synchronous machine is stable as long as the load angle is within certain limits. Exceeding these limits could lead to loss of synchronism.

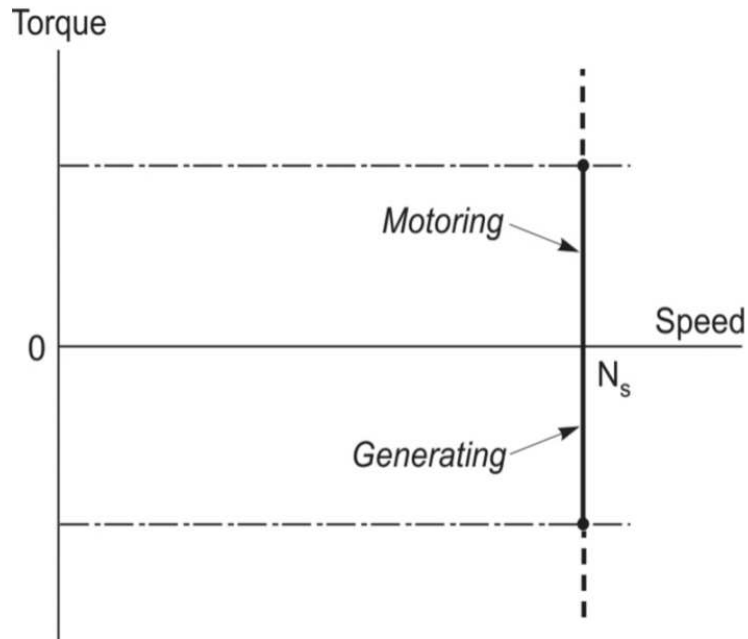


**Figure 3.5:** Steady-state torque-speed curve for a synchronous motor supplied at constant frequency. [14]

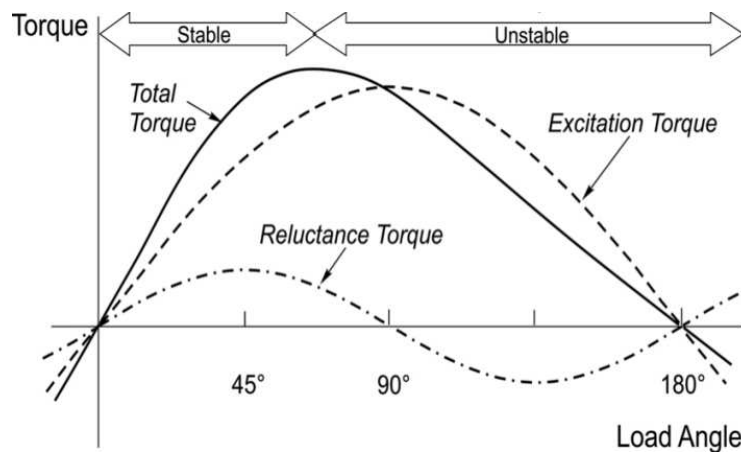


**Figure 3.6:** Torque-angle curve for a salient pole excited rotor motor. [14]

**In asynchronous machines**, the rotor never reaches the synchronous speed. There is always a small difference between the rotor speed  $N_r$  and the synchronous speed  $N_s$ , and this difference is what we refer to as slip  $s$ :

$$s = \frac{N_s - N_r}{N_s} \quad (3.32)$$

The torque produced in an induction motor can often be modeled as a function of slip.

$$\tau = \tau_{\max} \left( \frac{s}{s^2 + 1} \right) \quad (3.33)$$

The relationship between slip and torque can be plotted to create a slip-torque curve. This curve is essential for understanding the motor's performance under different loads. For instance, at  $s=0$ , the torque is zero. As slip increases, the torque also increases, reaching a maximum before decreasing again.

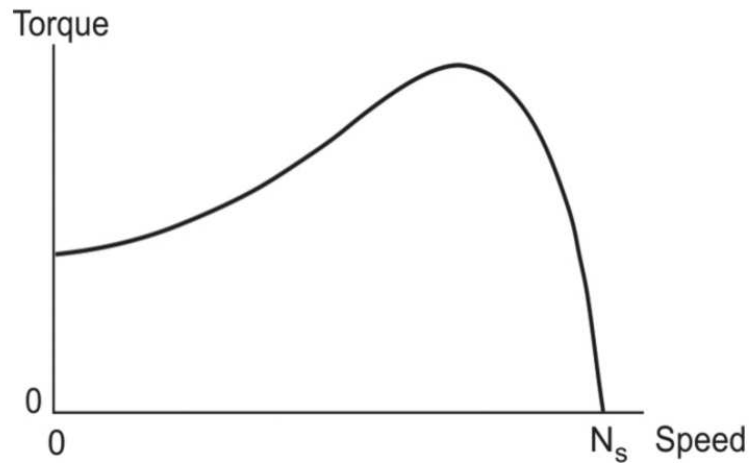


**Figure 3.7:** Typical torque-speed characteristic. [14]

# Chapter 4

## Electromagnetic simulations and experimental results

Prior to exploring the simulations and key research in the field of superconductors, a foundational understanding of the fundamental laws governing electromagnetic phenomena and heat transmission is indispensable. Additionally, an overview of simulation techniques relevant to these phenomena is warranted, as they constitute a cornerstone in contemporary engineering practices. These techniques serve as robust tools for modeling, optimizing, and comprehending complex systems such as superconductivity.

### 4.1 Models and equations used

#### 4.1.1 Electromagnetic Theory

The keystone of electromagnetic theory is the Maxwell's set of equations, four fundamental equations which govern the behavior of electric and magnetic fields. In their differential form, the equations can be expressed as follows:

$$\vec{\nabla} \cdot \vec{E} = \frac{\rho}{\epsilon_0} \quad (\text{Gauss's law for electricity}) \quad (4.1)$$

$$\vec{\nabla} \cdot \vec{B} = 0 \quad (\text{Gauss's law for magnetism}) \quad (4.2)$$

$$\vec{\nabla} \times \vec{E} = -\frac{\partial \vec{B}}{\partial t} \quad (\text{Faraday's law}) \quad (4.3)$$

$$\vec{\nabla} \times \vec{B} = \mu_0 \vec{J} + \mu_0 \epsilon_0 \frac{\partial \vec{E}}{\partial t} \quad (\text{Ampère's law with Maxwell's addition}) \quad (4.4)$$

Here,  $\vec{E}$  and  $\vec{B}$  are the electric and magnetic field vectors,  $\rho$  is the charge density,  $\epsilon_0$  is the vacuum permittivity,  $\mu_0$  is the vacuum permeability and  $\vec{J}$  is the current density.

The equation (4.1) is the Gauss's Law which relate the electric field  $\vec{E}$  to the charge distribution  $\rho$  and it can be written in integral form knowing that it represent the flux of electric field through the surface  $\vec{S}$ :

$$\oint_S \vec{E} \cdot d\vec{A} = \frac{Q_{\text{enc}}}{\epsilon_0} \quad (4.5)$$

To better understand, it is possible to consider a point in the space located in a place arbitrary called 'origin' which own a charge  $q$ .

The electric field  $\vec{E}$  located in a point 'p' in the space at a distance  $\vec{r}$  from the origin is computed by Coulomb's law:

$$\vec{E} = \frac{q}{4\pi\epsilon_0 r^2} \vec{r} \quad (4.6)$$

$$(4.7)$$

Applying the divergence operator on both sides it is possible to obtain:

$$\vec{\nabla} \cdot \vec{E} = \vec{\nabla} \cdot \left( \frac{q}{4\pi\epsilon_0 r^2} \vec{r} \right) = \frac{q}{\epsilon_0} \delta(r) \quad (4.8)$$

Here,  $\delta(r)$  is the Dirac delta function representing the charge at the origin.

Equation (4.8) demonstrates that the divergence of the electric field is non-zero only at the location of the point charge, which is consistent with Gauss's law in differential form.

The equation (4.2) postulates that there are no magnetic monopoles in nature. It means that the magnetic field lines are always closed loops.

In the case of a magnetic dipole, formed by a current loop, the magnetic field lines emerge from the "north pole" and enter the "south pole," completing the loop inside the material. The absence of magnetic monopoles ensures that  $\vec{\nabla} \cdot \vec{B} = 0$ , confirming Gauss's law for magnetism.[15]

The equation (4.2) can be written in the integral form as:

$$\oint_S \vec{B} \cdot d\vec{A} = 0 \quad (4.9)$$

It indicates that the magnetic flux through a closed surface S is always zero as it has been shown before.

The equation (4.3) states that a time-varying magnetic field induces an electromotive force (EMF) or electric field. This is the basis for electromagnetic induction used in transformers, electric generators, and many other applications.

Considering a loop of wire in the presence of a magnetic field  $\vec{B}$  that changes with time, the so called Faraday's law can be expressed in integral form as[15]:

$$\oint_C \vec{E} \cdot d\vec{l} = -\frac{d}{dt} \int_S \vec{B} \cdot d\vec{A} \quad (4.10)$$

This equation shows that a changing magnetic field  $\vec{B}$  induces an electric field  $\vec{E}$  around the loop, generating an (EMF).

The equation (4.4) describes how currents and changing electric fields give rise to magnetic fields.

Considering a parallel plate capacitor being charged with a time-dependent current  $I(t)$ , the magnetic field  $\vec{B}$  in a loop around the wire can be described by Ampère's law as:

$$\oint_C \vec{B} \cdot d\vec{l} = \mu_0 I(t) \quad (4.11)$$

The current  $I(t)$  is time-dependent, indicating that the capacitor is being charged over time. According to Ampère's original law, the magnetic field  $\vec{B}$  generated around a current-carrying wire loop is directly related to this current. However, this original formulation would suggest an infinite electric field between the capacitor plates, which contradicts Gauss's law for electricity. Maxwell amended this inconsistency by introducing a displacement current term  $\mu_0 \epsilon_0 \frac{\partial \vec{E}}{\partial t}$  to Ampère's law. This new term accounts for the changing electric field inside the capacitor and harmonizes the description of both electric and magnetic fields, including their behavior in and around a charging capacitor.

Another important quantity is the Poynting vector  $\vec{S}$  which is a measure of the directional flow of electromagnetic energy. It quantifies the energy transported per unit area in the form of an electromagnetic field and is mathematically expressed as:

$$\vec{S} = \vec{E} \times \vec{H} \quad (4.12)$$

Here,  $\vec{E}$  is the electric field and  $\vec{H}$  is the magnetic field. This vector is particularly useful in applications like power distribution systems and the study of electromagnetic wave propagation.

Considering a plane electromagnetic wave propagating in free space, the Poynting vector will point in the direction of wave propagation. The magnitude of this vector gives the power per unit area carried by the wave, and it is given by:

$$|\vec{S}| = EH \sin(\theta) \quad (4.13)$$

where  $\theta$  is the angle between  $\vec{E}$  and  $\vec{H}$ . For a plane wave in free space,  $\theta = 90^\circ$ , making  $|\vec{S}| = EH$ .

In many problems, even including the study of superconductors formulations, the magnetic vector potential is a crucial quantity. In this work, the used formulations to describe superconductors, A and T-A formulation both have the potential vector A as a state variable.

This vector field is related to the magnetic field  $\vec{B}$  through the curl operator.

$$\vec{B} = \vec{\nabla} \times \vec{A} \quad (4.14)$$

For instance, the definition of this vector can be formally articulated as follows:

Assuming which is predominant the magnetic phenomena with respect to the electric, the differential laws of magnetostatics are:

$$\vec{\nabla} \times \vec{B} = \mu_0 \vec{J}, \quad (4.15)$$

$$\vec{\nabla} \cdot \vec{B} = 0 \quad (4.16)$$

If the current is equal to zero in a bounded region, we immediately have that:

$$\vec{\nabla} \times \vec{B} = 0 \quad (4.17)$$

This allows us to express the magnetic induction  $\vec{B}$  as the gradient of a magnetic scalar potential  $\Phi_M$ :

$$\vec{B} = -\vec{\nabla} \Phi_M \quad (4.18)$$

Substituting the equation (4.18) in (4.17), it is obtained the Laplace equation.

$$\nabla^2 \Phi_M = 0 \quad (4.19)$$

If  $\vec{\nabla} \cdot \vec{B} = 0$  everywhere, then  $\vec{B}$  must be the curl of this magnetic vector field  $\vec{A}(x)$

$$\vec{B}(x) = \vec{\nabla} \times \vec{A}(x) \quad (4.20)$$

The general form of  $\vec{A}(x)$  is given by

$$\vec{A}(x) = \frac{\mu_0}{4\pi} \int \frac{\vec{J}(x')}{|\vec{x} - \vec{x}'|} d^3x' + \vec{\nabla} \Phi'(x) \quad (4.21)$$

This equation describes  $\vec{A}(x)$  as an integral involving the current density  $\vec{J}(x')$  and a gradient term of a scalar function  $\Phi'(x)$ .

The inclusion of the gradient term of a freely chosen scalar function  $\Phi'$  indicates that the vector potential can be uniquely modified as  $\vec{A} \rightarrow \vec{A} + \vec{\nabla} \Phi'$ , while still

maintaining the same magnetic field  $\vec{B}$ . And this could be an issue in the numerical computation as it will be observed later on.

This transformation is called a gauge transformation. The liberty provided by gauge transformations grants us the flexibility to shape  $\vec{\nabla} \cdot \vec{A}$  into any functional form.

If (4.20) is substituted inside (4.15) it is possible to find the following equation:

$$\nabla \times (\nabla \times \vec{A}) = \mu_0 \vec{J}$$

or

$$\nabla(\nabla \cdot \vec{A}) - \nabla^2 \vec{A} = \mu_0 \vec{J}$$

In this particular gauge selection where  $\nabla \cdot \vec{A} = 0$ , each component of the vector potential  $\vec{A}$  fulfills the Poisson equation  $\nabla^2 \vec{A} = -\mu_0 \vec{J}$ .

In a space without boundaries, the vector potential  $A(x)$  is given by the formula

$$A(x) = \frac{1}{4\pi} \int J(x') d^3x' \frac{1}{|x - x'|}$$

where  $\Phi'$  is set to a constant. This constant condition for  $\Phi'$  is explained by our choice of gauge  $\nabla \cdot A = 0$ , which simplifies to  $\nabla^2 \Phi' = 0$ . This is possible because the first term in Equation (4.21) has no divergence, i.e.,  $\nabla \cdot J = 0$ . If  $\nabla^2 \Phi' = 0$  holds throughout space,  $\Phi'$  can only be a constant, assuming there are no sources at infinity.[12]

For a long, straight wire carrying a current  $I$ , the magnetic vector potential  $\vec{A}$  in cylindrical coordinates  $(r, \phi, z)$  is given by:

$$\vec{A} = \frac{\mu_0 I}{2\pi r} \hat{\phi} \tag{4.22}$$

Here,  $\mu_0$  is the permeability of free space. This potential gives rise to the well-known magnetic field  $\vec{B}$  in a circular pattern around the wire.

Understanding these equations in depth, is crucial for any electromagnetic simulation. They provide the mathematical foundation for understanding how electric and magnetic fields interact with charges, currents, and with each other, laying the groundwork for the subsequent numerical methods used to solve these equations in practical applications.

### 4.1.2 Heat transfer phenomenon Theory

The Navier-Stokes equations govern fluid dynamics and are crucial for modeling heat transfer in fluids. These equations represent the conservation of momentum

in a fluid, and they are given by:

$$\rho \left( \frac{\partial \vec{u}}{\partial t} + \vec{u} \cdot \vec{\nabla} \vec{u} \right) = -\vec{\nabla} p + \mu \nabla^2 \vec{u} + \vec{F} \quad (4.23)$$

Here,  $\rho$  is the fluid density,  $\vec{u}$  is the fluid velocity,  $t$  is time,  $\vec{\nabla} p$  is the pressure gradient,  $\mu$  is the dynamic viscosity,  $\nabla^2$  is the Laplacian operator.[16]

As will be discussed in the chapter 5, it is possible to obtain starting from (4.23) the following Energy equation which takes in account explicitly the convection and conduction phenomena, since the generic source 'Q' is hidden:

$$\rho C_p \left( \frac{\partial T}{\partial t} + \vec{u} \cdot \vec{\nabla} T \right) = \vec{\nabla} \cdot (k \vec{\nabla} T) + Q \quad (4.24)$$

Starting from this one, it is interesting to obtain two simplified formulation which could be useful and more easy to handle:

- **In a steady-state situation with no heat generation and a uniform velocity field, the energy equation simplifies to:**

$$\vec{u} \cdot \vec{\nabla} T = \alpha \nabla^2 T \quad (4.25)$$

$\alpha = \frac{k}{\rho C_p}$  is the thermal diffusivity. This equation can be solved for various geometries and boundary conditions to get the temperature distribution.

- **In transient conditions, the time derivative in the energy equation cannot be neglected:**

$$\frac{\partial T}{\partial t} = \alpha \nabla^2 T + \frac{Q}{\rho C_p} \quad (4.26)$$

And on this way it is possible to describe how the temperature changes with respect to time due to conduction and any internal heat generation.

This result is a good step to understand better how the numerical simulations work.

### 4.1.3 Governing equations

At this juncture, it becomes imperative to understand the coupled phenomenon of 'electromagnetic heating.' Consequently, further elaboration on this topic is essential.

While Maxwell's equations in vacuum provide the foundation for electromagnetic theory, engineering applications often involve materials with distinct electrical properties. In material media, Maxwell's equations are modified to:

$$\vec{\nabla} \cdot \vec{D} = \rho_f \quad (4.27)$$

$$\vec{\nabla} \cdot \vec{B} = 0 \quad (4.28)$$

$$\vec{\nabla} \times \vec{E} = -\frac{\partial \vec{B}}{\partial t} \quad (4.29)$$

$$\vec{\nabla} \times \vec{H} = \vec{J}_f + \frac{\partial \vec{D}}{\partial t} \quad (4.30)$$

Here,  $\vec{D} = \epsilon \vec{E}$  is the electric displacement field,  $\epsilon$  is the permittivity of the material,  $\rho_f$  is the free charge density,  $\vec{H} = \frac{1}{\mu} \vec{B}$  is the magnetic field intensity,  $\mu$  is the permeability, and  $\vec{J}_f$  is the free current density.  $\vec{D}$  and  $\vec{B}$  are even called electric and magnetic flux densities.

In thermal simulations involving temperature-dependent properties or non-isothermal conditions, the energy equation takes the form:

$$\rho C_p \left( \frac{\partial T}{\partial t} + \vec{u} \cdot \vec{\nabla} T \right) = \vec{\nabla} \cdot (k \vec{\nabla} T) + Q - \rho E \frac{\partial \phi}{\partial t} \quad (4.31)$$

Here,  $\vec{E}$  is the electric field, and  $\phi$  is the electric potential. The last term represents the Joule heating due to electric fields, which is vital in applications like resistive heating or induction.

Now, this passage is really important, since it is possible to understand how software like COMSOL handle phenomena like this starting from a precise formulation.

In systems where electromagnetic and thermal phenomena are interdependent, the governing equations become coupled. For instance, in an induction heating system, the electromagnetic fields generate heat, affecting the material properties and, in turn, the electromagnetic fields. The coupled equations can be written as:

$$\vec{\nabla} \times (\mu(T) \vec{\nabla} \times \vec{E}) - \epsilon(T) \omega^2 \vec{E} = -\omega \vec{J} \quad (4.32)$$

$$\rho C_p \frac{\partial T}{\partial t} = \vec{\nabla} \cdot (k(T) \vec{\nabla} T) + Q(T, E, J) \quad (4.33)$$

Here,  $\mu(T)$ ,  $\epsilon(T)$ , and  $k(T)$  are the temperature-dependent permeability, permittivity, and thermal conductivity, respectively.  $Q(T, E, J)$  is the heat generation term, which can be a function of temperature, electric field, and current density. It result really important to observe the variable In the formula  $\omega$ , which represents the angular frequency of the electromagnetic field. Angular frequency is related to the regular frequency  $f$  by the equation  $\omega = 2\pi f$ .

In the context of the coupled electromagnetic and thermal equations,  $\omega$  is often used to describe oscillating or time-varying electromagnetic fields. It appears in the equation to account for the time-dependent behavior of these fields, particularly when you're dealing with phenomena like induction heating.

Angular frequency is an important parameter because it can affect both the electromagnetic behavior of the system and its thermal characteristics. For instance, at high frequencies, skin effects might dominate, leading to heating mostly at the surface of a conductor. This in turn affects how the thermal equation will behave because the heat source (Joule heating) is frequency-dependent.

Indeed, considering an electromagnetic wave propagating through a medium with temperature-dependent electrical conductivity  $\sigma(T)$ . The heat generated due to the wave can be given by:

$$Q = \sigma(T) |\vec{E}|^2 \quad (4.34)$$

This heat source will affect the temperature distribution, which in turn modifies  $\sigma(T)$ , creating a feedback loop that can only be solved using coupled equations.

Obviously, the governing equations are partial differential equations (PDEs) that require appropriate boundary and initial conditions for a unique solution. For instance, in electromagnetic simulations, Dirichlet or Neumann boundary conditions might specify the electric or magnetic fields at the boundaries. In thermal simulations, the temperature or heat flux could be defined at the boundaries. In addition, in many engineering applications, especially those involving complex materials like superconductors or phase-changing materials, the governing equations can be non-linear and time-dependent.

Therefore, understanding the governing equations is the key of any simulation in engineering. These equations define the mathematical framework within which the physical phenomena operate. Maxwell's equations govern electromagnetic behavior, modified by the material properties and possibly coupled to thermal effects. The energy equation, often coupled with the Navier-Stokes equations for fluid flow, dictates the thermal behavior. Boundary and initial conditions, as well as non-linearities and time-dependence, add layers of complexity and starting from here.

## 4.2 Electromagnetic simulations in conventional copper conductors

The purpose of the initial numerical simulations was to approach the main problem in steps, in order to gain proficiency with the COMSOL software and verify the results by comparing them with theoretical physical models. This allowed for subsequent comparisons, commentary, and considerations between the behavior of materials that do not exhibit superconducting properties and those that do under appropriate conditions.

Numerical simulations were performed on a copper tape subjected to both direct and alternating current, analyzing electromagnetic and energetic behaviors under different conditions. These simulations will be summarized and discussed below. It is important to highlight that the size of the tape has been kept equal in each simulation which coincides with the size measured in the laboratory. On this way, it is possible to observe the relevant differences in terms of thermal and electromagnetic effects, in particular the width the height and the length of the tape have been set respectively to 6.8(mm), 0.8 (mm) and 0.21(m).

### 4.2.1 Copper tape surrounded by liquid nitrogen

As a first step, the geometry considered was a copper tape surrounded by 1 ( $m^3$ ) of liquid nitrogen but considering the low electrical and thermal conductivity of the fluid, physical effects are very negligible. Therefore, the volume of liquid nitrogen surrounding the copper tape was reduced to  $8.4 \times 10^{-5}$  ( $m^3$ ), in particular, this volume corresponds to a square with edge equal to 0.02 (m) multiplied by an orthogonal length of 0.21(m), in order to observe more significant results. In the picture and in the table beneath is shown the geometry of the model.

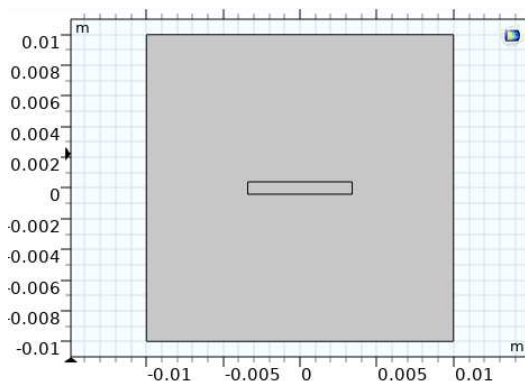
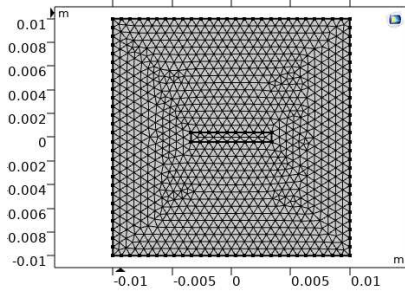


Figure 4.1: Geometry of the model

**Table 4.1:** Dimensions of Liquid Nitrogen and Copper Tape

	Liquid Nitrogen (m)	Copper Tape (m)
Height	0.02	$0.8 \times 10^{-3}$
Width	0.02	$6.8 \times 10^{-3}$
Length	0.21	0.21

An adaptive mesh refinement is adopted in almost all simulations in order to obtain more accurate values in particular in the regions of interest. This implies more computational time, therefore, in some superconductor simulations it is avoided due to the non-linearity of the problem itself and an extra-refined mesh would require too much time and power. The difference between the starting mesh and the refined one is shown in figures (4.2) and (4.3) respectively.



**Figure 4.2:** Starting mesh

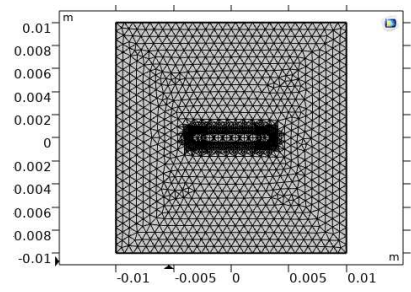


**Figure 4.3:** Refined mesh

The copper tape properties such as the heat capacity at constant pressure ( $C_p$ ), the density and the thermal conductivity ( $K$ ), are modified on the software defaults values since it works at an initial temperature equal to 77 (K).

The 'physics' added on the software are:

- a) Magnetic fields, which solves the problem for the magnetic vector potential, also known as A formulation.
- b) Heat transfer in solids, which solves for temperature field as it was explained in the previous section.

As a matter of fact, all the studies are focused on the coupled interface 'electromagnetic heating', which means that the coil works as a resistive heater, coupling the electromagnetic behavior with the heat transfer equations.

For both heat problem and magnetic problem, boundary conditions and initial conditions are added.

The initial value for the thermal problem is set at the temperature

$$T_0 = 77(K) \tag{4.35}$$

and the initial value for the magnetic problem is set at the potential magnetic vector which is the default initial condition in 'magnetic fields' interface solving for the vector potential  $\vec{A}$ .

$$\vec{A} = \frac{1}{4\pi} \iiint \frac{\vec{J}}{r} dV' = \vec{0} \quad (4.36)$$

The  $r$  in the denominator represents the distance between the volume element  $dV'$  and the point for computing the vector potential.

These were set on the entire domain for both problems.

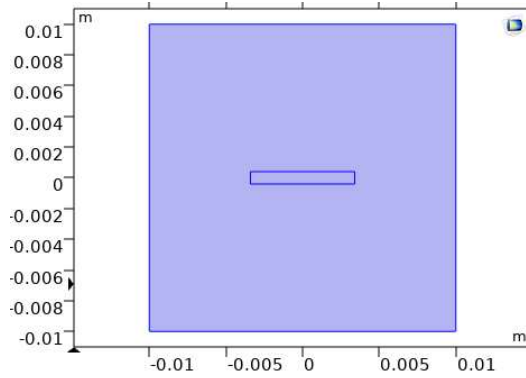


**Figure 4.4:** Initial conditions for magnetic and thermal problem

Concerning the boundary conditions, magnetic and thermal insulation conditions were imposed as it is shown beneath.

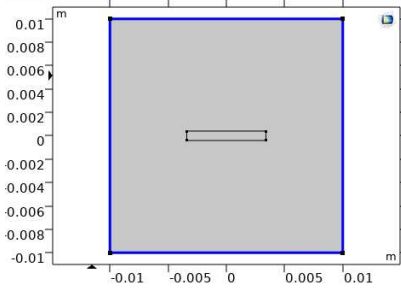


**Figure 4.5:** Magnetic insulation on all nitrogen boundaries

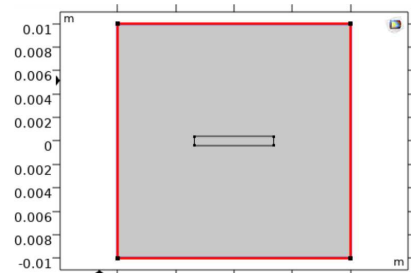


**Figure 4.6:** Thermal insulation on all nitrogen boundaries

## 4.2.2 Copper Tape under AC supply

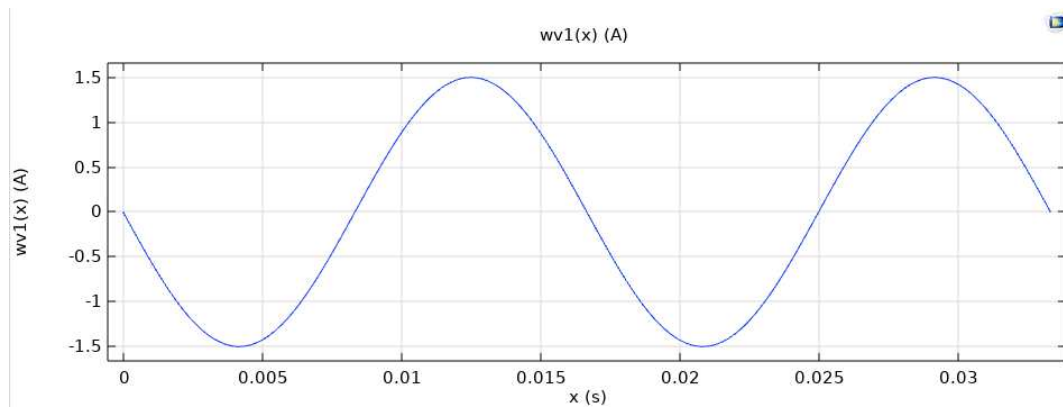
An AC current in the copper tape was imposed, with an amplitude of 1.5 (A) and a frequency of 60 (Hz) with a delay of  $\pi$  in the coil and the simulation is performed.

Due to the quite poor thermal conductivity, very poor electrical conductivity and the large volume of the liquid nitrogen, it is difficult to observe significant effects, particularly in the heat transfer phenomenon.

**Table 4.2:** Thermal and Electrical Conductivity of Liquid Nitrogen at 77 K

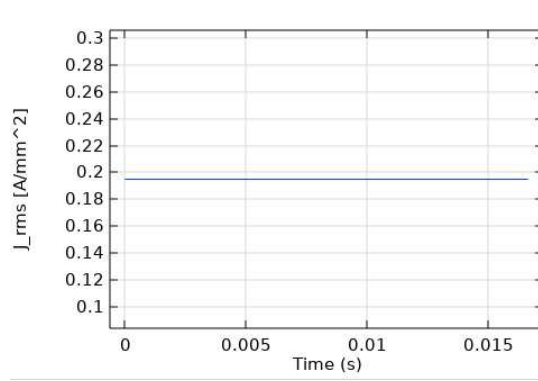
Property	Value
Thermal Conductivity	0.104 W/(m · K)
Electrical Conductivity	$\approx 10^{-14}$ S/m

As a first step, post simulation, the signals  $I(A)$  inside the coil and the  $J_{RMS}$  are plotted.



**Figure 4.7:** Waveform I (A) (input signal)

Considering that the cross section of the copper tape is equal to  $S=5.44 \times 10^{-6} \text{ m}^2$ , it is possible to plot the RMS value of the Current density  $J$  verifying that the current density inside the tape corresponds to the signal input of 1.5 (A) as a peak value:


**Figure 4.8:**  $J_{RMS}$ 

This value is quite far from the physical constraint in ambient temperature of the copper tape which is around 4 (A/mm<sup>2</sup>) and in particular considering that the simulations was performed at 77 (K).

It is evident that imposing a peak current of 1.5 (A) is unlikely to yield significant results. In fact, considering the limitations delineated in the subsequent table, the copper tape can accommodate a peak current approaching 30 (A) at ambient temperature and even higher considering the tape submerged at 77(K).

**Table 4.3:** Limits of  $J_{rms}$  for Copper Tape at Different Temperatures

Temperature (K)	$J_{rms}$ Limit (A/mm <sup>2</sup> )
Room Temperature	4 A/mm <sup>2</sup>
77 K	15-20 A/mm <sup>2</sup>

The Ampere-Maxwell law is used to perform verification at two or more random time instants, confirming that the values of the magnetic field  $\vec{B}$  ensure the simulation operates correctly.

$$\oint_{\partial\Sigma} \mathbf{H} \cdot d\mathbf{l} = \int_{\Sigma} \mathbf{J} \cdot d\mathbf{S} + \frac{d}{dt} \int_{\Sigma} \mathbf{D} \cdot d\mathbf{S} \quad (4.37)$$

Assuming in (4.37) that the electric Field is negligible as well as the polarization, the vector  $\vec{D}$  is not considered, and therefore the term associated to the variation in time of D which causes a magnetic field is considered negligible. In addition, through the Hopkinson laws it is possible to obtain from (4.37) the following equation:

$$\oint \vec{H} \cdot d\vec{l} = \iint \vec{J} \cdot d\vec{S} = N \cdot I \quad (\text{by Hopkinson law}) \quad (4.38)$$

Where  $N$  is the number of the coils and  $I$  is the current passing through the coils. From (4.38), the path along the magnetic field  $\vec{H}$  is computed, is approximated as a circumference, the integral over the surface  $S$  of the copper tape crossed by  $\vec{J}$  is equal to the peck current and the number of turns  $N$  is equal to one. Therefore, it is possible to evaluate the magnetic field  $\vec{B}$  as follows:

$$\vec{B} = 4\pi \times 10^{-7} \left( \frac{\vec{I}}{2\pi r} \right) \quad (4.39)$$

Equation (4.39) is valid for a pontual conductor, however, considering the small dimensions of the tape, as a first verification, this law was used assess the reliability of the results and ensure the electromagnetic phenomena is accurately modelled. Subsequent graphical analysis provides temporal snapshots of the magnetic field  $B(T)$ . For the purposes of this evaluation, two specific time steps were selected:

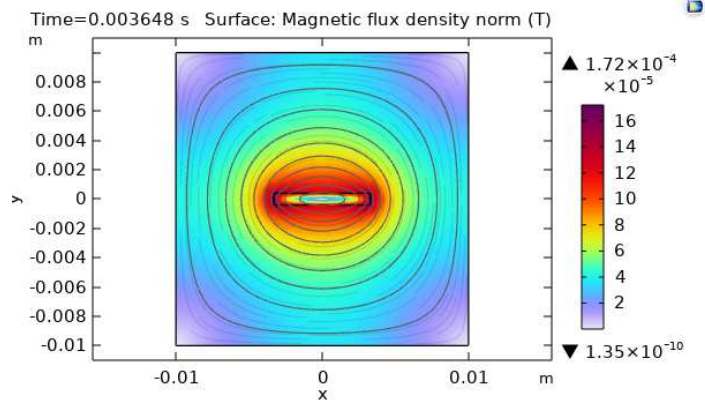


**Figure 4.9:**  $B(T)$  at time step  $t=0,003648(s)$

In the table below it is possible to look at the values useful for computing by the equation (4.39) the magnetic field. The same procedure is performed considering

**Table 4.4:** Comparison of Magnetic Field  $B(T)$  from Software and Computed Values

Time (s)	Radius (m)	Current (A)	$B(T)$ from Software	Computed $B(T)$
0.003648	0.0075367	-1.47	$3.97 \times 10^{-5}$	$3.9 \times 10^{-5}$

the time step  $t=0,01(s)$ :

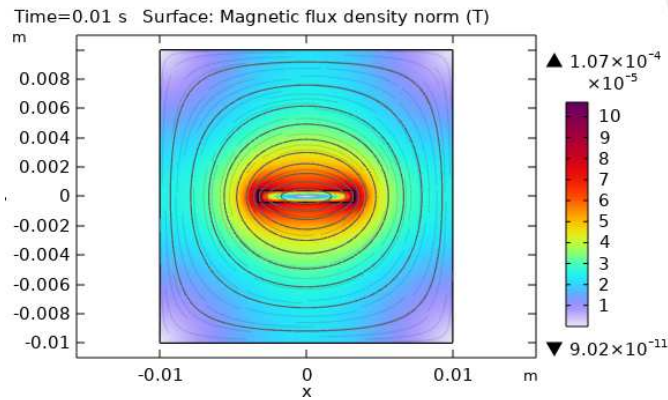


**Figure 4.10:** Magnetic field at  $t=0,01(s)$

**Table 4.5:** Comparison of Magnetic Field  $B(T)$  from Comsol and Computed Values

Time (s)	Radius (m)	Current (A)	$B(T)$ from Comsol	Computed $B(T)$
0.01	0.007596	0.88	$2.3593 \times 10^{-5}$	$2.32 \times 10^{-5}$

Therefore it is possible to assume that the simulation accurately replicates the behavior of the conductor and the electromagnetic behaviour of the system.

### 4.2.3 Electromagnetic heating

The FEM model is implemented considering coupled electromagnetic-thermal model and the increasing temperature corresponds to joule losses of copper since the models are coupled so this thermal heating model just takes the losses from the electromagnetic variables and the information of the surrounding material which is in this simulation the liquid nitrogen.

Here, the equation which represents the phenomenon:

$$\rho c_p \frac{\partial T}{\partial t} + \rho c_p \mathbf{u} \cdot \nabla T = \nabla \cdot (k \nabla T) + Q_e \quad (4.40)$$

As it has been just discussed previously, the content of the equation is briefly summarized:

- $\rho$  represents the density of the fluid.
- $c_p$  is the specific heat at constant pressure.

- $\frac{\partial T}{\partial t}$  is the partial derivative of temperature  $T$  with respect to time  $t$ .
- $\mathbf{u}$  is the velocity vector field of the fluid.
- $\nabla T$  represents the temperature gradient.
- $\nabla \cdot (k \nabla T)$  is the divergence of the thermal conductivity  $k$  times the temperature gradient, which represents the conductive heat transfer.
- $Q_e$  is the external heat source term, which in this case, is the heat coming from Joule losses.

The simulation was implemented imposing a 100(A) DC current applied in the tape for around three hours to obtain an observable result in the analysis since the low thermal conductivity of the liquid nitrogen and the higher volume compared with the volume of the tape may lead to a imperceptible variations in therms of increasing temperature.

Here, the results obtained from the model at  $t=0(s)$  and  $t=3600(s)$ :

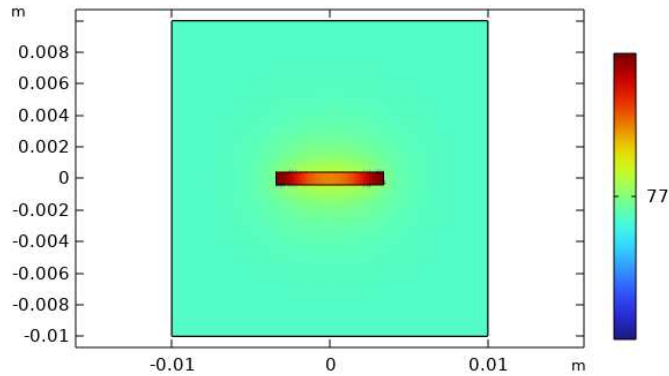
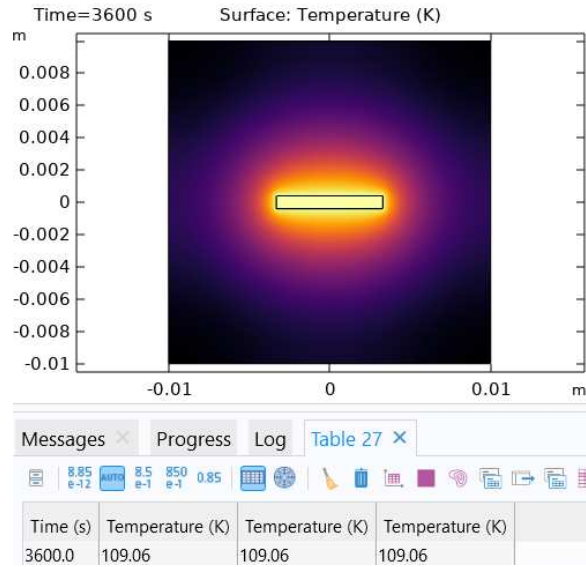
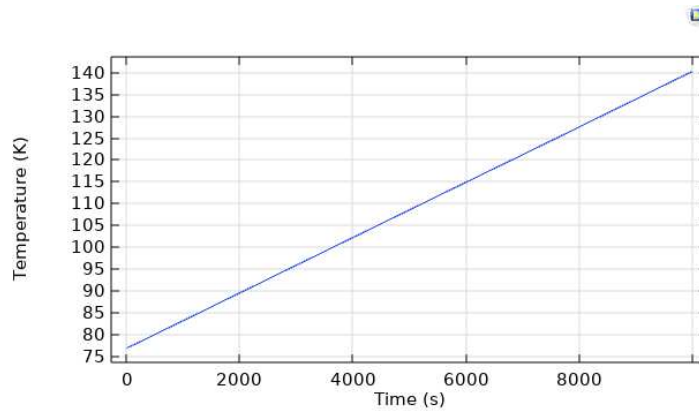


Figure 4.11: Temperature map at  $t=0(s)$



**Figure 4.12:** Temperature map at t=3600(s)

Additionally, the relationship between temperature and time was plotted to get the idea about the mathematical model to use in order to verify the accuracy of the software results.



**Figure 4.13:** Relationship Temperature-time

As it can be observed, it is a linear relationship, therefore from (4.40), it is evident that the heat generated from the copper tape by Joule losses is absorbed by conduction from the liquid nitrogen.

Therefore a verification between the heat balance was performed as follows:

$$\int_0^t RI^2 dt = \rho_{\text{liquid}} V_{\text{liquid}} c_{p,\text{liquid}} \Delta T \quad (4.41)$$

with the following values:

Quantity	Symbol	Value (Unit)
Resistivity of copper tape at 77 K	$\rho_{77K}$	$2.29 \times 10^{-9} \Omega \cdot m$
Current	$I$	100 A
Resistance	$R$	$8.77 \times 10^{-5} \Omega$
Density of liquid nitrogen	$\rho$	$808 \text{ kg/m}^3$
Volume	$V$	$8.286 \times 10^{-5} \text{ m}^3$
Specific heat at constant pressure	$c_p$	$1040 \text{ J/kg/K}$
Change in temperature	$\Delta T$	$42 \text{ K}$

Therefore from (4.41) on the left hand side it is obtain  $Q=3159(\text{J})$  and from the right hand side it is obtained  $Q=3027(\text{J})$  and it could be considered verified since some values are not more precise at low temperatures and may be affected by other phenomena.

This thermal part is implemented in the same way for superconductors or copper, since only the material characteristics change. So thermal model in superconductors is not done because temperature was not measured in the tape but just electrical characteristics.

#### 4.2.4 Copper tape with DC supply (analytical) verification

As a case of study, a copper tape was considered with input current in the simulation.

This input signal was set as the DC current multiplied by the function 'step' which is a smooth step function. The imposed signal can be seen in Fig.4.11. To change the value of the input current the step is multiplied by the DC current amplitude, changing its upper limit.

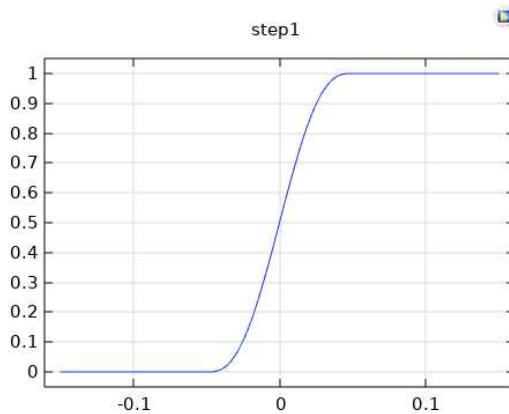


**Figure 4.14:** Time step function

It is important to highlight that starting from this study, the copper simulations

are set in ambient temperature since the resistance is computed at that temperature.

In the laboratory, the dimensions of a copper tape have been measured through the "Vernier Caliper", which are the same used in the previous simulation.

And the following dimensions are obtained:

- a) Length= 21 (cm)
- b) Width= 6,8 (mm)
- c) thickness= 0,8 (mm)

It is crucial to emphasize that this numerical simulation was conducted at room temperature, with the system surrounded by air rather than liquid nitrogen. Furthermore, the simulation employed the 'A-formulation,' as previously discussed in the text.

As input in the coil, different values of DC current are imposed, knowing the analytical value of the resistance computed by the Ohm's law considering the resistivity of the copper tape at room temperature and the dimensions,  $R$  is equal to  $6.7 \times 10^{-4} (\Omega)$ .

Imposing two different values of DC current, namely, 1(A) and 2(A), the following verifications have been made, where in each point the analytical value is computed and compared with the simulation value.

- Check of the voltage.
- Check of the resistance.
- Check of the magnetic field.

Starting from the value of current equal to 1(A), the analytical value of the voltage is  $6.67 \times 10^{-4} (V)$ . Extracting the post-processing values of current from Comsol, this check results to be verified.

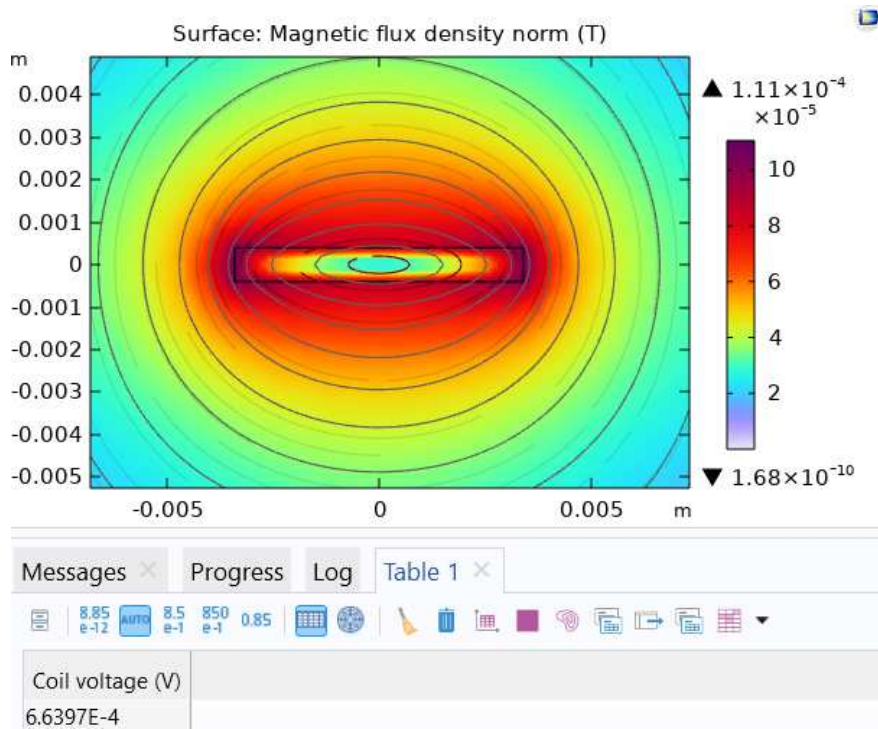


Figure 4.15: Post-process voltage

Concerning the magnetic flux, the analytical values is computed through the same model:

$$\vec{B} = 4\pi \times 10^{-7} \left( \frac{\vec{I}}{2\pi r} \right) = 2.65 \times 10^{-6} \text{ (T)}. \quad (4.42)$$

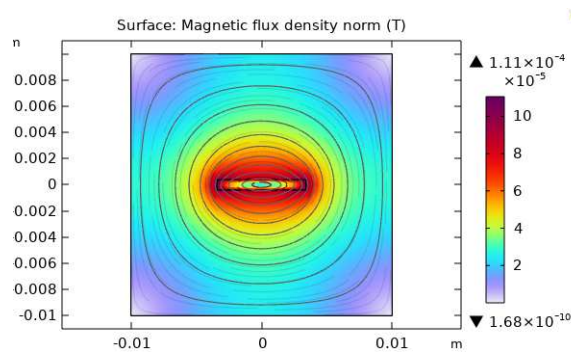


Figure 4.16: Magnetic field at 1 (A)

The magnetic field is inherently constant under DC conditions, and the value obtained from the software is in good agreement with the analytically calculated result.

**Table 4.6:** Comparison of Magnetic Field  $B(T)$  from Comsol and Computed Values

Radius (m)	Current (A)	$B(T)$ from Comsol	Computed $B(T)$
0.07546	1	$2.693 \times 10^{-6}$	$2.65 \times 10^{-6}$

The same is performed for the input DC current of 2 (A) and concerning post-processing current and voltage, the results can be seen below.

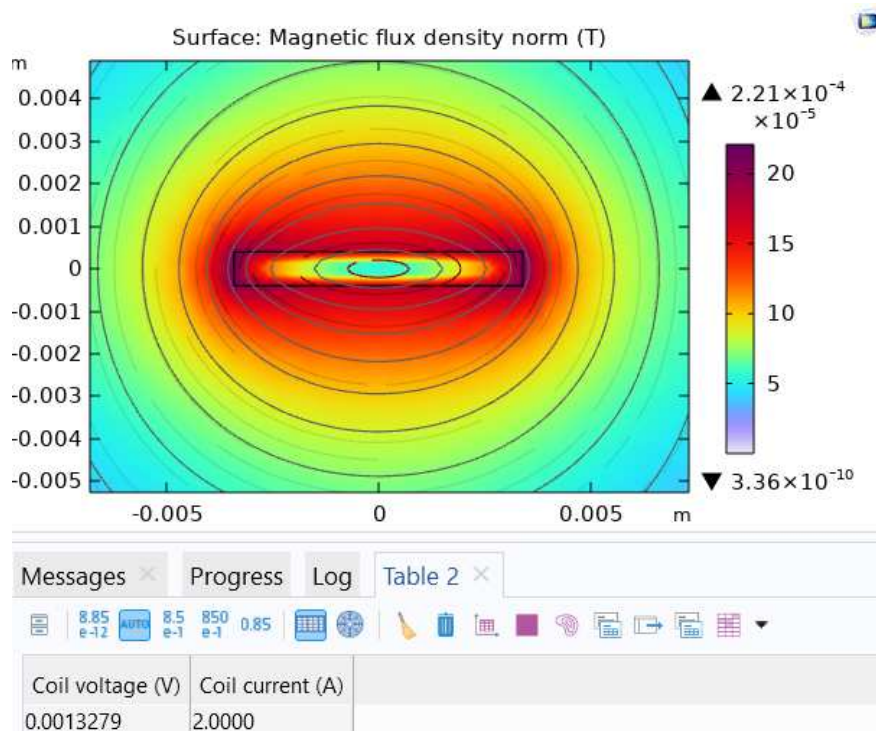


**Figure 4.17:** current and voltage

Concerning the magnetic flux, a value of  $5.288 \times 10^{-6}$  (T) is obtained which very close to the same extracted from the software.

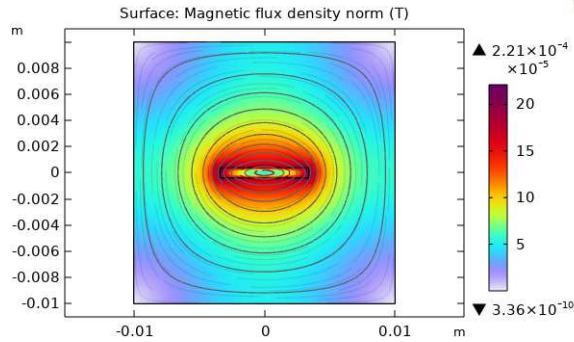


**Figure 4.18:** Magnetic field at 2(A)

**Table 4.7:** Comparison of Magnetic Field  $B(T)$  from Comsol and Computed Values

Radius (m)	Current (A)	$B(T)$ from Comsol	Computed $B(T)$
0.075768	2	$5.372 \times 10^{-6}$	$5.288 \times 10^{-6}$

#### 4.2.5 Comparison between experimental data obtained from a copper tape powered by AC current and data obtained from the software

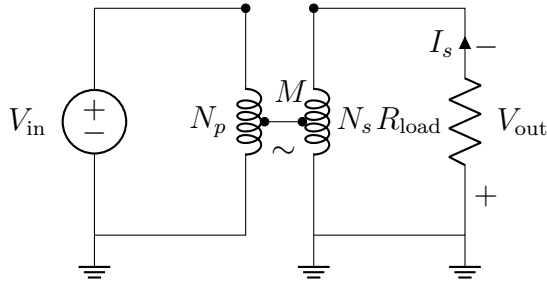
As a experimental analysis, it has been performed on the same copper tape in AC regime.

A sinusoidal wave with a frequency of 50 (Hz) with variable amplitude has been imposed as the tape's current.

In the built circuit, like a transformer, the wave imposed in the primary, through the number of turns, increased in therms of amplitude, considering the following relationship:

$$I_p \times N_p = I_s \times N_s \quad (4.43)$$

where subscript  $p$  and  $s$  indicate the primary and secondary, and  $N$  is the number of turns.



The values of peak current ( $I_s$ ) and voltage ( $V_s$ ) measured at the secondary, keeping the frequency constant and equal to 50 (HZ), where the load (copper tape) is connected, are reported in the following table:

**Table 4.8:** Measured peak values of Current and Voltage at the Secondary with Load

$I_s$ (A)	$V_s$ (mV)
3.988	11.674
10.24	29.84
16.26	48.21

As a first step, a current waveform has been imposed in the coil in COMSOL, with the amplitude as the measured value in order to verify whether the simulation results replicate the experimental values.

It is important to compare the behavior of the experimental result in terms of voltage with the ones coming from the software, considering the values listed above.

Considering the first signal with a secondary peak current of 3.988 (A), in the picture below it is possible to observe the post-processing signal of the voltage, obtained with a surface integral over the copper divided by the constant tape cross-section for each time step.

The choice to derive the voltage value through integration is purely a decision; this value could have also been obtained through other methods or 'paths'.

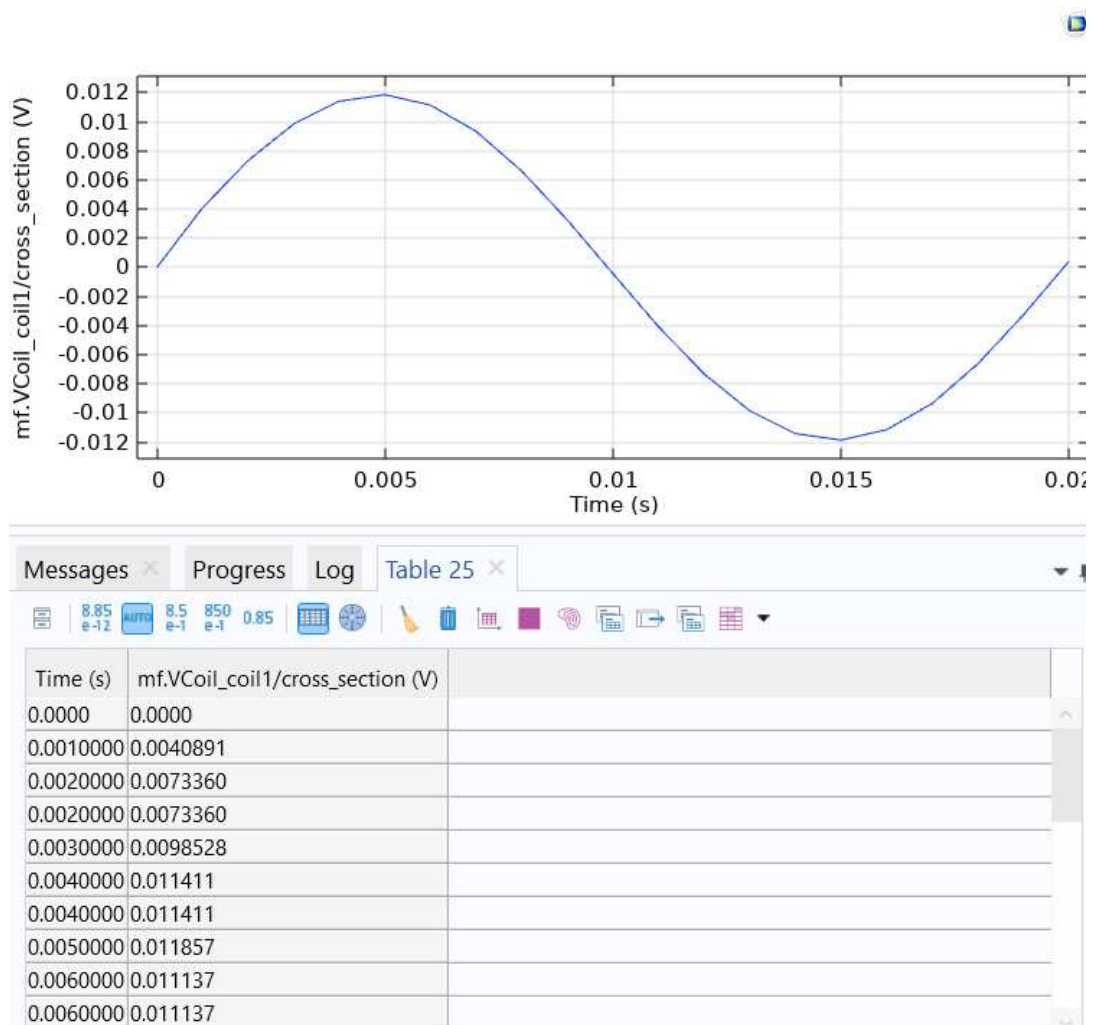


**Figure 4.19:** Voltage signal post-processing at 3.988(A)

Therefore, for the first set of data, the model seems to replicate well the real behavior of the experiment.

The same process is repeated again for the peak currents of 10,24(A) and 16,26(A).

In the subsequent figure, one can observe a notable degree of concordance between the experimental data and the results generated through simulation.

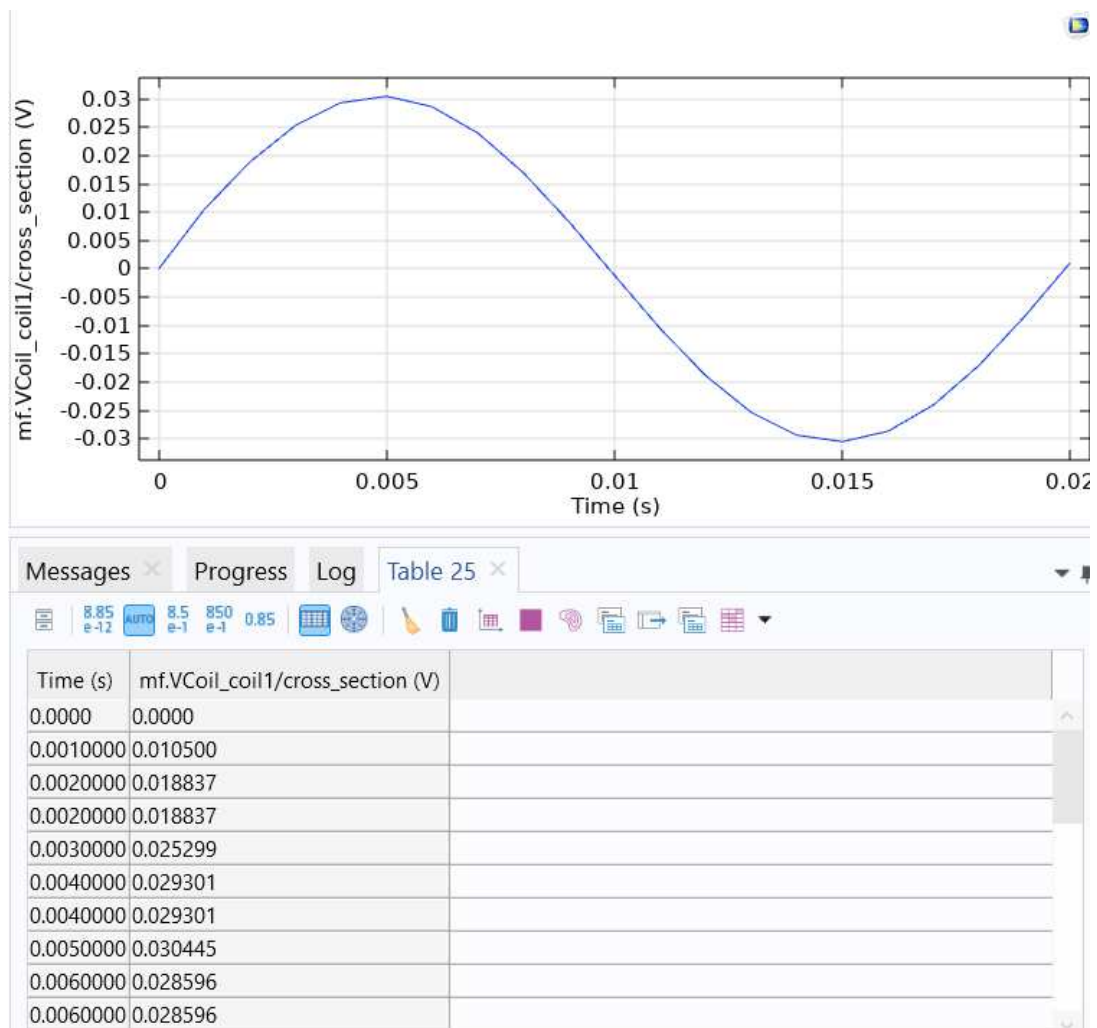


Figure 4.20: Voltage signal post-processing at 10(A)

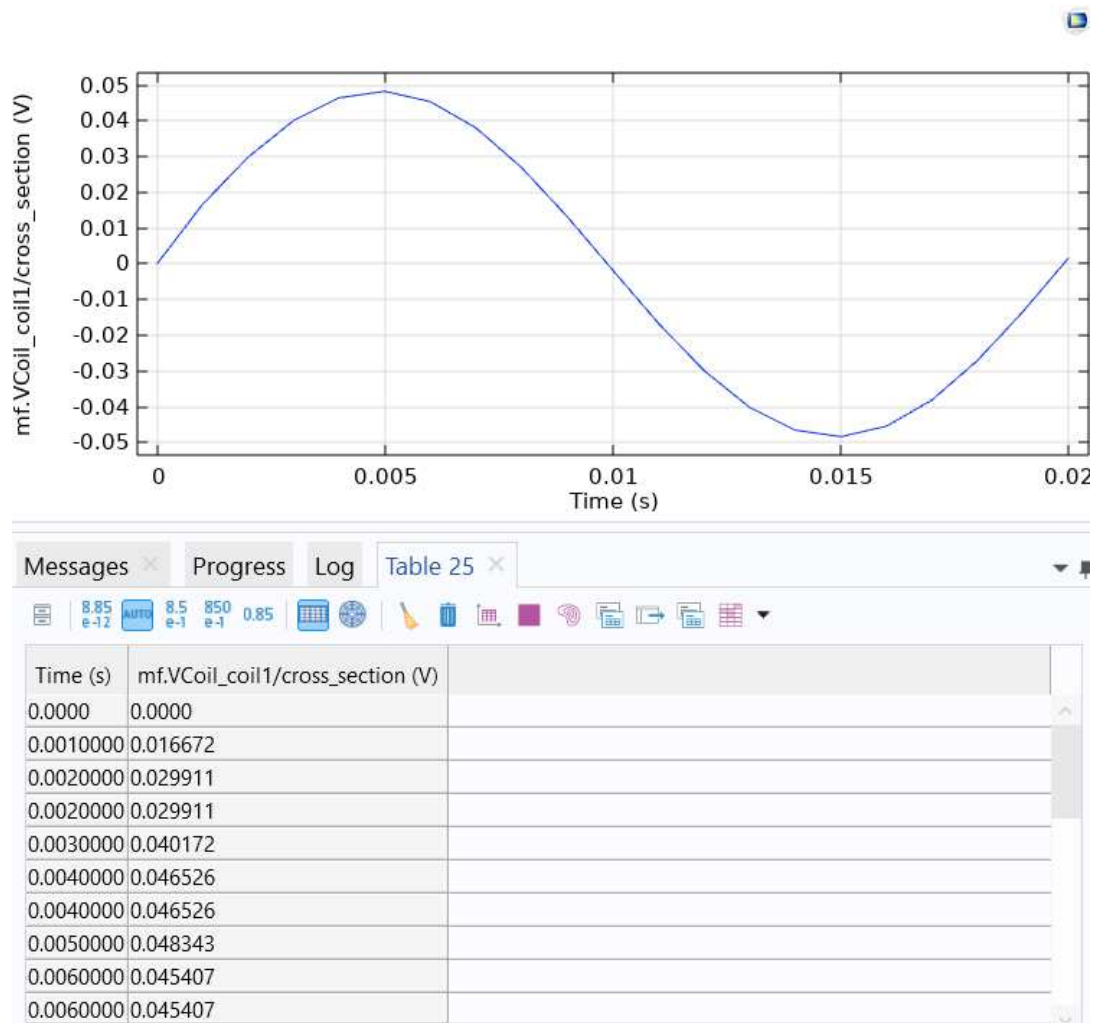


Figure 4.21: Voltage signal post-processing at 16(A)

Observing the result obtained, the experimental data result to be well reproduced, therefore, the case study copper tape model is validated.

## 4.3 Electromagnetic simulations in superconductors with different formulations

### 4.3.1 A-formulation

The A formulation has been implemented in order to solve from numerical methods the parameters which are interesting such as  $J$ ,  $E$  and  $\rho$ .

The name of this formulation is given by the state variable, the vector potential  $\vec{A}$ . The equations used in this formulation are the following ones:

$$\nabla \times \frac{1}{\mu_0} \nabla \times \vec{A} = \vec{J} \quad (4.44)$$

$$\vec{B} = \nabla \times \vec{A} \quad (4.45)$$

$$\nabla \cdot \vec{B} = 0 \quad (4.46)$$

The numerical simulation approach employed here is consistent with previous methodologies, as it also involves solving for the magnetic vector potential  $\vec{A}$ . The distinguishing feature in this case is the incorporation of the resistivity power law in the superconducting domain as it is shown in (4.46), which exhibits strong non-linearity during the transition from superconducting to normal conducting behavior. This deviates from Ohm's law, which posits a linear theoretical relationship between voltage and current.

The computational framework initially focuses on the determination of  $\vec{A}$ , from which  $\vec{E}$  is subsequently derived.

$$E = E_0 \left( \frac{J}{J_c} \right)^n$$

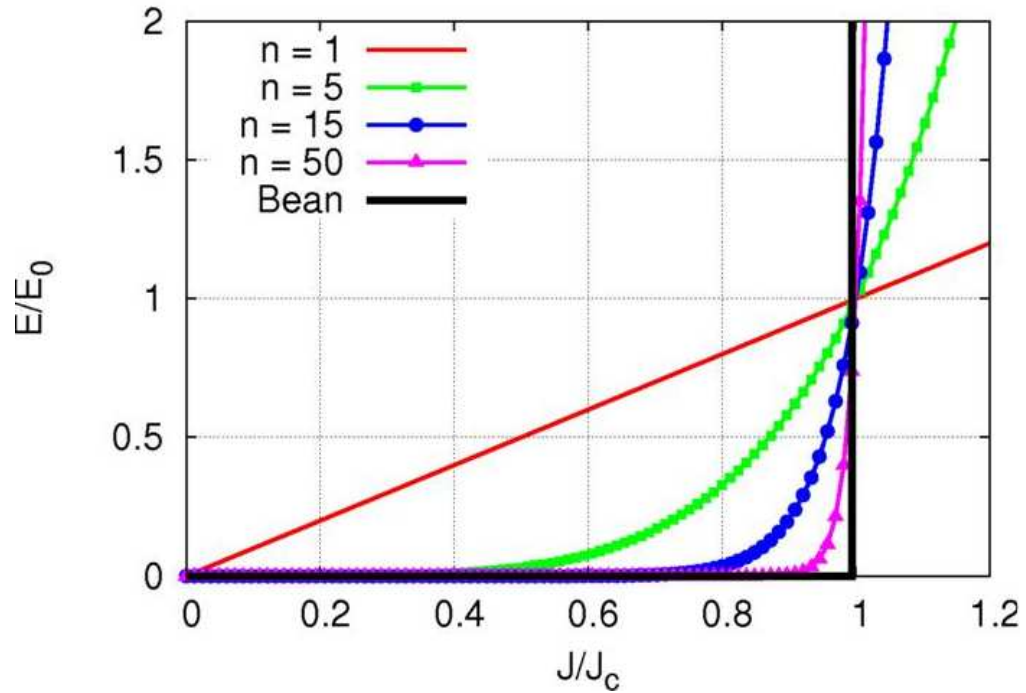


**Figure 4.22:** Power law for different values of the exponential constant 'n'[17]

Here, it is possible to observe that the  $n$  value is a parameter defining the steepness of the power law, and therefore that defines how fast the transition to the resistive state occurs.

## 4.4 Experimental analysis and comparison between data

### 4.4.1 Superconducting simulation in DC regime

Starting from the software configuration, the geometry has been built considering the real dimensions of the HTS tape surrounded by air.

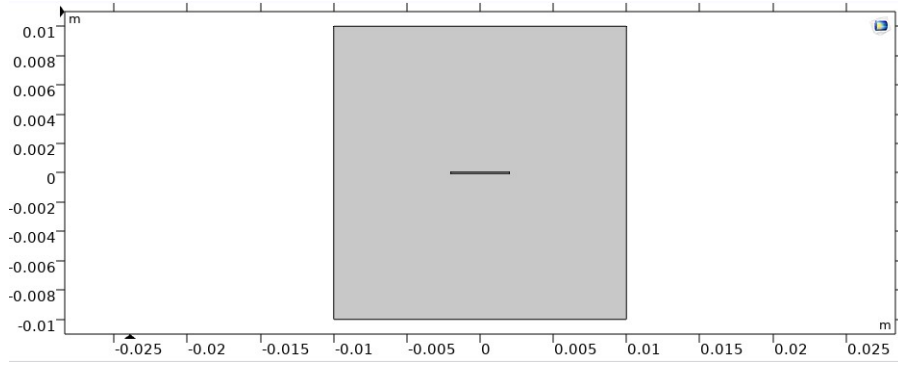


**Figure 4.23:** Geometry on the software

The analytical expressions of the model have been imposed on the software.

$$J_{\text{critical}} = \frac{J_{c0} \cdot B_0}{B + B_0} \quad (4.47)$$

It is interesting to look at the equation of  $J_{\text{critical}}$ , If the magnetic field  $\vec{B}$  increases, which is the sum of the external magnetic field and the internal one ( or the self-field), the critical current decreases following the Kim model.

$$\rho = E_0 \left( \frac{J_z}{J_{\text{critical}}} \right)^{n-1} \frac{1}{J_{\text{critical}}} \quad (4.48)$$

And the following starting parameters are imposed with typical values:

Parameter	Value	Description
Si	$3.824 \times 10^{-7} \text{ m}^2$	cross section
E0	$1 \times 10^{-4} \text{ V/m}$	critical Electric field
Ic0	160 A	current
n	14	exponential constant
B0	100 mT	critical magnetic field

**Table 4.9:** Superconductor parameters

This simulation is performed using the A formulation and forcing the coil with a DC current which increase from 0 to 200 (A) imposing a step function with applied current as maximum value.

The behavior of the magnetic field for two different input currents are shown beneath, in particular for 40(A) which corresponds to a superconducting state and for 160(A) which should be around the value of critical current, which is, by definition, the peak current that a specific superconductor can sustain before

transitioning to its resistive state.

Specifically, the transition from a superconducting state to a resistive state is referred to as the superconductor undergoing a quench.

Here, the software-generated image the magnetic field characteristics corresponding to a given input current.

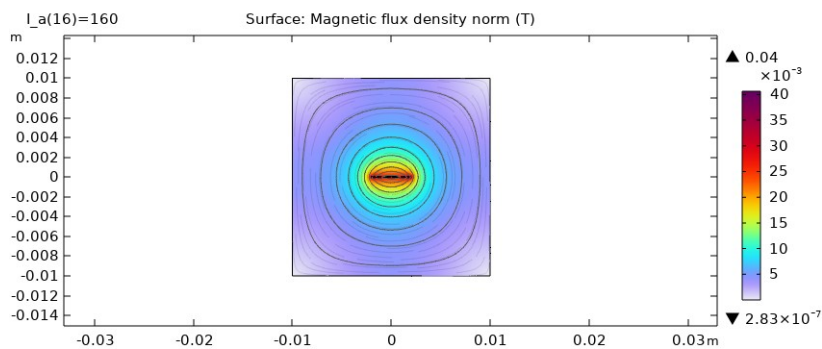


Figure 4.24: Magnetic field at 160 (A)

#### 4.4.2 Collection of the data and laboratory experience

The apparatus designed for handling superconductors is highly sensitive, necessitating meticulous attention to multiple potential complications. Foremost, the superconductor material itself exhibits pronounced sensitivity. Proper handling is imperative to prevent potential ruptures, short circuits, or open circuits that could compromise the desired outcomes.

It is necessary to manage the liquid nitrogen in order to keep the superconductor in its state.

The tape is submerged in liquid nitrogen, allowing to keep the temperature below its critical point, therefore the temperature has to be kept below 90(K).

In the subsequent figures, the laboratory configuration employed for experimental data collection is shown.



**Figure 4.25:** Superconducting tape setup surrounded by liquid nitrogen and insulator



**Figure 4.26:** Superconducting tape setup surrounded by liquid nitrogen and insulator

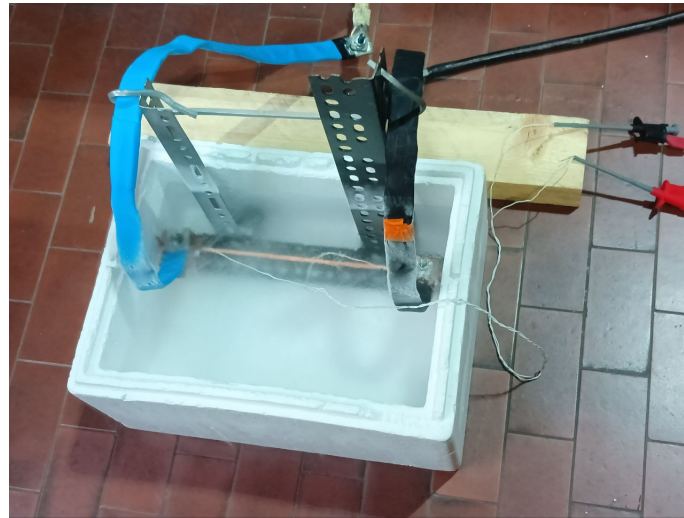


**Figure 4.27:** Superconducting tape while liquid nitrogen is boiling

In the image above, it is evident the boiling of liquid nitrogen due to the ambient temperature and it is amplified by the heating of the tape while the current is passing through.



**Figure 4.28:** Data collection

### **4.4.3 Experimental method**

During the data collection, different values of DC current were imposed in the superconducting tape, measuring and recording the values of voltage.

It was very interesting observing the transition from the superconducting state in which, increasing the current, the voltage kept almost negligibly low.

At a certain time, the voltage as well as the Electric field, started increasing following a strong non linear path, as the macroscopic mathematical model describes, approaching the critical current value, which is quite evident to observe in the data and in the plots.

**Table 4.10:** First set of experimental data

$I(A)$	$V(mV)$ DC $\pm$ 0.001	$E(V/m)$
5	0	0
35	0	0
60	0	0
70	0	0
80	0.001	$4.7619 \times 10^{-6}$
100	0.001	$4.7619 \times 10^{-6}$
110	0.003	$1.42857 \times 10^{-5}$
120	0.004	$1.90476 \times 10^{-5}$
125	0.005	$2.38095 \times 10^{-5}$
125.91	0.007	$3.33333 \times 10^{-5}$
128.89	0.01	$4.7619 \times 10^{-5}$
129.89	0.013	$6.19048 \times 10^{-5}$
130.89	0.0155	$7.38095 \times 10^{-5}$
131.885	0.017	$8.09524 \times 10^{-5}$
132.89	0.0185	$8.80952 \times 10^{-5}$
134.878	0.022	0.000104762
135.86	0.0244	0.00011619
136.87	0.029	0.000138095
140.85	0.042	0.0002
142.85	0.052	0.000247619
145.84	0.0695	0.000330952
146.84	0.0745	0.000354762
148.83	0.087	0.000414286
150.9	0.099	0.000471429
153.98	0.127	0.000604762
155.99	0.148	0.000704762
156.98	0.161	0.000766667
158.96	0.189	0.0009
160.96	0.22	0.001047619
163.985	0.279	0.001328571
165.965	0.327	0.001557143
167.98	0.38	0.001809524
168.96	0.415	0.00197619
170.94	0.48	0.002285714
173.93	0.65	0.003095238
175.94	0.78	0.003714286
178.95	1.03	0.004904762
179.94	1.17	0.005571429

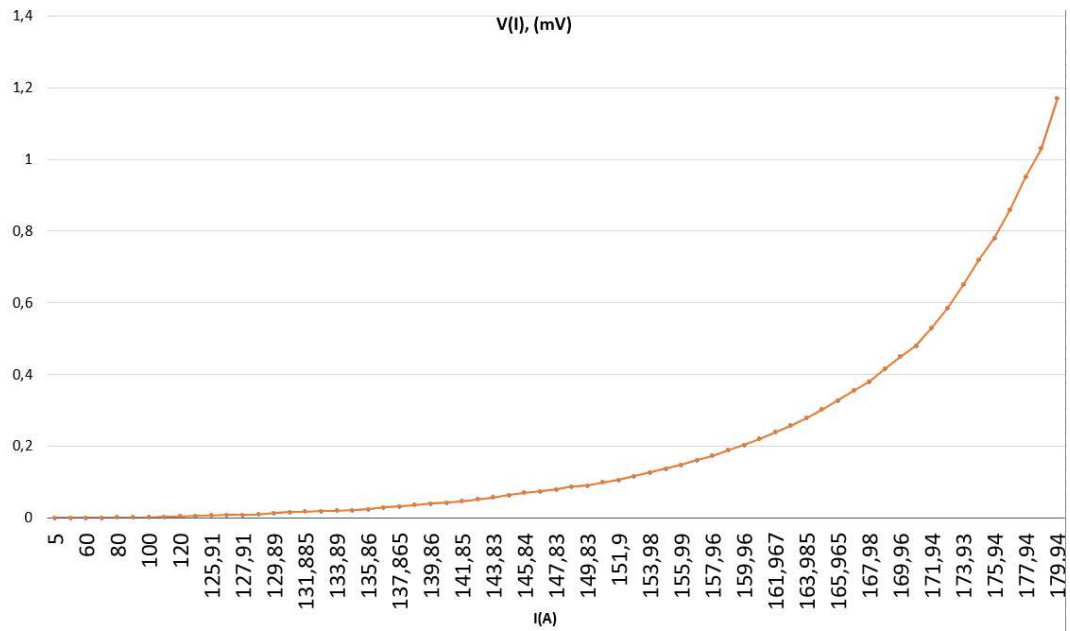


Figure 4.29: Voltage as a function of the current

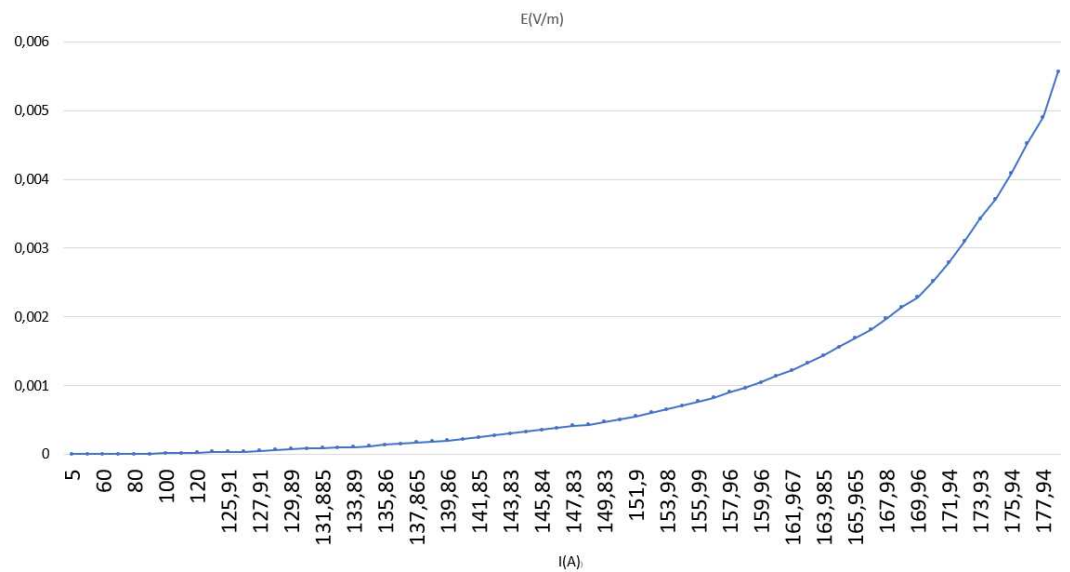


Figure 4.30: E-J experimental curve

#### 4.4.4 Experimental results

The objective of this study is to closely emulate experimental results through numerical modelling, and subsequently, assuring their reliability.

Additionally, the study aims to evaluate the adaptability of this data to computational analysis, given the inherent complexity and non-linearity of the observed phenomenon. Initial laboratory data delineates the voltage behavior relative to the current and the E-J curve, underscoring pronounced non-linearity.

As a first step, in order to get a comparison between experimental and computed data, a parametric sweep, which enables a parameter to vary across a spectrum of values and is feasible during transient, AC, or DC sweep examinations, has been implemented, in order to verify the possible match between the data, starting with typical parameters of  $I_{c0}=160$  (A),  $n=14$  and  $B_0=0.1$ (T) [18], performing a matlab study with the 'fitting curve toolbox' which aims to find the best matching between experimental data and simulated data obtained by the software Comsol. The swept parameter was imposed to be the DC current and in the picture beneath are shown the final fitted curve in comparison:

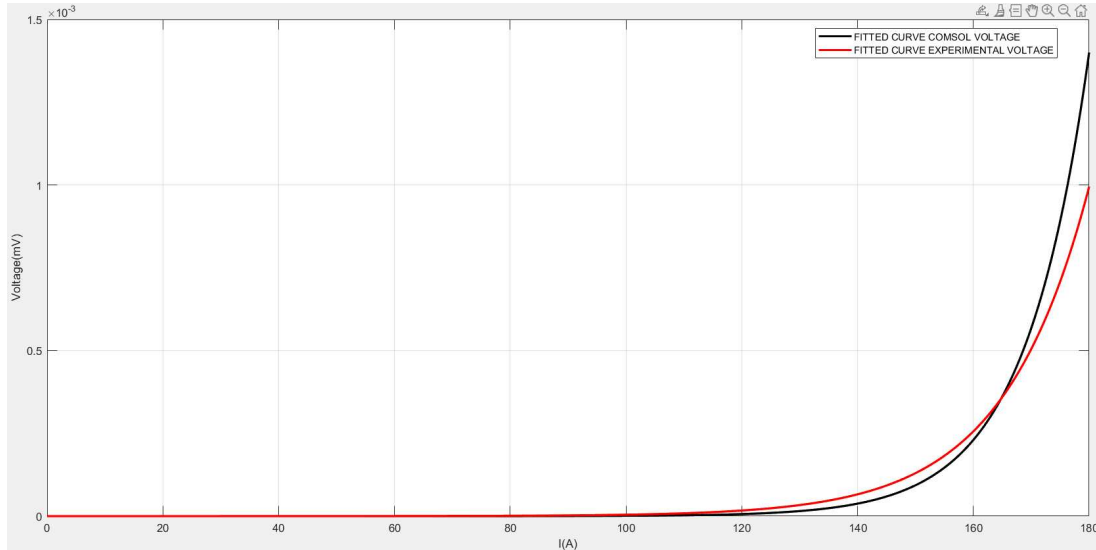


**Figure 4.31:** Fitted experimental and computed voltage

The behavior seems to be quite similar, but in order to obtain the best possible results, the model should be optimized with respect to the variables  $I_{c0}, n$  and  $B_0$ , keeping in mind the fact that from equation (5.14) the value of electric field at the critical current should be close to  $E_0$ .

These parameters are important for modelling since:

1.  $I_{c0}$  (**Critical Current Density**): This parameter serves for describing the maximum current density a superconductor can sustain without going outside

its superconducting state. For applications such as electromagnets or power transmission lines, an accurate estimation of  $I_{c0}$  is indispensable for ensuring operational safety and efficiency.

2.  $n$  (**Exponent**): The exponent  $n$  dictates the sensitivity of the electric field  $E$  to variations in the current density  $J$ . A high value of  $n$  implies a rapid increase in the electric field as  $J$  approaches  $J_c$ , having ramifications for the stability and control of superconducting devices.
3.  $B_0$  (**Characteristic Magnetic Field**): The model incorporates the effects of magnetic fields,  $B_0$  serves as a scaling factor for how  $J_c$  varies with  $B$ .
4.  $E_0$ : This parameter sets the scale for the electric field. It ensures that the modeled electric field aligns with empirical observations, particularly at the critical current. It is a conventional value and it was considered fixed.

Here, the importance concerning the fitting:

1. **Optimization**: During the fitting process, these parameters act as adjustable "knobs" that are optimized to align the model closely with experimental data. Their optimized values offer an accurate description of the physical system under investigation.
2. **Error Minimization**: Precise parameter values are crucial for minimizing the discrepancy between the model and observed data, thereby enhancing the model's predictive accuracy.
3. **Physical Interpretation**: Post-optimization, the parameters can be analyzed to yield valuable insights into the material's physical properties. Deviations from theoretical expectations could indicate novel physics at play.
4. **Validation and Comparison**: A well-optimized model provides a robust framework for comparing different superconductors or experimental setups. It also facilitates the validation of the model against new or diverse data sets.

Therefore, some matlab optimization algorithm have been implemented in order to get the best possible results, and it will be discussed in detail in this chapter.

As a first implemented code, the aim was to use an optimization algorithm in order to get the best values of  $I_{c0}$ ,  $B_0$  and  $n$  which minimize the objective function which has been set as the mean square error between the electric field computed by Comsol and the Electric field obtained from the experimental results.

Since both the measurements both the software could lead to errors it is important to understand which is the real behavior of the superconductor and through the

comparison between the model and the data it is possible to make considerations about that.

As a matter of fact, this first simple algorithm has the purpose of matching the two E-J curves as well as possible, therefore, it is possible to watch at the schematic of the implemented code and the explanation as follows.

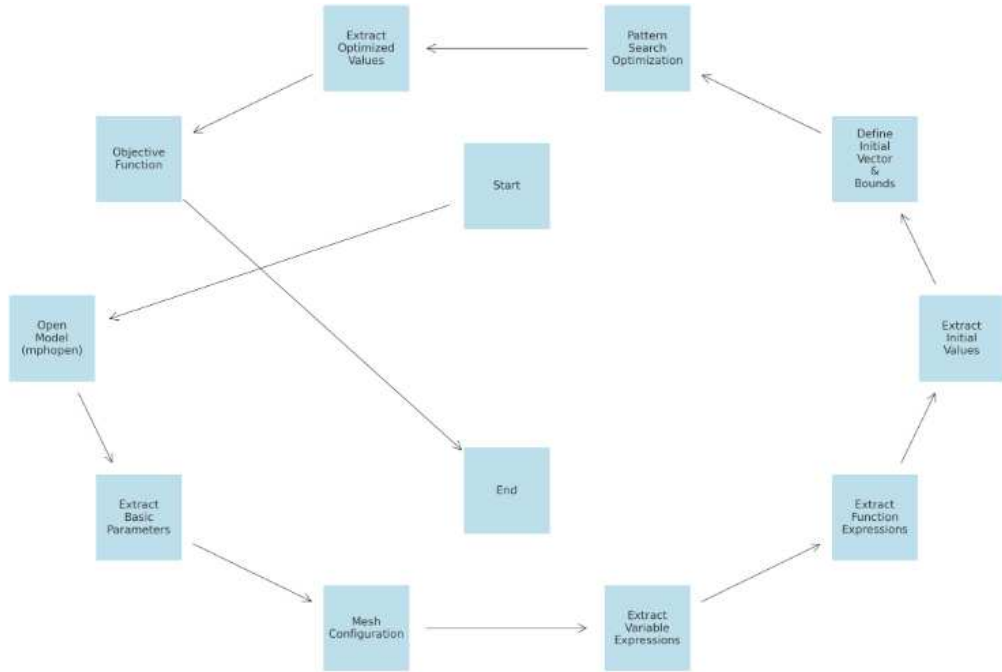


**Figure 4.32:** Iterative flow chart for the first code

As it was anticipated before, the expression imposed in the model for  $J_{critical}$  (5.13),  $\rho$  (5.14) and  $\sigma$  (5.15) are fundamental.

The software Comsol solves for  $\vec{A}$  according with A-formulation and the Matlab code iteratively check if  $\vec{E}$  matches with the experimental one.

After that, the initial values of the the variables to optimize in order to get the best fitting between the experimental and computed data has been set. The optimization algorithm requires the lower and upper boundaries of the three variables in order to follow the path within them, and reasonable values have been imposed.

As a optimization algorithm, the patternsearch has been used to minimize the objective function which in this case is the mean square error.

This is a direct optimization algorithm, therefore, it does not require the computation of the gradient, and it could be great enough in case of Objective functions which are discontinuous or non differentiable, but it could be even slowly in terms of computational time in order to reach the convergence.

The basic idea behind pattern search methods is to explore the search space by evaluating the objective function at a set of points that form a pattern. These points are generated around the current best-known point, and the objective function is evaluated at each of these points.[19] And the procedure is the following one:

- **Initialization:** Choose an initial point  $x_0$  and an initial mesh size  $\Delta$ . The mesh size controls the distance between points in the pattern.
- **Exploratory Move:** Generate a set of points around  $x_0$  according to the pattern and mesh size. Evaluate the objective function  $f(x)$  at these points.
- **Pattern Move:** If an improved point is found, move to that point and go back to Step 2. If no improved point is found, then reduce the mesh size.
- **Stopping Criteria:** Continue this process until a stopping criterion is met, such as a maximum number of iterations, a sufficiently small mesh size, or a sufficiently small change in the objective function value.

In the context of patternsearch, the term "mesh" refers to the set of points where the objective function will be evaluated. The "poll" is the actual set of evaluations of the objective function at the mesh points. A successful poll occurs when any of the mesh points yield a better objective function value than the current point.

It works with an adaptive mesh or refinement,since if a poll is successful, the mesh can expand, allowing the algorithm to take larger steps. Conversely, if a poll is unsuccessful, the mesh contracts, forcing the algorithm to explore more carefully.

Finally, in order to get a complete overview on the optimization algorithm, it is important to highlight that it is possible to add a variety of constraints, including linear, nonlinear, equality, and inequality constraints, and this is really important for many applications.

It can handle even multi-objective functions in the optimization.

Unfortunately, it can be computationally expensive because it requires multiple evaluations of the objective function at each iteration, and for complex problems like the non-linear power law of resistivity it could be a wrong choice.

Additionally, It is worth noting that 'patternsearch' is a local optimization method, which means that it may find a local minimum rather than the global minimum. Starting from different initial points can provide different results.

The vector of optimized variables at each iteration is initialized. After that, the function which is called inside the the optimization algorithm at each iteration is set, with the starting values of n, B0 and Ic0. At each iteration of the optimization algorithm the new parameters have to be set in the comsol model.

Therefore, the empty vector  $E_{\text{COMSOL}}$  which is the vector that should be optimized and fitted with the vector of experimental data of the electric field thanks to the optimization algorithm has been set.

A loop inside the previous loop(patternsearch), which fills the vector  $E_{\text{comsol}}$ , running the study 2 from comsol for each value of the experimental current gave as input, has been set and this one change the values at each iteration of the outer loop since, n,B0,and Ic0 will change.

Inside the optimization iterative algorithm, an interpolation of the calculated and the experimental data has been imposed since comparing two vectors it is not so easy at first glance, therefore it could be better obtaining continuous functions to observe, since looking at two almost-overlapped functions instead of comparing point by point, could allow for quicker validation of the study.

The logarithm is applied to the two vectors containing the values of electric field coming from experimental and simulated results, adding a small value 'eps', which is an infinitesimal quantity summed at each element of the two vectors, avoiding error in case of values equal to zero, due to the domain of the logarithmic function which does not allow values equal to zero. The interpolation 'spline' is performed, which is quite typical in order to get from discrete functions, continuous functions.

In particular,a spline is a piecewise polynomial function that is smooth at the points where the polynomial pieces meet, also known as knots. In cubic spline interpolation, each piece between adjacent knots is a cubic polynomial, mathematically represented as[20]:

$$S(x) = a_i + b_i(x - x_i) + c_i(x - x_i)^2 + d_i(x - x_i)^3 \quad (4.49)$$

where  $a_i$ ,  $b_i$ ,  $c_i$ , and  $d_i$  are coefficients that need to be determined, and  $x_i$  and  $x_{i+1}$  are adjacent knots.

The concept of a "piecewise polynomial" is fundamental to splines. This means that we define a different polynomial equation for each sub-interval between the knots. However, the polynomial pieces must meet certain conditions to form a smooth curve. In cubic spline interpolation, we require that:

- **The function is continuous.**
- **The first derivative is continuous.**
- **The second derivative is continuous.**

Therefore, the working method is briefly explained:

- **Step 1: Initialize and Sort Data Points**  
You start with a set of  $n + 1$  data points  $(x_0, y_0), (x_1, y_1), \dots, (x_n, y_n)$ . These points should be sorted in ascending order based on the  $x$ -values.
- **Step 2: Formulate the Cubic Polynomials**  
For each interval between  $x_i$  and  $x_{i+1}$ , a cubic polynomial is formulated. These polynomials are then pieced together to form the spline.
- **Step 3: Ensure Smoothness**  
To make the spline smooth, we set the conditions for the polynomials to be continuous and have continuous first and second derivatives at the knots.
- **Step 4: Solve for Coefficients**  
A system of equations is formed based on the above conditions, and it is solved to find the coefficients  $a_i, b_i, c_i,$  and  $d_i$  for each cubic polynomial piece.
- **Step 5: Evaluate the Spline**  
Once the coefficients are known, the spline can be evaluated at any point within the range of the data.

At the end, the mean square error is computed and even the plot at each iteration of the interpolated curves as well as the current values of  $n, B_0,$  and  $I_{c0}$  is required from the code.

In the picture beneath it is possible to observe, at the convergence of the algorithm, the two E-J curves and the optimal values of the variables obtained.

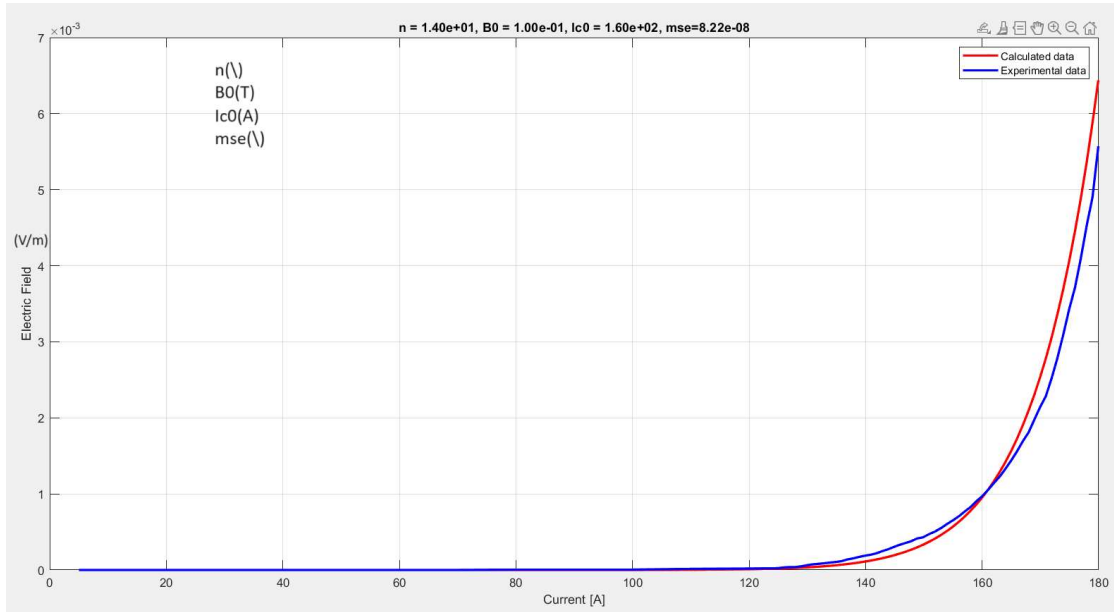


**Figure 4.33:** Result of the convergence of the algorithm considering the first set of experimental data.

**Table 4.11:** Optimal values of the variables in order to minimize the MSE

n	B0(T)	Ic0(A)	mse
14	0.1	160	8.22e-8

The red curve is the one related to the values coming from the simulation and the blue curve is related to the experimental data.

How it is possible to notice above, the simple algorithm well replicates the data, obtaining the the fundamental parameters  $n=14$ ,  $B_0=0.1(\text{T})$  and  $I_{c0}=160 (\text{A})$ .

However, according with the initial assumption, the critical electric field  $E_0$  should be equal to

$$1 \times 10^{-4} \text{ V/m}$$

This come from the equation of the power law:

$$E = E_0 \left( \frac{J}{J_c} \right)^n \quad (4.50)$$

But from the plot, at the resulting critical current, the electric field does not correspond to the defined  $E_0$ , it is possible to observe that there is one order of

magnitude of difference, indeed, the correct value of critical current is around 130(A) as it is evident from the previous plots.

According with the starting assumption, the matlab code converges at the best fitting between experimental and simulated data even though the value of critical current is wrong due to the constraints imposed in a reasonable range of the three variables to optimize but since the range was set not large enough in terms of critical current values, the algorithm converges at its optimal value which is different from the expected one coming from experimental data showing that this method is not suitable to determine the tape's parameters.

#### **4.4.5 Second set of data**

A second set of experimental have been measured and they are reported beneath:

**Table 4.12:** Second set of experimental data

$I(A)$	$V(mV)$ DC $\pm$ 0.001	$E(V/m)$
9.9875	0	0
10.0037	0	0
20.0035	0	0
49.9555	0	0
49.9615	0	0
69.9538	0	0
89.937	0	0
109.876	0.001	$4.25532 \times 10^{-6}$
109.894	0.001	$4.25532 \times 10^{-6}$
114.859	0.001	$4.25532 \times 10^{-6}$
119.838	0.0015	$6.38298 \times 10^{-6}$
119.84	0.001	$4.25532 \times 10^{-6}$
124.821	0.001	$4.25532 \times 10^{-6}$
129.802	0.001	$4.25532 \times 10^{-6}$
134.806	0.001	$4.25532 \times 10^{-6}$
139.768	0.0015	$6.38298 \times 10^{-6}$
139.807	0.001	$4.25532 \times 10^{-6}$
144.76	0.002	$8.51064 \times 10^{-6}$
145.804	0.002	$8.51064 \times 10^{-6}$
146.8	0.002	$8.51064 \times 10^{-6}$
149.802	0.0035	$1.48936 \times 10^{-5}$
149.807	0.003	$1.2766 \times 10^{-5}$
154.95	0.0075	$3.19149 \times 10^{-5}$
154.978	0.007	$2.97872 \times 10^{-5}$
156.946	0.01	$4.25532 \times 10^{-5}$
156.984	0.01	$4.25532 \times 10^{-5}$
159.98	0.0175	$7.44681 \times 10^{-5}$
159.987	0.017	$7.23404 \times 10^{-5}$
163.005	0.029	0.000123404
163.012	0.029	0.000123404
165.02	0.041	0.000174468
166.016	0.0495	0.000210638
167.03	0.059	0.000251064
168.023	0.071	0.000302128
169.018	0.082	0.000348936
170.01	0.098	0.000417021

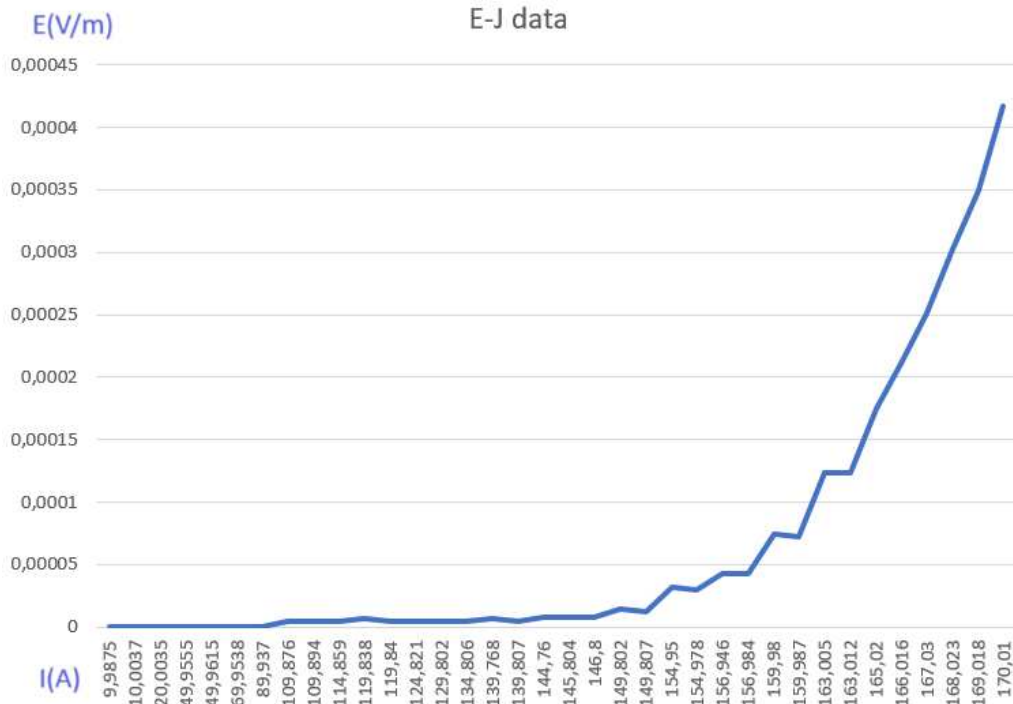


Figure 4.34: Plot of the second set of data (E-J curve)

It is clear that there are not enough data therefore the curve is not smooth, and in the next algorithms developed it has been necessary to implement the number of data through the extrapolation method in order to obtain more accurate results, but the choice to perform the extrapolation has advantages and disadvantages as it will be discussed briefly here. In the next steps of the own work, it will be more clear.

In the context of optimization without extrapolation, each iterative step is influenced solely by local information in the immediate vicinity of the current point within the solution space. Specifically, 'local information' refers to the characteristics of the objective function or constraints that are directly adjacent to the current point. This is commonly quantified using the gradient or another differential measure that captures local variations. Consequently, the algorithm's next move is determined by this localized data, often in the direction of steepest descent or ascent, depending on whether the optimization goal is minimization or maximization.

In contrast, when optimization is performed with extrapolation, the algorithm employs a strategy to jump to distant points in the solution space based on the current and past information.

The idea is to accelerate the search by making fine enough guesses about where good solutions might lie, far from the current point.

This can cause large jumps in the solution space, therefore there is the risk of overshooting, in addition, often this involve more complex calculations or heuristics methods to decide where to jump next.

On the other hand, the method can converge to the optimal solution much more quickly than without extrapolation, although each step might be more computationally expensive, fewer steps are often needed, which might reduce the total computational cost.

Additionally, extrapolation can help the algorithm to jump out of local minima and explore more of the solution space, which is particularly useful for non-convex problems and for problems where global optimization is needed.[21] The most common extrapolation methods are:

**Linear extrapolation** involves extending a straight line beyond a dataset's limits based on its last known points. This method is most effective when the dataset closely resembles a linear function, or when the extension does not go significantly beyond the known data. Given two closest data points near the point  $x_*$ —namely,  $(x_{k-1}, y_{k-1})$  and  $(x_k, y_k)$ —the function for linear extrapolation is given as:

$$y(x_*) = y_{k-1} + \frac{x_* - x_{k-1}}{x_k - x_{k-1}} \cdot (y_k - y_{k-1}) \quad (4.51)$$

This formula is essentially the same as linear interpolation when  $x_{k-1} < x_* < x_k$ . It's possible to refine this method by using more than two data points and averaging their slopes.

**Polynomial curve** can be accomplished either through the entire dataset or by focusing only on a few end points, two for linear, three for quadratic extrapolation, and so on. This curve can subsequently be extended past the available data. Methods such as Lagrange interpolation or Newton's finite difference technique are commonly used for constructing the polynomial. Once established, the polynomial can be utilized to project future data points. The error margin for extrapolated values tends to increase with the polynomial's degree.

As a first step, two different algorithms have been performed in order to establish which reproduces in a better way the experimental data, and therefore are used two different optimization methods:

- Genetic algorithm
- Patternsearch algorithm with Pearson correlation factor as objective function

Here, The Patternsearch flow chart algorithm with the Pearson correlation factor is shown.

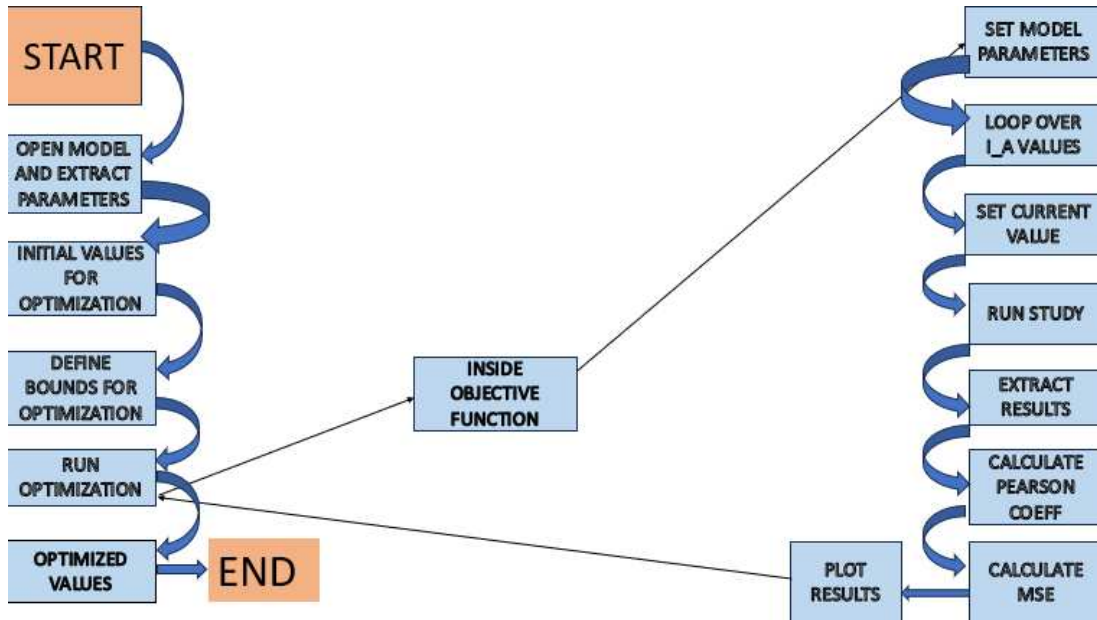


Figure 4.35: Iterative flow chart for the second code

The difference in this code is the objective function which is the Pearson correlation coefficient of the off diagonal square matrix, it is fine which is a square matrix since it means that the number of  $E_{\text{experimental}}$  and  $E_{\text{comsol}}$  is the same as well as the current imposed in the comsol model at each step which correspond exactly with the experimental one.

One of the advantages of using Pearson's correlation coefficient  $r$  is that it is dimensionless and normalized, meaning it accounts for the scale of the data and focuses only on the shape of the relationship.[22]

On the other hand, the correlation matrix only captures linear relationships. It will not detect more complex, non-linear interactions and it is sensitive to outliers, which can significantly impact the coefficient.

Indeed, this seems to be not really accurate, it does not reach the convergence and the best fitting between the two curves is obtained with values of the optimized variables not really precise as it is shown beneath:

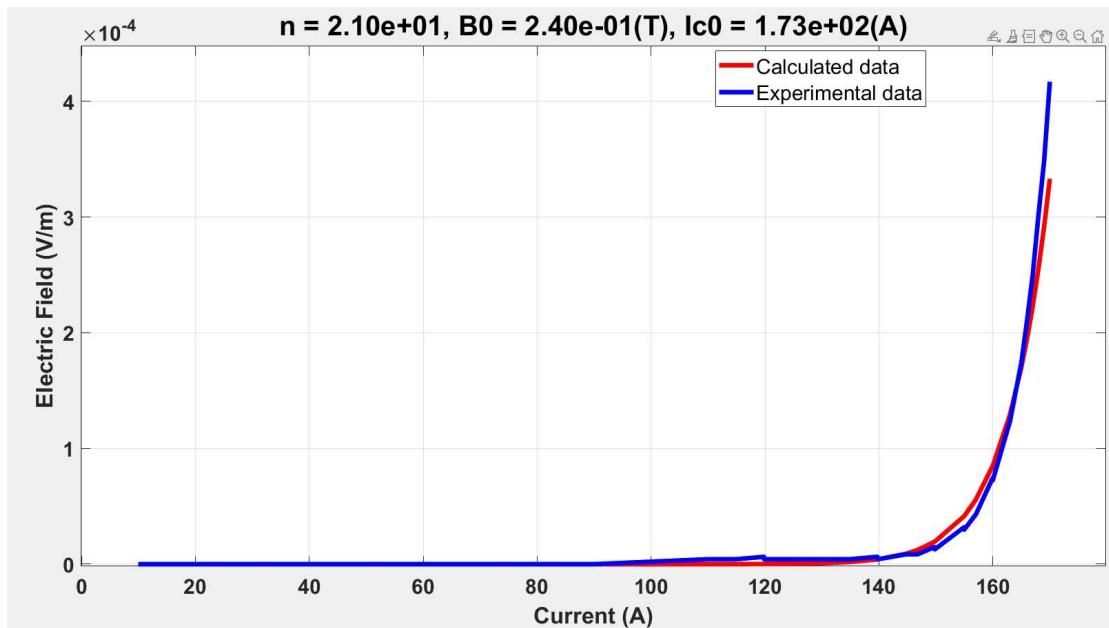


**Figure 4.36:** E-J curve with Pearson correlation coefficient as O.F

Here, the red curve represents the data coming from the software, and the blue one contains the data coming from the experiment in the laboratory.

It is possible to observe from the plot which the curves fit quite well and the optimized variables are:

- $n=21$
- $B_0=240(mT)$
- $I_{c0}=173(A)$

And obviously the value of the critical current is not coherent with the plotted results.

Therefore, the idea has been substituting in the previous code, the optimization algorithm 'patternsearch' with a stochastic one, in particular the 'genetic algorithm' and as a O.F the mean square error to minimize. Underneath, the genetic algorithm is briefly explained.

It is inspired by the process of natural selection. The basic idea is to simulate the process of natural evolution, including mechanisms like selection, crossover (recombination), and mutation, to evolve better and better

solutions to a problem.

The key components of a genetic algorithm include:

- **Population:** A collection of candidate solutions, often termed "chromosomes," each of which represents a potential solution to the problem at hand.
- **Fitness Function:** A function responsible for assessing how close a specific solution is to the ideal solution for the problem.
- **Selection:** The mechanism for choosing specific chromosomes from the population for subsequent reproduction, which involves crossover and mutation processes.
- **Crossover:** The act of combining two parent chromosomes to generate one or more offspring.
- **Mutation:** Introducing random modifications to a chromosome to enhance genetic diversity within the population.

It is important to understand the steps involved in the algorithm and they are listed below:

- **Initialization:** Create an initial set of chromosomes to form the initial population.
- **Evaluation:** Utilize the fitness function to assess the fitness level of each chromosome in the population.
- **Selection:** Choose parent chromosomes based on their fitness scores. Common selection techniques include roulette wheel selection, tournament selection, and elitism.
- **Crossover:** Conduct crossover operations on selected parent pairs to produce offspring. Different crossover types include one-point, multi-point, and uniform crossover.
- **Mutation:** Introduce random alterations to chromosomes. The mutation rate is typically low.
- **New Generation:** Form a new population by choosing individuals from both the current generation and the freshly created offspring.
- **Termination:** Continue to repeat steps 2 through 6 until a specified termination criterion is fulfilled, such as reaching a maximum number of generations or achieving a satisfactory fitness level.

The main advantages of the genetic algorithm are the flexibility, therefore, it can be applied to a wide range of problems, including those where the solution space is discrete, non-linear, and high-dimensional and the ability to find global minima or maxima.

Obviously there are even disadvantages, and the main ones are the possibility to converge at a local optimum instead of a global optimum and the very high computational time.

Here, the flow chart related to the implemented code.

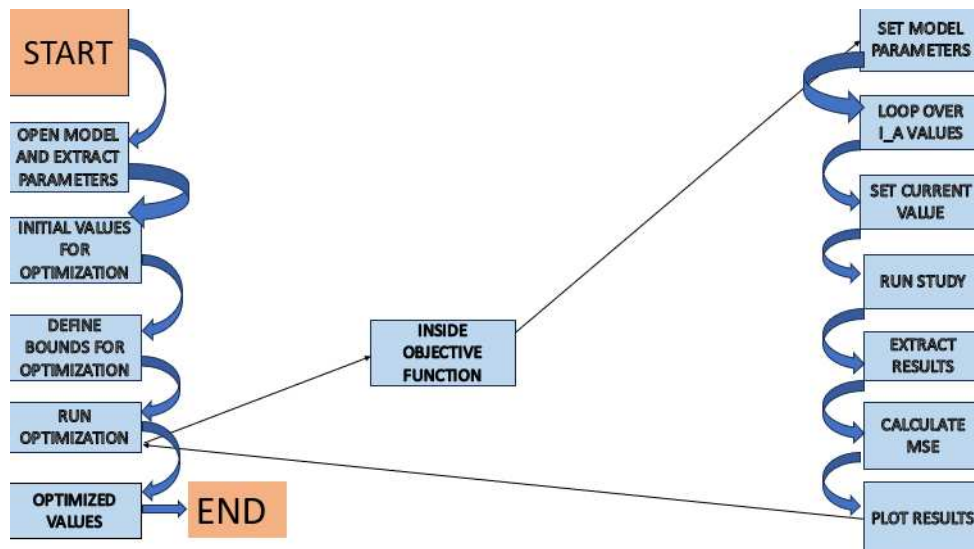
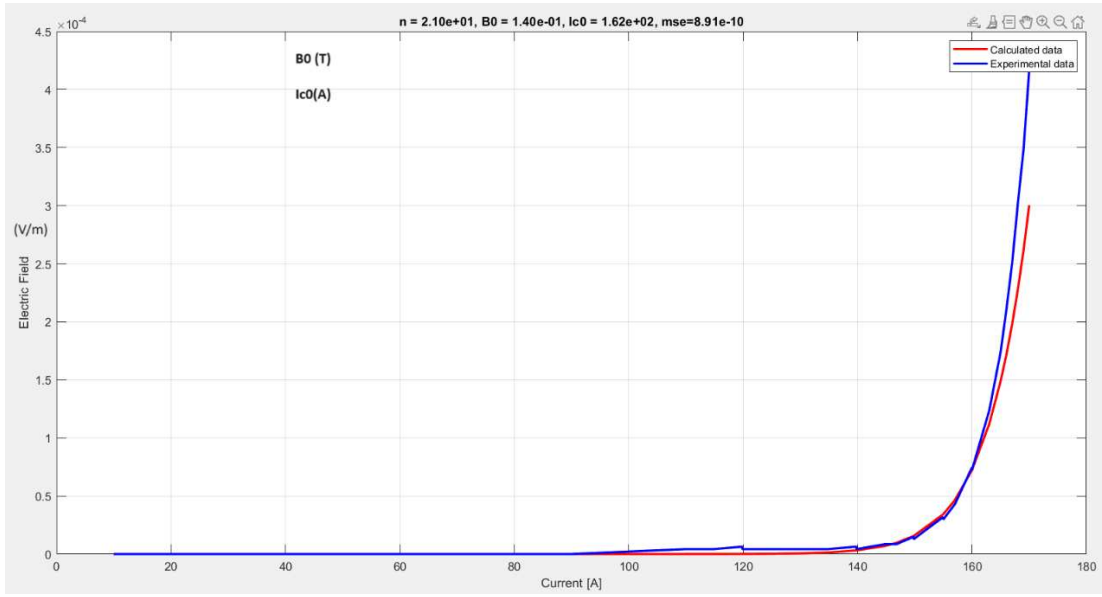


Figure 4.37: Iterative flow chart for the third code

The changes in the code have been explained previously, therefore it is relevant to put in evidence that the code converged to a minimum, getting the values of the optimized variables:

- $n=21$
- $B_0=140(\text{mT})$
- $I_{c0}=162(\text{A})$

and it is shown in the following graph:



**Figure 4.38:** E-J curve with Genetic algorithm

Here, the values of the optimized variables and the minimized O.F.

**Table 4.13:** Optimal values of the variables in order to minimize the MSE

n	B0(T)	Ic0(A)	mse
21	1.4	162	8.91e-10

It is relevant observing that the mse is really small ( $8.91 \times 10^{-10}$ ), the optimized variables values are plausible and the value of the  $\vec{E}$  computed at  $I_{c0}$  is very close to  $1 \times 10^{-4}$  V/m.

The matlab code has been executed measuring the time in order to achieve the convergence, and it is possible to look at very interesting results:

- **Convergence time** is equal to 71140 (s) which are around 20 (hours)
- **The Bottleneck** of the code is the study 2 of the software, which provides the value of the Electric field, it covers almost the total time

This results confirm the expected ones, the genetic algorithm could be very slow to reach the convergence as well as the study on the software with the A-formulation and the reliability of the algorithm to reach a plausible convergence.

**Links are disabled because this is a static copy of a profile report**

geneticalgorit>objective\_function (Calls: 253, Time: 71140.182 s)  
 Generated 12-Aug-2023 12:26:30 using performance time.  
 subfunction in file C:\Users\pecch\Desktop\Master degree Thesis\geneticalgorit.m  
 Copy to new window for comparing multiple runs

**Parents** (calling functions)

Function Name	Function Type	Calls
...(x)objective_function(x,model,E_exp,I_a)	anonymous function	253

**Lines where the most time was spent**

Line Number	Code	Calls	Total Time	% Time	Time Plot
82	model.study('std2').run();	9076	70698.302 s	99.4%	
87	E_comsol(i) = mphtable(model,'...)	9075	118.804 s	0.2%	
84	mphtable(model,'tbl90').data;	9075	113.546 s	0.2%	
79	model.param.set('I_a', I_a(i))...	9076	76.850 s	0.1%	
83	model.result.numerical('av15')...	9075	73.768 s	0.1%	
All other lines			58.912 s	0.1%	
Totals			71140.182 s	100%	

**Figure 4.39:** Measured time of convergence of the algorithm (A-formulation)

## 4.5 T-A formulation

The T-A formulation is a very efficient approach to model the macroscopic behavior of superconductors and is introduced here to also decrease the computational time for the optimization. As seen in the previous section, the bottleneck of the optimization is the study 2 of the comsol model. It is expected that the time for this step will decrease if the T-A formulation is used instead of the A formulation .

It has been proven a great efficiency in therms of computational time of the FEA software and in the evaluation of the AC losses.

The core idea of the numerical model in question hinges on the separate calculation of two vector potentials  $T$  and  $A$  in distinct domains. Specifically,  $T$  is computed exclusively within the superconducting domain, while  $A$  is calculated across the entire domain. These state variables,  $T$  and  $A$ , serve as the basis for determining the current density, represented as  $J$ , and the magnetic flux density, denoted as  $B$ .

The unique feature of this model is its fully integrated methodology. It solves for both  $J$  and  $B$  simultaneously, facilitating a continual interchange of these variables. This synergistic approach ensures a comprehensive and accurate solution[23].

The set of governing equations in their general form can be stated as,

$$J = \nabla \times T \quad (4.52)$$

$$B = \nabla \times A \quad (4.53)$$

For type-II superconductors, the resistivity is described using the  $E$ – $J$  power-law relationship which is limited to the superconducting domain,

$$E = \rho_{\text{HTS}} \cdot J = E_c \left( \frac{J}{J_c(B)} \right)^{n(B)-1} \quad (4.54)$$

where  $\rho_{\text{HTS}}$  symbolizes the resistivity of the high-temperature superconducting (HTS) material,  $J_c$  is the critical electric field threshold at  $10^{-4} \text{ V m}^{-1}$ ,  $n$  is the superconducting  $n$ -value, and both  $J_c$  and  $n$  can be functions of the magnetic field.

Incorporating Maxwell-Faraday's equation into the superconducting domain yields,

$$\nabla \times E = -\frac{\partial B}{\partial t} \quad (4.55)$$

Across the entire domain, the traditional  $A$ -formulation is employed via the Maxwell-Ampere's law,

$$\nabla \times \nabla \times A = \mu_0 \mu_r J \quad (4.56)$$

where  $\mu_0$  and  $\mu_r$  denote the magnetic and relative permeability of free space, respectively.

The current density  $J$  is connected to the  $A$ -formulation through an externally imposed surface current density  $J_e$ ,

$$J_e = J \cdot \delta \quad (4.57)$$

where  $\delta$  represents the thickness of the HTS tape. Here,  $J_e$  is given in  $\text{A m}^{-1}$  to account for the thin-strip approximation which neglects the HTS layer's thickness.

The transport current in the superconductor is applied at the tape's terminals and can be represented as an integral over the cross-sectional area of the conductor,

$$I = \oint_S J dS = \oint_S \nabla \times T dS = \int_{\partial S} T ds \quad (4.58)$$

Here,  $S$  is the conductor's cross-section and  $\partial S$  denotes the boundary edges of that cross-section.[23]

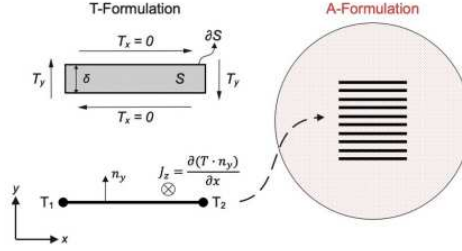


**Figure 4.40:**  $T$  computed on the superconductor layer and  $A$  computed in the whole domain[23]

Owing to the elevated aspect ratio of high-temperature superconducting (HTS) coated conductors, full-surface simulation is computationally expensive. The  $T - A$  formulation offers a novel approach to mitigate this by employing the thin strip approximation. This geometric simplification effectively reduces the HTS tape's surface area to a single thin layer.

As a consequence, the current is constrained to flow solely within this superconducting layer, and the vector potential  $T$  is simplified to its component perpendicular to the tape. In this context, the current vector potential can be expressed as  $T \cdot \mathbf{n}$ , where  $\mathbf{n} = [n_x, n_y, n_z]^T$  and  $\mathbf{n} = [n_r, n_\phi, n_z]^T$  represent the normal vectors to the wide face of the tape in Cartesian and cylindrical coordinates, respectively.

In a 2D approximation, the surface element of the HTS tape simplifies to a 1D line element. Consequently,

$$J_z = \frac{\partial(T \cdot n_y)}{\partial x} - \frac{\partial(T \cdot n_x)}{\partial y} \quad (4.59)$$

in Cartesian coordinates, or for axisymmetric issues in cylindrical coordinates as

$$J_\phi = \frac{\partial(T \cdot n_r)}{\partial z} \quad (4.60)$$

Depending on the tape's orientation, either  $T \cdot n_y$  or  $T \cdot n_x$  may be disregarded. Equation (4.59) serves as a general form for an 'easy bend' tape, where the current flows in the  $\phi$  direction, thus simplifying the current vector potential to  $T \cdot n_r$ .

Upon incorporating Faraday's law, Equation (4.54) condenses to

$$\left[ \frac{\partial E_z}{\partial y} - \frac{\partial E_x}{\partial z} \right] \cdot \mathbf{n} + \left[ \frac{\partial B_x}{\partial t}, \frac{\partial B_y}{\partial t} \right] \cdot \mathbf{n} = 0 \quad (4.61)$$

for Cartesian coordinates, and

$$-\frac{\partial E_\phi}{\partial z} \cdot \mathbf{n} + \frac{\partial B_r}{\partial t} \cdot \mathbf{n} = 0 \quad (4.62)$$

for cylindrical coordinates. Only the  $x$  or  $y$  components of the magnetic flux density need to be considered, contingent on the tape's orientation.

A transport current, defined as in Equation (4.57), can be administered to the tape edges via

$$I = (T_1 - T_2)\delta \quad (4.63)$$

where  $T_1$  and  $T_2$  signify the current vector potentials at the corresponding edge points, and  $\delta$  is the tape thickness.[23]

### 4.5.1 Model implemented on the software

To replicate the behavior of the superconductor and compare the experimental results with the simulated ones, in the software a superconductor submerged by air with properties similar to the the laboratory state, essentially, a tape surrounded by liquid nitrogen.

The model was implemented according with the T-A formulation, therefore, the superconducting layer has been separated in terms of properties with respect to the non-superconducting layer, since the the current vector potential  $T$  should be computed only in the superconducting domain and the magnetic vector potential  $A$  is computed in the entire domain.

Here, the geometry implemented on the software:

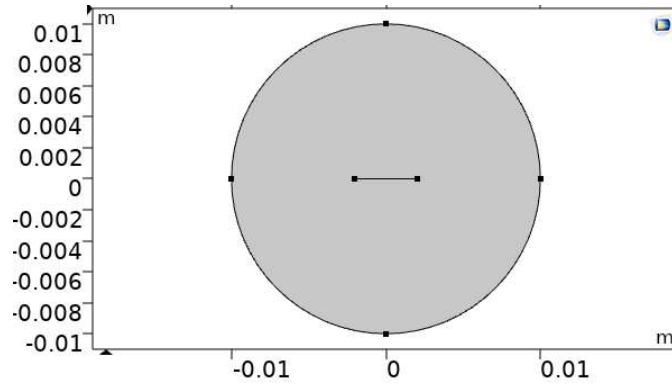


**Figure 4.41:** Geometry implemented according with T-A formulation.

As previously discussed, the model solves for both  $J$  and  $B$  simultaneously. The density current  $J$  is obtained from the potential  $T$  and the magnetic field  $B$  from the vector  $A$  and this approach guarantees high accuracy and speed in terms of obtained results as it may be intuited.

Being analyzed in the laboratory the behavior of (HTS), the resistivity is described by the power law, expressed in the equation (4.52), therefore, different parameters, equations, boundary and initial conditions has been set to solve the numerical simulation.

- Geometrical parameters

**Table 4.14:** Dimensions of the tape and surrounding air

Parameter	Value [SI Units]
Height of the superconducting layer	$1.6 \times 10^{-6}$ m
Height of the tape	$9.56 \times 10^{-5}$ m
Width of the tape	$4 \times 10^{-3}$ m
Length of the tape	0.2 m
Radius of the surrounding air	0.01 m

**Table 4.15:** Physical properties of materials

Parameter	Value
Relative permeability	$1.2566 \times 10^{-6}$ H/m
Resistivity of the air	$2 \times 10^{16}$ $\Omega \cdot m$

•

- Parameters to optimize: As in the A-formulation analysis, the aim of this study is to optimize the fundamental variables, the exponent of the power law, the critical magnetic field and the critical current, in order to minimize the (MSE) between the experimental and simulated data.
- Boundary (PDE) Initial boundary partial differential equations have been imposed on the tape, as discussed in the T-A formulation theory to take in account the vector  $\mathbf{T}$  solving only for the superconducting layer, considering the Current density vector  $\mathbf{T}$  and its first derivative with respect to time equal to zero at  $t=0$  (s).

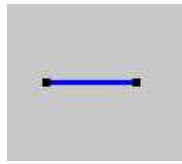


**Figure 4.42:** Initial PDE

On the left side of the tape, the value of the current density vector is imposed equal to zero as prescribed Dirichlet boundary condition, according with the theory discussed.

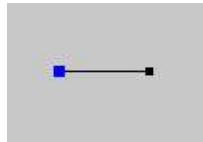


**Figure 4.43:** Dirichlet on the left side

On the other hand, on the right side, the vector  $\mathbf{T}$  is imposed to be variable in time, based on the current waveform description.

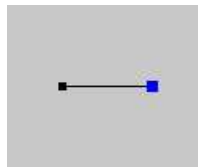


**Figure 4.44:** Dirichlet on the right side

- Physics

The physics 'Magnetic field' is set, taking in account the vector  $A$  which solves for the entire domain, imposing the Ampere Law in the whole domain, magnetic insulation as boundary condition, the value of magnetic vector potential equal to zero as initial condition and, according with the theory, a variable surface current density is imposed perpendicular with respect to the tape.

- Study

A time dependent study has been selected, considering a waveform in case of AC regime, or a step function multiplied by the current amplitude in case of DC regime.

For this study, a matlab code has been implemented, trying to compare the results coming from the two different approaches, the T-A and the A formulation.

Since, the convergence in the previous approach happened for reasonable values of the variables  $n$ ,  $B_0$  and  $I_{c0}$ , the range of variation of the algorithm for these ones has been kept quite close, assuming that the values obtained in the previous simulation is reliable.

The step function used for the DC regime study, saturates at around 0,015(s), therefore, during the transition from 0 to 1, the values of current is simulated until they reach a constant value multiplied by 1.

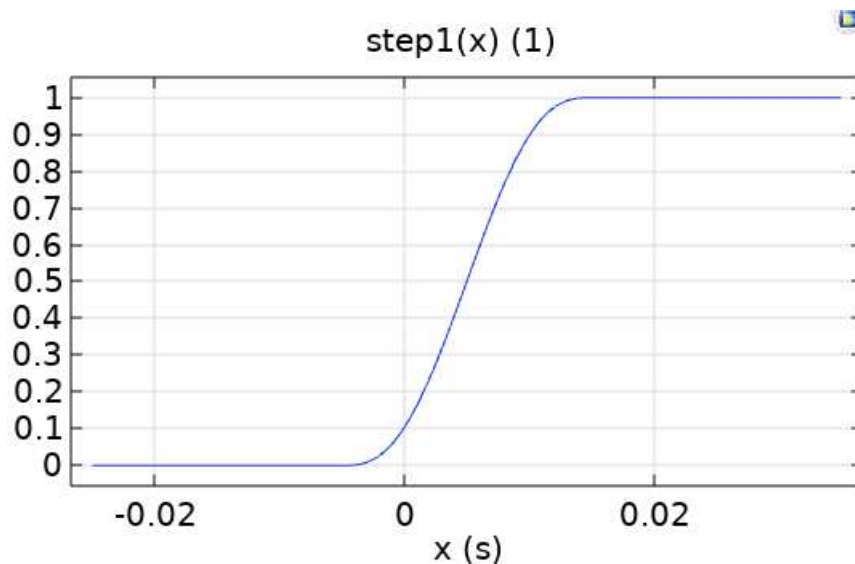
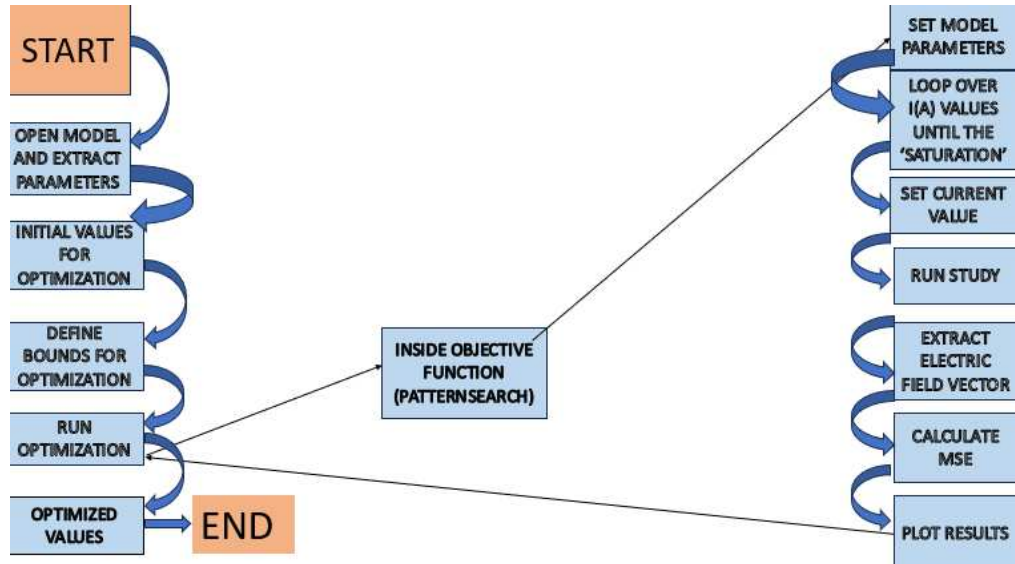


Figure 4.45: Step function

Therefore a for loop until the saturation has been performed to fill the current vectors of I(A) and E(v/m) inside another loop which aims to go ahead until the patternsearch optimization algorithm reaches the convergence, comparing at each loop, the MSE between experimental and simulated power law.

Here, a schematic of the implemented code:



**Figure 4.46:** Schematic matlab code to find best fitting between experimental and simulated power law

It is important to remark that the power law experimental curve and its respective values come from the previous optimization, therefore could not coincide exactly with the measured data since they have been interpolated in order to obtain a smooth curve.

### 4.5.2 Results

Here, the values coming from the numerical analysis are shown, in order to get a first idea of the results obtained.

**Table 4.16:** Relationship between Current  $I_s$  and Electric Field.

Current $I_s$ (A)	Electric Field(V/m)
38.097	$1.2844 \times 10^{-08}$
40.645	$1.5262 \times 10^{-08}$
43.256	$1.8059 \times 10^{-08}$

Current $I_s$ (A)	Electric Field (V/m)
45.925	$2.1557 \times 10^{-08}$
48.65	$2.5602 \times 10^{-08}$
51.425	$3.0261 \times 10^{-08}$
54.247	$3.6086 \times 10^{-08}$
57.112	$4.2864 \times 10^{-08}$
60.014	$5.0709 \times 10^{-08}$
62.949	$6.0488 \times 10^{-08}$
65.913	$7.1801 \times 10^{-08}$
68.902	$8.4850 \times 10^{-08}$
71.909	$1.0110 \times 10^{-07}$
74.931	$1.1997 \times 10^{-07}$
77.963	$1.4185 \times 10^{-07}$
81.0	$1.6908 \times 10^{-07}$
84.037	$2.0060 \times 10^{-07}$
87.069	$2.3791 \times 10^{-07}$
90.091	$2.8206 \times 10^{-07}$
93.098	$3.3347 \times 10^{-07}$
96.087	$3.9593 \times 10^{-07}$
99.051	$4.6671 \times 10^{-07}$
101.99	$5.5139 \times 10^{-07}$
104.89	$6.5179 \times 10^{-07}$
107.75	$7.6708 \times 10^{-07}$
110.57	$8.9962 \times 10^{-07}$
113.35	$1.0574 \times 10^{-06}$
116.07	$1.2357 \times 10^{-06}$
118.74	$1.4351 \times 10^{-06}$
121.35	$1.6626 \times 10^{-06}$
123.9	$1.9109 \times 10^{-06}$
126.38	$2.1789 \times 10^{-06}$
128.8	$2.4697 \times 10^{-06}$
131.13	$2.7767 \times 10^{-06}$
133.4	$3.0988 \times 10^{-06}$
135.58	$3.4717 \times 10^{-06}$
137.68	$3.8319 \times 10^{-06}$
139.7	$4.2235 \times 10^{-06}$
141.63	$4.7547 \times 10^{-06}$
143.48	$5.5886 \times 10^{-06}$
145.23	$7.2283 \times 10^{-06}$
146.89	$9.5591 \times 10^{-06}$
148.46	$1.2206 \times 10^{-05}$

Current $I_s$ (A)	Electric Field (V/m)
149.94	$1.5147 \times 10^{-05}$
151.33	$1.8362 \times 10^{-05}$
152.62	$2.1827 \times 10^{-05}$
153.81	$2.5495 \times 10^{-05}$
154.92	$2.9357 \times 10^{-05}$
155.93	$3.3370 \times 10^{-05}$
156.86	$3.7546 \times 10^{-05}$
157.69	$4.1876 \times 10^{-05}$
158.44	$4.6325 \times 10^{-05}$
159.1	$5.0834 \times 10^{-05}$
159.68	$5.5372 \times 10^{-05}$
160.18	$5.9934 \times 10^{-05}$
160.61	$6.4540 \times 10^{-05}$
160.97	$6.9218 \times 10^{-05}$
161.27	$7.3898 \times 10^{-05}$
161.5	$7.8513 \times 10^{-05}$
161.68	$8.2984 \times 10^{-05}$
161.81	$8.7361 \times 10^{-05}$
161.9	$9.1680 \times 10^{-05}$
161.96	$9.6025 \times 10^{-05}$
161.99	$1.0031 \times 10^{-04}$
162.0	$1.0440 \times 10^{-04}$

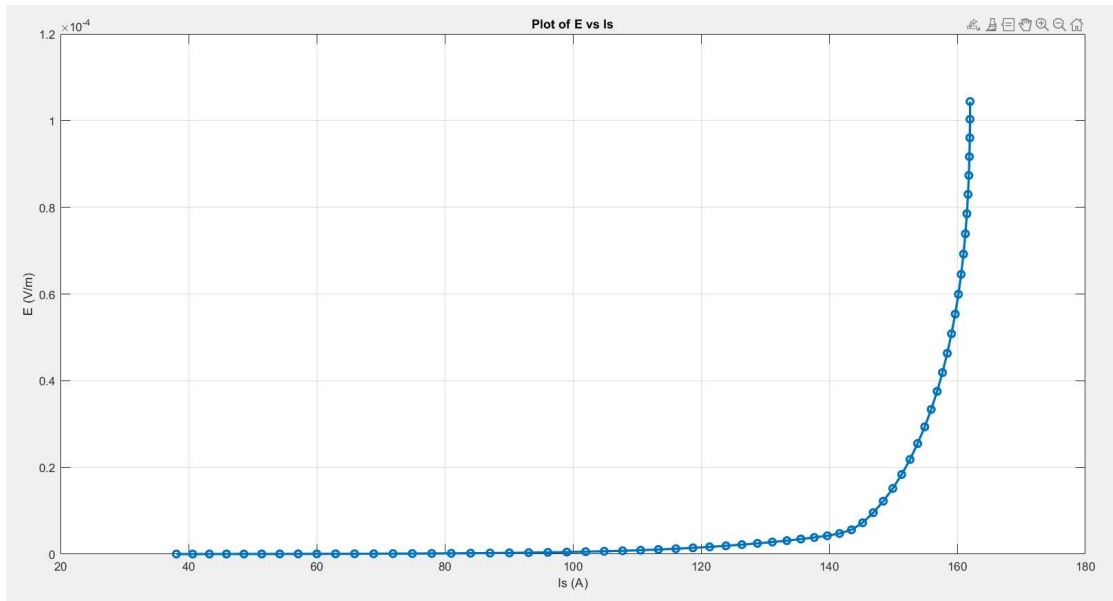


**Figure 4.47:** T-A power Law

It is important to put in evidence even the results of the comparison between the numerical and experimental data coming from the optimization code, to look at the fitting of the two power laws, which due to the optimization techniques, it shows a great matching and therefore a good reliability and accuracy in simulating the experimental data. This could lead in time to a better understanding of the representation of the macroscopic phenomenon and it could be very interesting considering the importance of the superconductivity in possible applications in everyday life.

Here, it is possible to look at the convergence of the algorithm at the best optimization, in particular in the region of transition from superconductive state to a conductive state, which is evident happening around 162(A).

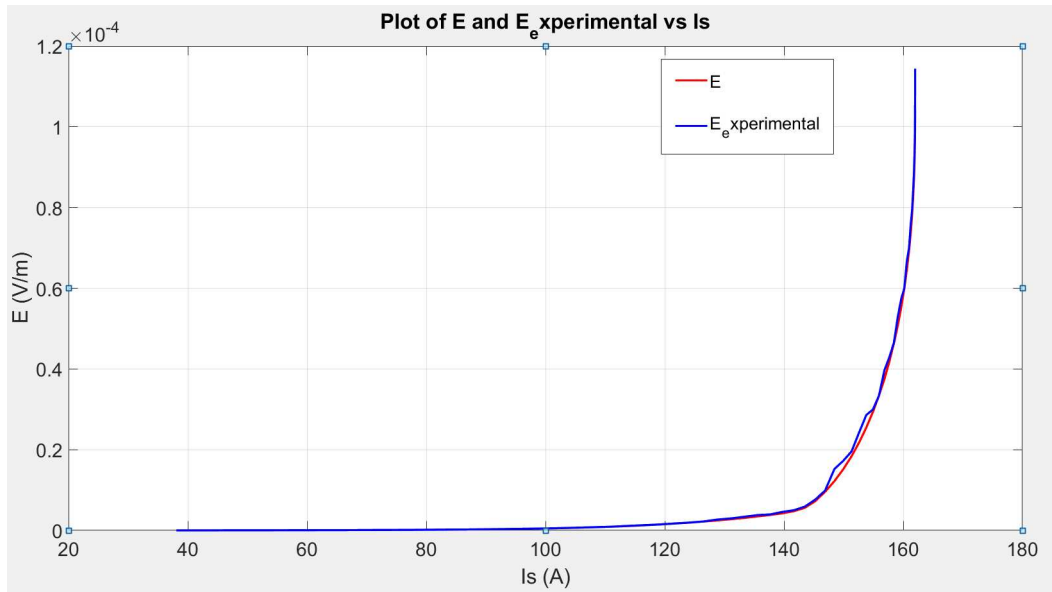


**Figure 4.48:** Fitting between experimental data and numerical optimization

As last observation, even if the code is quite simple due to the restricted range of constraints coming from the previous simulations, the time spent from matlab to converge is really small compared to the A formulation approach, it is only a couple of minutes.

Calls	Total Time (s)	↓	Self Time* (s)	Total Time Plot (dark band = self time)
1	272.319		0.097	
75	258.516		258.516	
77	9.154		9.154	
151	2.208		0.386	
1	0.727		0.022	

**Figure 4.49:** Time to converge T-A formulation

### 4.5.3 Discussion and comparison between the two different approaches

The T-A formulation is particularly preferred in scenarios where the accurate representation of transport current distribution is crucial. This includes the design and analysis of superconducting tapes, wires, and coils where current-carrying capacity (critical current) is a key performance metric. Applications such as fault current limiters, superconducting magnetic energy storage systems, and high-field

magnet design for particle accelerators and MRI machines often rely on the T-A formulation for simulation and optimization.

One of the primary advantages of the T-A formulation is its ability to directly incorporate the transport current as a boundary condition, making it particularly suitable for problems where the current path is not trivial. It provides a more intuitive approach for engineers to specify the current input in simulations. Additionally, the T-A formulation can be more stable numerically when dealing with problems that have high aspect ratios or thin film geometries, which are common in superconducting tapes and coils.

While the T-A formulation is powerful, it comes with its set of challenges. The primary limitation is its computational complexity and the associated costs. The non-linear nature of superconductor behavior, coupled with the complexity of the T-A formulation, requires significant computational resources, especially for three-dimensional models. This can lead to long computation times and may require the use of high-performance computing systems for large-scale problems. Another challenge is the need for detailed material properties and parameters that accurately capture the superconducting state, which can be difficult to obtain experimentally.

In addition, the T-A formulation can become less accurate in scenarios where the assumption of negligible displacement currents (quasi-static approximation) does not hold, such as in very high-frequency applications. Engineers must carefully consider these limitations when choosing to use the T-A formulation for their simulations.

The A formulation is particularly advantageous in situations where the focus is on the magnetic field distribution rather than the currents themselves. This can include cases such as understanding the shielding effect of superconductors, analyzing magnetic levitation phenomena, or calculating the loss distributions within superconducting materials subject to alternating magnetic fields. It is also beneficial when the geometry does not lend itself to easy definition of current paths, such as in complex or multiply-connected superconducting domains.

Using the A formulation simplifies the boundary conditions since it often involves natural magnetic boundary conditions, such as those at infinity or on surfaces where the magnetic field is known. Additionally, the A formulation can be computationally more efficient in problems where the magnetic field varies significantly over the domain but the current distribution is not the primary concern. This efficiency can be quite pronounced when dealing with large-scale simulations or when modeling the interaction of superconductors with external magnetic fields.

One of the limitations of the A formulation is that it does not explicitly include the transport current as a variable, which can make it less intuitive to work with when the current distribution is a primary concern. Moreover, it requires careful treatment of the gauge conditions—additional constraints that must be imposed to ensure a unique solution for A. This can add complexity to the formulation and the numerical implementation.

Another potential complication arises in the presence of moving boundaries or in dynamic simulations where the relationship between the electric field and the vector potential becomes more complex. Furthermore, the A formulation may require finer meshing around the superconducting material to accurately capture the rapid spatial variation of the magnetic fields, leading to higher computational costs.

On balance, it is important to analyze the phenomenon, the performance and results required and then implement the suited macroscopic approach to model the real complex phenomenon.

# Chapter 5

## Conclusions and future work

### 5.0.1 Conclusions

This thesis presented a comprehensive study in the field of superconducting materials, focusing on the integration of thermal aspects in modeling normal conductors and the effective utilization of the A and T-A formulations for optimizing material characterization. The research journey began with the successful modeling of normal conductors, incorporating thermal aspects to enhance the accuracy of simulations. This theoretical model was then substantiated through rigorous experimental verification, serving as a foundational case study.

Advancing further, the thesis delved into the efficient modeling of the A and T-A formulations, which played a crucial role in optimizing material characterization. This optimization was significantly bolstered by the integration of experimental data, ensuring a more realistic and practical approach. The pinnacle of this research was the successful implementation of an optimization strategy in the characterization of superconducting tape. Here, the genetic decision algorithm emerged as the most effective method for material characterization, evidenced by the high degree of correlation observed between the experimental results and the simulations.

A noteworthy achievement of this research was the substantial reduction in optimization time achieved through the adept use of the T-A formulation, cutting down the process from several hours to mere minutes. This leap in efficiency not only signifies a methodological breakthrough but also underscores the practical implications of this research. The methodologies and findings of this study pave the way for future endeavors in accurately characterizing material properties for Finite Element Method (FEM) models, with a particular focus on superconducting tapes.

## **5.0.2 Future work**

The research presented in this thesis, while comprehensive in its current scope, opens several avenues for future investigations, particularly in the realm of applied superconductivity. A significant aspect of this potential research pertains to the study of AC losses in superconductors, a topic that has emerged as a primary focus in contemporary superconductivity research. This thesis has already laid the groundwork by highlighting the criticality of AC loss studies for practical applications of superconductors. Future research could expand upon this foundation, delving deeper into the intricacies of AC loss phenomena and their implications in real-world superconducting applications.

One of the more promising directions for future work involves the application of the calibration methods developed in this thesis to the study of AC losses. The calibration techniques presented here, possess the potential to significantly enhance the accuracy and efficacy of AC loss analysis in superconductors. This advancement could provide critical insights into optimizing superconducting materials for practical applications, thereby bridging the gap between theoretical research and applied technology.

It is also noteworthy to consider the potential integration of temperature dependence into the optimization algorithms used for material characterization.

Since the critical current density ( $J_c$ ) can be defined as a function of temperature, incorporating this variable into the algorithm could substantially refine the calibration process. Such an enhancement would allow for a more nuanced and accurate characterization of superconducting materials, taking into account their temperature-dependent behaviors.

# Appendix A

First Matlab code to evaluate the best values of  $I_{c0,n}$  and  $B_0$  which minimize the O.F (MSE)

```
1 % OPENING THE MODEL AND EXTRACTING BASIC PARAMETERS
2 mphopen superconductor_simulation_correct.mph
3 mphgeom(model)
4 mphmesh(model)
5 mphtable(model, 'tbl90').data
6 mphgetexpressions(model.param)
7 expressions=mphgetexpressions(model.param);
8 mphmeshstats(model).numelem(2)
9 model.mesh('mesh21').feature('size').set('hauto',2)
10 model.mesh('mesh21').run
11 mphgetexpressions(model.variable('var13'))
12 variabili1=mphgetexpressions(model.variable('var13'));
13 mphgetexpressions(model.variable('var2'))
14 variabili2=mphgetexpressions(model.variable('var2'));
15 mphgetexpressions(model.variable('var1'))
16 variabili3=mphgetexpressions(model.variable('var1'));
17 Jc = model.func('an2');
18 rho_sc= model.func('an3');
19 sigma=model.func('an4');
20 n = expressions{19, 4};
21 B0 =expressions{20, 4};
22 Ic0 = expressions{22, 4};
23 %VALUES OF EXPERIMENTAL CURRENT AND ELECTRIC FIELD
```

```

24 I_a = [5; 10; 15; 20; 30; 40; 45; 50; 60; 70; 80; 90;
        100; 110; 120; 125; 125.91; 126.91; 127.91; 128.89;
        129.89; 130.89; 131.885; 132.89; 133.89; 134.878;
        135.86; 136.87; 137.865; 138.865; 139.86; 140.85;
        141.85; 142.85; 143.83; 144.83; 145.84; 146.84;
        147.83; 148.83; 149.83; 150.9; 151.9; 152.98; 153.98;
        154.98; 155.99; 156.98; 157.96; 158.96; 159.96;
        160.96; 161.967; 162.978; 163.985; 164.976; 165.965;
        166.97; 167.98; 168.96; 169.96; 170.94; 171.94;
        172.92; 173.93; 174.94; 175.94; 176.93; 177.94;
        178.95; 179.94];
25
26 E_exp = [0; 0; 0; 0; 0; 0; 0; 0; 0; 0; 4.7619e-06;
          4.7619e-06; 4.7619e-06; 1.42857e-05; 1.90476e-05;
          2.38095e-05; 3.33333e-05; 3.80952e-05; 3.80952e-05;
          4.7619e-05; 6.19048e-05; 7.38095e-05; 8.09524e-05;
          8.80952e-05; 9.7619e-05; 0.000104762; 0.00011619;
          0.000138095; 0.000152381; 0.000171429; 0.000188095;
          0.0002; 0.000219048; 0.000247619; 0.000271429;
          0.000302381; 0.000330952; 0.000354762; 0.000378571;
          0.000414286; 0.000428571; 0.000471429; 0.000504762;
          0.000552381; 0.000604762; 0.000652381; 0.000704762;
          0.000766667; 0.00082381; 0.0009; 0.000966667;
          0.001047619; 0.001138095; 0.00122381; 0.001328571;
          0.001438095; 0.001557143; 0.001690476; 0.001809524;
          0.00197619; 0.002142857; 0.002285714; 0.00252381;
          0.002785714; 0.003095238; 0.003428571; 0.003714286;
          0.004095238; 0.00452381; 0.004904762; 0.005571429];
27
28
29 % Extract initial values for n, B0, and Ic0
30 n_init =n;
31 B0_init =B0;
32 Ic0_init =Ic0;
33
34 % Create the vector of initial values
35 x0 = [n_init, B0_init, Ic0_init];
36
37 % Define the bounds for the parameters
38 lb = [11,0.1,158];
39 ub = [28,0.25,164];

```

```

40
41 % Use MATLAB's patternsearch function to minimize the
    objective function, it is a
42 % direct optimization algorithm and does not require the
    computation of the gradient of the objective or
    constraint functions.
43 % it useful for problems where the objective or
    constraint functions are discontinuous or non-
    differentiable.
44
45 options = optimoptions(@patternsearch,'Display','iter','
    PlotFcn',@psplotbestf);
46 [x_opt, fval] = patternsearch(@(x) objective_function(x,
    model, E_exp, I_a), x0, [], [], [], [], lb, ub, [],
    options);
47
48
49
50 % The optimized values of n, B0, and Ic0 are available
    in x_opt
51 n_opt = x_opt(1);
52 B0_opt = x_opt(2);
53 Ic0_opt = x_opt(3);
54
55 % Objective function that computes the mean square error
56 function mse = objective_function(x, model, E_exp, I_a)
57
58 n = x(1);
59 B0 = x(2);
60 Ic0 = x(3);
61
62 % Set the new parameter values in the model
63 model.param.set('n', n);
64 model.param.set('B0', B0);
65 model.param.set('Ic0', Ic0);
66
67 % Initialize the result vector
68 E_comsol = zeros(size(I_a));
69
70 % Loop over each value in I_a
71 for i = 1:length(I_a)

```

```

72
73     % Set the value of the current
74     model.param.set('I_a', I_a(i));
75
76     % Run the study
77     model.study('std2').run();
78     model.result.numerical('av15').setResult;
79     mphtable(model, 'tbl90').data;
80
81     % Get the result
82     E_comsol(i) = mphtable(model, 'tbl90').data(end);
83
84     % Display the result
85     disp(['I_a = ', num2str(I_a(i)), ', E_comsol = ',
86         num2str(E_comsol(i))]);
86 end
87
88
89
90
91     % Direct exponential interpolation of the calculated
92     and experimental data
92     E_comsol_interp = exp(interp1(I_a, log(E_comsol + eps),
93         I_a, 'spline'));
93     E_exp_interp = exp(interp1(I_a, log(E_exp + eps), I_a,
94         'spline'));
94
95 %Computation of the mean square error
96
97     mse = mean((E_comsol_interp - E_exp_interp).^2);
98
99
100
101     figure;
102     plot(I_a, E_comsol_interp, 'r', 'LineWidth', 2);
103     hold on;
104     plot(I_a, E_exp_interp, 'b', 'LineWidth', 2);
105     legend('Calculated data', 'Experimental data');
106     xlabel('Current [A]');
107     ylabel('Electric Field');

```

```

108     title(sprintf('n = %.2e, B0 = %.2e, Ic0 = %.2e, mse
109     =%.2e', n, B0, Ic0, mse));
110     grid on;
111     hold off;
112
113
114 end

```

Matlab code for the second set of data, here, Pearson correlation coefficient is used as O.F

```

1 % OPENING THE MODEL AND EXTRACTING BASIC PARAMETERS
2 mphopen superconductor_simulation_correct.mph
3 mphgeom(model)
4 mphmesh(model)
5 mphtable(model, 'tbl90').data
6 mphgetexpressions(model.param)
7 expressions=mphgetexpressions(model.param);
8 mphmeshstats(model).numelem(2)
9 model.mesh('mesh21').feature('size').set('hauto',2)
10 model.mesh('mesh21').run
11 mphgetexpressions(model.variable('var13'))
12 variables1=mphgetexpressions(model.variable('var13'));
13 mphgetexpressions(model.variable('var2'))
14 variables2=mphgetexpressions(model.variable('var2'));
15 mphgetexpressions(model.variable('var1'))
16 variables3=mphgetexpressions(model.variable('var1'));
17 Jc = model.func('an2');
18 rho_sc= model.func('an3');
19 sigma=model.func('an4');
20 n = expressions{19, 4};
21 B0 =expressions{20, 4};
22 Ic0 = expressions{22, 4};
23 %VALUES OF EXPERIMENTAL CURRENT AND ELECTRIC FIELD

```

```

24 I_a = [9.9875; 10.0037; 20.0035; 49.9555; 49.9615;
        69.9538; 89.937; 109.876; 109.894; 114.859; 119.838;
        119.84; 124.821; 129.802; 134.806; 139.768; 139.807;
        144.76; 145.804; 146.8; 149.802; 149.807; 154.95;
        154.978; 156.946; 156.984; 159.98; 159.987; 163.005;
        163.012; 165.02; 166.016; 167.03; 168.023; 169.018;
        170.01];
25 E_exp = [0; 0; 0; 0; 0; 0; 0; 0; 4.25532E-06; 4.25532E-06;
          4.25532E-06; 6.38298E-06; 4.25532E-06; 4.25532E-06;
          4.25532E-06; 4.25532E-06; 6.38298E-06; 4.25532E-06;
          8.51064E-06; 8.51064E-06; 8.51064E-06; 1.48936E-05;
          1.2766E-05; 3.19149E-05; 2.97872E-05; 4.25532E-05;
          4.25532E-05; 7.44681E-05; 7.23404E-05; 0.000123404;
          0.000123404; 0.000174468; 0.000210638; 0.000251064;
          0.000302128; 0.000348936; 0.000417021];
26
27
28
29 % Extract initial values for n, B0, and Ic0
30 n_init =n;
31 B0_init =B0;
32 Ic0_init =Ic0;
33
34 % Create the vector of initial values
35 x0 = [n_init, B0_init, Ic0_init];
36
37 % Define the bounds for the parameters
38 lb = [19,0.1,160];
39 ub = [21,0.2,174];
40
41 % Use MATLAB's patternsearch to minimize the objective
    function
42 options = optimoptions(@patternsearch,'Display','iter','
    PlotFcn',@psplotbestf);
43 [x_opt, fval] = patternsearch(@(x) objective_function(x,
    model, E_exp, I_a), x0, [], [], [], [], lb, ub, [],
    options);
44
45
46 % The optimized values of n, B0, and Ic0 are available
    in x_opt

```

```

47 n_opt = x_opt(1);
48 B0_opt = x_opt(2);
49 Ic0_opt = x_opt(3);
50
51 % Objective function that computes the Pearson
    correlation coefficient
52 function r = objective_function(x, model, E_exp, I_a)
53
54
55     n = x(1);
56     B0 = x(2);
57     Ic0=x(3);
58
59 % Set the new parameter values in the model
60 model.param.set('n', n);
61 model.param.set('B0', B0);
62 model.param.set('Ic0', Ic0);
63
64 % Initialize the result vector
65 E_comsol = zeros(size(I_a));
66 % Loop over each value in I_a
67     for i = 1:length(I_a)
68
69         % Set the value of the current
70
71         model.param.set('I_a', I_a(i));
72
73         % Run the study
74         model.study('std2').run();
75         model.result.numerical('av15').setResult;
76         mphtable(model, 'tbl90').data;
77
78         % Get the result
79         E_comsol(i) = mphtable(model, 'tbl90').data(end);
80
81
82
83         % Display the result
84         disp(['I_a = ', num2str(I_a(i)), ', E_comsol = ',
    , num2str(E_comsol(i))]);
85     end

```

```

86
87     % Calculate the Pearson correlation coefficient
88 R = corrcoef(E_comsol, E_exp);
89 r = -R(1,2); % Extract the correlation coefficient
      from the matrix with minus therefore the algorithm
      tends to minimize, otherwise, it go away from the
      best result
90
91
92 % Direct exponential interpolation of the calculated
      and experimental data
93 E_comsol_interp = exp(interp1(I_a, log(E_comsol + eps
      ), I_a, 'spline'));
94 E_exp_interp = exp(interp1(I_a, log(E_exp + eps), I_a
      , 'spline'));
95 %calculate mse
96 mse = mean((E_comsol_interp - E_exp_interp).^2);
97
98
99
100 figure;
101 plot(I_a,E_comsol_interp, 'r', 'LineWidth', 2);
102 hold on;
103 plot(I_a, E_exp_interp, 'b', 'LineWidth', 2);
104 legend('Calculated data', 'Experimental data');
105 xlabel('Current [A]');
106 ylabel('Electric Field');
107 title(sprintf('n = %.2e, B0 = %.2e, Ic0 = %.2e', n,
      B0, Ic0));
108
109 grid on;
110 hold off;
111
112 end

```

Matlab code for the second set of data, here, MSE is used as O.F and the optimization algorithm is the Genetic algorithm.

```

1 % OPENING THE MODEL AND EXTRACTING BASIC PARAMETERS
2 mphopen superconductor_simulation_correct.mph
3 mphgeom(model)

```

```

4 mphmesh(model)
5 mphtable(model, 'tbl90').data
6 mphgetexpressions(model.param)
7 expressions=mphgetexpressions(model.param);
8 mphmeshstats(model).numelem(2)
9 model.mesh('mesh21').feature('size').set('hauto',2)
10 model.mesh('mesh21').run
11 mphgetexpressions(model.variable('var13'))
12 variables1=mphgetexpressions(model.variable('var13'));
13 mphgetexpressions(model.variable('var2'))
14 variables2=mphgetexpressions(model.variable('var2'));
15 mphgetexpressions(model.variable('var1'))
16 variables3=mphgetexpressions(model.variable('var1'));
17 Jc = model.func('an2');
18 rho_sc= model.func('an3');
19 sigma=model.func('an4');
20 n = expressions{19, 4};
21 B0 =expressions{20, 4};
22 Ic0 = expressions{22, 4};
23
24 %VALUES OF EXPERIMENTAL CURRENT AND ELECTRIC FIELD
25 %I_exp= [9.9875; 10.0037; 20.0035; 49.9555; 49.9615;
        69.9538; 89.937; 109.876; 109.894; 114.859; 119.838;
        119.84; 124.821; 129.802; 134.806; 139.768; 139.807;
        144.76; 145.804; 146.8; 149.802; 149.807; 154.95;
        154.978; 156.946; 156.984; 159.98; 159.987; 163.005;
        163.012; 165.02; 166.016; 167.03; 168.023; 169.018;
        170.01];
26
27 % Original values up to 170.01
28 I_a_original = [9.9875; 10.0037; 20.0035; 49.9555;
        49.9615; 69.9538; 89.937; 109.876; 109.894; 114.859;
        119.838; 119.84; 124.821; 129.802; 134.806; 139.768;
        139.807; 144.76; 145.804; 146.8; 149.802; 149.807;
        154.95; 154.978; 156.946; 156.984; 159.98; 159.987;
        163.005; 163.012; 165.02; 166.016; 167.03; 168.023;
        169.018; 170.01];
29
30 % New values from 171 to 210 with a step of 1
31 I_a_new = (171:1:210)';
32

```

```

33 % Combine original and new values
34 I_a = [I_a_original; I_a_new];
35
36 E_exp = [0+eps; 0+eps; 0+eps; 0+eps; 0+eps; 0+eps; 0+eps
; 4.25532E-06; 4.25532E-06; 4.25532E-06; 6.38298E-06;
4.25532E-06; 4.25532E-06; 4.25532E-06; 4.25532E-06;
6.38298E-06; 4.25532E-06; 8.51064E-06; 8.51064E-06;
8.51064E-06; 1.48936E-05; 1.2766E-05; 3.19149E-05;
2.97872E-05; 4.25532E-05; 4.25532E-05; 7.44681E-05;
7.23404E-05; 0.000123404; 0.000123404; 0.000174468;
0.000210638; 0.000251064; 0.000302128; 0.000348936;
0.000417021];
37 E_comsol = zeros(length(I_a), 1);
38
39
40 % Step 2: Simulation Loop
41 for i = 1:length(I_a)
42     % Set the value of the current
43     model.param.set('I_a', I_a(i));
44     % Run the study
45     model.study('std2').run();
46     model.result.numerical('av15').setResult;
47     % Get the result
48     E_comsol(i) = mphtable(model, 'tb190').data(end);
49     % Display the result
50     disp(['I_a = ', num2str(I_a(i)), ', E_comsol = ',
num2str(E_comsol(i))]);
51 end
52
53 % Fit an exponential model to the data up to 170 A
54 fittype_exp = fittype('a*(x/b).^21+c', 'independent', 'x
', 'dependent', 'y');
55 opts = fitoptions(fittype_exp);
56 opts.StartPoint = [0.0001 162 0];
57 exp_fit = fit(I_a_original, E_exp, fittype_exp, opts);
58
59 % Predict E_exp values for the entire I_a range
60 E_exp_combined = feval(exp_fit, I_a);
61
62
63

```

```

64
65 % Step 3: Interpolation in order to obtain continuous
    curves
66 I_fine = linspace(min(I_a), max(I_a), 1000); % Fine mesh
    for interpolation using cubic Hermite interpolation(
    pchip)
67 E_comsol_fine = interp1(I_a, E_comsol, I_fine, 'pchip');
68 E_exp_combined_fine = interp1(I_a, E_exp_combined,
    I_fine, 'pchip');
69
70 % Step 4: Plot the Results
71 figure;
72 plot(I_fine, E_comsol_fine, 'r-', I_fine,
    E_exp_combined_fine, 'b-');
73 xlabel('Current [A]');
74 ylabel('Electric Field');
75 legend('E_comsol', 'E_exp_combined');
76 title('Comparison of E_comsol and E_exp_combined');
77 grid on;

```

# Bibliography

- [1] K.T. Chau Calvin C.T. Chow a Mark D. Ainslie b. «High temperature superconducting rotating electrical machines: An overview». In: 9 (2023), pp. 1125–1126 (cit. on pp. 1, 5, 19–27).
- [2] Steven M. Anlage. «Microwave Superconductivity». In: 1 (2021), p. 390 (cit. on p. 2).
- [3] Martin N. Wilson. *Superconducting magnets*. 1983, pp. 1–2 (cit. on p. 2).
- [4] CC BY-SA 4.0 By PJRay - Own work. *Online kalman filter tutorial*. URL: <https://commons.wikimedia.org/w/index.php?curid=46193149> (cit. on p. 4).
- [5] *Evolution of superconductors*. URL: <https://commons.wikimedia.org/w/index.php?curid=46193149> (cit. on p. 4).
- [6] Martin N. Wilson. *Superconducting magnets*. 1983, pp. 7–18 (cit. on pp. 6–10).
- [7] Hongye Zhang - Zezhao Wen - Francesco Grilli - Konstantinos Gyftakis - Markus Mueller. *Alternating Current Loss of Superconductors Applied to Superconducting Electrical Machines*. URL: <https://www.mdpi.com/1996-1073/14/8/2234#> (cit. on pp. 14, 19).
- [8] Zach Stone P.E. *How to Solve Transformer Flux, Reluctance, MMF, and Magnetic Circuits*. URL: <https://www.electricalpereview.com/how-to-solve-transformer-flux-reluctance-mmf-and-magnetic-circuits/> (cit. on p. 29).
- [9] Stack Exchange-physichs. *Is torque in an electric motor generated from repelling magnetic dipoles and the Lorentz force on a solenoid?* URL: <https://physics.stackexchange.com/questions/366255/is-torque-in-an-electric-motor-generated-from-repelling-magnetic-dipoles-and-the> (cit. on p. 31).
- [10] Matlab| Mellor P.H.- R. Wrobel and D. Holliday. *FEM-Parameterized PMSM*. URL: <https://ww2.mathworks.cn/help/sps/ref/femparameterizedpmsm.html> (cit. on p. 32).

- [11] K R Siddhapura | D B Raval. *A Textbook of Electrical Machines*, pp. 10–304 (cit. on pp. 32, 36).
- [12] J. D. Jackson. *Classical electrodynamics*, pp. 150–350 (cit. on pp. 34, 44).
- [13] <https://engineeringlearn.com/operation-of-induction-motor/>. *Operation of Induction Motor*. URL: <https://engineeringlearn.com/operation-of-induction-motor/> (cit. on p. 34).
- [14] A.Hughes B.Drury. *Electric Motors and drives Fundamentals*, pp. 230–380 (cit. on pp. 36, 38, 39).
- [15] David Griffiths. *Introduction to Electrodynamics*. 2012 (cit. on pp. 41, 42).
- [16] P.M.Gerhart-A.L.Gerhart-J.I.Hochstein. *Fundamentals of fluid mechanics*. 2016, pp. 85–435 (cit. on p. 45).
- [17] Mark Ainslie. *Power law*. URL: [https://en.m.wikipedia.org/wiki/File:E\\_J\\_Power\\_Law.JPG](https://en.m.wikipedia.org/wiki/File:E_J_Power_Law.JPG) (cit. on p. 67).
- [18] I. S. P. Peixoto S. Vaschetto J. F. P. Fernandes P. J. C. Branco A. Tenconi and A. Cavagnino. «Modelling Approach for Superconducting ac Windings: Case Study on Axial Flux PM Machines». In: (2023), pp. 1–3 (cit. on p. 75).
- [19] R. | Jeeves Hooke. *Direct search solution of numerical and statistical problems*. 1961, pp. 180–238 (cit. on p. 78).
- [20] Ahlberg Nielson Walsh. *The Theory of Splines and Their Applications*. 1967 (cit. on p. 79).
- [21] C. Brezinski | M. Redivo Zaglia. *Extrapolation Methods.Theory and Practice*. 1991 (cit. on p. 85).
- [22] Sheldon M. Ross. *Probabilità e statistica per l'ingegneria e le scienze*. 1991 (cit. on p. 86).
- [23] Felix Huber Wenjuan Song Min Zhang Francesco Grilli. «The T-A formulation: an efficient approach to model the macroscopic electromagnetic behaviour of HTS coated conductor applications». In: (2022), pp. 1–3 (cit. on pp. 92–94).